

# POLITECNICO DI TORINO

Collegio di Ingegneria Biomedica

## Master of Science in Biomedical Engineering

Master of Science Thesis

### Structural Analysis of Low-Density Lipoprotein Interactions with Proteins and Corona Formation



**Politecnico  
di Torino**



#### Supervisors:

Prof.ssa Laura Fabris - Politecnico di Torino

Prof. Francesco Stellacci - École Polytechnique Fédérale de Lausanne

Dr. Quy Ong Khac - École Polytechnique Fédérale de Lausanne

Ph.D. Ding Ren - École Polytechnique Fédérale de Lausanne

#### Candidate:

Martina Campagna

Academic Year 2024-2025



*Alla mia famiglia,  
e a chi mi guarda da lassù*



## Abstract

Lipoproteins are naturally occurring biological nanoparticles circulating in our bloodstream. Researchers have paid great attention to their function in cholesterol transport and to their relationship with various diseases like cardiovascular disease and metabolic disorder. Their characteristics as nanoparticles have long been ignored. In a biological environment, lipoproteins may also bind with various proteins, and form hard and/or a soft corona on their surface, similar to other nanoparticles.

In this thesis, low-density lipoproteins (LDL) are isolated using density gradient ultracentrifugation (DGUC), followed by fast protein liquid chromatography (FPLC) purification to minimize the presence of pre-existing protein corona. The purified LDL are characterized through dynamic light scattering (DLS) and transmission electron microscopy (TEM) before being incubated with human serum albumin (HSA), immunoglobulin G (IgG), and apo-transferrin to form a protein corona. These proteins were selected based on their varying abundance in plasma and their differing affinities for nanoparticle surfaces. HSA, the most abundant plasma protein, is primarily involved in molecular transport but interacts weakly with nanoparticles, a behaviour also observed for apo-transferrin. In contrast, IgG, the dominant immunoglobulin in blood, exhibits stronger binding to LDL.

Sedimentation velocity analytical ultracentrifugation (SV-AUC) is employed to assess the size and interaction dynamics of LDL after corona formation. It is observed that the purity of the LDL samples significantly influences the interaction between LDL and proteins, indicating the existence of both a hard corona and a soft corona.

Additionally, it was found that the binding of LDL to plasma proteins is highly protein-specific, with IgG forming stronger associations, leading to larger LDL-protein complexes. To further explore the function of protein corona on lipoproteins, isolated LDL is precipitated using a high concentration PEG solution. However, the results show no significant difference compared to LDL isolated through DGUC followed by FPLC, indicating that PEG precipitation does not alter LDL behaviour under these conditions.

This thesis provides valuable insights into the interactions between lipoproteins and plasma proteins, contributing to a deeper understanding of protein corona formation on LDL. Furthermore, the findings highlight the potential to modulate protein corona composition, paving the way for advancements in lipoprotein-based therapeutics for precision medicine.



# Table of Contents

<b>Abstract</b> .....	<b>i</b>
<b>1. Introduction and Objectives</b> .....	<b>1</b>
1.1 Protein Corona Formation .....	3
1.2 Introduction to Lipids and Lipoproteins.....	4
1.3 Key Proteins in Human Serum .....	7
1.5 Challenges of AUC Theory in Describing Protein-Nanoparticle Interactions .....	10
1.6 Thesis Objectives.....	10
<b>2. Materials</b> .....	<b>13</b>
<b>3. Methods</b> .....	<b>15</b>
3.1 Low-Density Lipoproteins (LDL) Extraction Protocols .....	15
3.1.1 1 <sup>st</sup> Protocol.....	15
3.1.2 2 <sup>nd</sup> Protocol without Staining .....	17
3.1.3 2 <sup>nd</sup> Protocol with Staining .....	19
3.1.4 2 <sup>nd</sup> Protocol with PEG Precipitation.....	20
3.1.5 2 <sup>nd</sup> Protocol with Filtering Several Times .....	21
3.1.6 SEC-based purification of commercial LDL.....	22
3.2 LDL and Protein Incubation Procedure.....	22
3.2.1 Interactions between LDL particles and Human Serum Albumin (HSA).....	22
3.2.2 Interactions between stained LDL particles and HSA .....	23
3.2.3 Interactions between LDL particles and Immunoglobulin G (IgG) .....	24
3.2.4 Interactions between stained LDL particles and IgG .....	27
3.2.5 Interactions between LDL particles with HSA and IgG .....	28
3.3 Characterization Techniques for Isolated LDL .....	32
3.3.1 FPLC .....	32
3.3.2 Sodium Dodecyl Sulphate-PolyAcrylamide Gel Electrophoresis (SDS-PAGE)...	33
3.3.3 Dynamic Light Scattering (DLS) .....	33
3.3.4 Transmission Electron Microscopy (TEM).....	34
3.3.5 Sedimentation Velocity Analytical Ultracentrifugation (SV-AUC) .....	35
<b>4. Results and Discussion</b> .....	<b>39</b>
4.1 Evaluation of Low-Density Lipoprotein (LDL) Extraction Methods .....	39
4.1.1 Analysis of Fast Protein Liquid Chromatography (FPLC) .....	39
4.1.2 Dynamic Light Scattering (DLS) Characterization .....	41

4.1.3 Transmission Electron Microscopy (TEM) Characterization .....	42
4.1.4 Sodium Dodecyl Sulphate- PolyAcrylamide Gel Electrophoresis (SDS-PAGE) characterization .....	43
4.1.5 Sedimentation Velocity Analytical Ultracentrifugation (SV-AUC) Characterization.....	45
4.2 Interactions between LDL and Human Serum Albumin (HSA) .....	47
4.2.1 Interactions between unstained LDL particles and HSA .....	47
4.2.2 Interactions between stained LDL particles and HSA .....	48
4.3 Interactions between LDL and Human Immunoglobulin G (IgG).....	49
4.3.1 Analysis of LDL-IgG Interaction – 1 <sup>st</sup> Experiment.....	49
4.3.2 Analysis of LDL-IgG Interaction – 2 <sup>nd</sup> Experiment.....	50
4.3.3 Analysis of the Interaction of LDL Filtered Several Times with IgG.....	54
4.3.4 Analysis of the Interaction of Stained LDL with IgG .....	54
4.4 Interactions between LDL, HSA and IgG .....	55
4.5 Interactions between LDL and Human Apo-Transferrin Protein.....	61
4.5.1 Analysis of the Interaction of LDL and Apo-Transferrin Protein.....	61
4.5.2 Analysis of the Interaction of LDL Filtered Several Times and Apo-Transferrin Protein .....	61
<b>5. Conclusions and Future Work.....</b>	<b>63</b>
<b>6. List of Figures .....</b>	<b>65</b>
<b>7. List of Tables .....</b>	<b>69</b>
<b>References.....</b>	<b>71</b>
<b>Acknowledgements.....</b>	<b>77</b>

# 1. Introduction and Objectives

Lipoproteins, natural nanoparticles present in our body, are efficient carriers of lipids and cholesterol [1]. They can be grouped into different categories based on their size, density, the type of internal cholesterol, and the presence of specific apolipoproteins [2]. These categories include chylomicrons (CM), very low-density lipoproteins (VLDL), low-density lipoproteins (LDL), intermediate-density lipoproteins (IDL), and high-density lipoproteins (HDL) [2].

Among them, LDL are particularly significant due to their involvement in cholesterol delivery from the liver to peripheral tissues [3]. Indeed, LDL is often referred to as “bad” cholesterol, as it can build up in the walls of arteries, leading to blockages and increasing the risk of heart disease[4], where HDL is known as “good” cholesterol because it helps remove excess cholesterol from the bloodstream, promoting cardiovascular health [4].

LDL have a diameter ranging from 17 to 28 nm and consist of a lipid core rich in cholesterol esters, encased in a phospholipid monolayer embedded with apolipoproteins, mainly Apolipoprotein B-100 (ApoB-100), a ~550 kDa protein essential for structural stability and receptor-mediated interactions [3].

When LDL, and in general nanoparticles (particles with at least one dimension smaller than 500 nm), interact with biological fluids, proteins and biomolecules present in the surrounding environment rapidly adsorb onto their surface, forming a protein corona [5]. This protein layer not only stabilizes the nanoparticle by reducing its surface energy [5], but also modifies its physicochemical properties, influencing biological recognition, receptor interactions, and cellular uptake [6]. Moreover, the structure of the protein corona can be divided into hard and soft coronas, based on the strength of the interaction between the proteins and the nanoparticle surface [7].

A two-step process is applied to isolate LDL from serum. The process includes a density gradient ultracentrifugation (DGUC) step to remove triglyceride-rich particles and serum proteins by density, followed by fast protein liquid chromatography (FPLC) system with a size-exclusion column (SEC) to separate lipoproteins by size [8]. This approach effectively removes contaminating serum proteins, thereby significantly reducing the presence of any pre-existing protein corona. This is achieved due to the strong stripping force applied during the process, as well as the notable density difference between proteins and lipoproteins, which facilitates their efficient separation [8]. As a result, the nanoparticles or lipoproteins can be analyzed or utilized with minimal interference from unwanted protein adsorption, ensuring more accurate and reproducible experimental outcomes [8].

Despite the extensive research on lipoproteins in relation to cholesterol metabolism and cardiovascular disease, their behaviour as nanoparticles and their interactions with serum proteins remain less explored [9]. Understanding how LDL interacts with serum proteins and the factors influencing protein corona formation is essential for a more comprehensive view of LDL biology, particularly in physiological and pathological contexts.

Currently there is not a one-method-for-all approach but multiple techniques are utilized in combination to thoroughly characterize the size, density, shape, ligand shell of nanoparticles [10].

Analytical ultracentrifugation (AUC), particularly sedimentation velocity (SV) experiments, is employed to assess the size distribution, sedimentation behaviour, and interaction dynamics

of LDL-protein complexes. This high-resolution approach provides insights into molecular weight and hydrodynamic properties, allowing for the identification of protein-specific binding patterns and distinguishing between hard and soft corona components [11].

## 1.1 Protein Corona Formation

Due to their unique surface activity, in a solution, nanoparticles rapidly adsorb various biomolecules, particularly proteins, onto their surface, forming a protein layer that stabilizes them in a low-energy state [1]. This layer, termed “Protein Corona”, was first introduced by Kenneth A. Dawson and co-workers [12] in 2007. Different dynamic interaction strength between biomolecules and nanoparticles leads to the classification of protein corona into two main categories: the hard corona and the soft corona [5].

The hard corona consists of proteins that exhibit a strong affinity for the nanoparticle surface, forming a tightly bound inner layer that is often regarded as stable and difficult to remove [7]. In contrast, the soft corona is composed of proteins that interact more loosely with the outer layer, associating through reversible interactions and weaker protein-nanoparticle binding [7]. Due to their strong interactions, hard corona proteins tend to remain attached to the nanoparticle surface for extended periods, whereas soft corona proteins are more dynamic and can easily detach under physiological conditions [13]. A common hypothesis suggests that hard corona proteins directly adhere to the nanoparticle surface, while soft corona proteins associate indirectly by interacting with the hard corona layer [14], whereas Pareek et al. [6] propose that both types of proteins may bind directly to the nanoparticle surface, differing in their binding strengths and interaction dynamics.

When nanoparticles enter a physiological environment, the initial adsorption is dominated by highly abundant and rapidly diffusing proteins like serum albumin, which attach to the particle surface due to their high concentration [5]. However, as time progresses, these loosely bound proteins are gradually displaced by proteins that possess stronger affinities for the nanoparticle, such as immunoglobulins and complement factors [15], as shown in Figure 1. This competitive exchange, known as the Vroman effect, is influenced by both protein concentration and binding kinetics [5]. The process involves continuous competitive interactions, where numerous biomolecules compete for available binding sites on the nanoparticle surface [16]. This dynamic competition is a key factor in shaping the final composition of the protein corona, as proteins with higher affinities gradually replace those initially adsorbed.

This effect is understood to be one of the key mechanisms underlying the differences between the protein profiles in the corona and those in the surrounding biological fluid. Furthermore, a dynamic equilibrium is established through rapid adsorption and dissociation between bound corona proteins and free proteins in the biological fluid [17]. This exchange can occur within minutes or take hours to days to stabilize, depending on nanoparticle properties and environmental conditions [18]. Additionally, adsorbed proteins may undergo structural modifications due to hydrophobic and electrostatic interactions, ultimately stabilizing the corona in a thermodynamically favorable state [6].

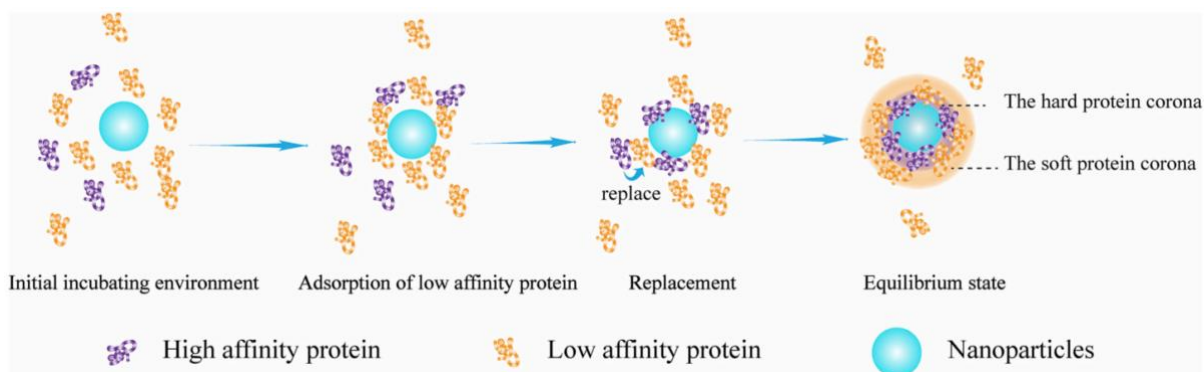


**Figure 1** – Schematic representation of protein corona formation [5].

From a kinetic standpoint, nanoparticle-protein interactions in biological fluids are primarily governed by non-covalent forces, including electrostatic attractions, hydrophobic interactions, and hydrogen bonding [19] [20]. While electrostatic forces are often a key factor, they act alongside other molecular interactions in determining the stability and composition of the protein corona [6].

## 1.2 Introduction to Lipids and Lipoproteins

Lipoproteins play a crucial role in lipid transport, as cholesterol and triglycerides are insoluble in water and need to associate with proteins to circulate effectively [21]. These macromolecular complexes not only facilitate the absorption and distribution of dietary lipids from the intestine but also ensure the transport of lipids from the liver to peripheral tissues and the reverse cholesterol transport to the liver [22]. In addition to their primary role in lipid metabolism, lipoproteins contribute to the removal of hydrophobic and amphipathic toxic compounds, such as bacterial toxins, preventing their accumulation in sites of infection and inflammation [22].

Their structural organization enables them to perform these functions effectively. Lipoproteins consist of a hydrophobic central core containing cholesterol esters and triglycerides, surrounded by an outer hydrophilic layer made up of phospholipids, free cholesterol, and apolipoproteins [23] (**Figure 2**).

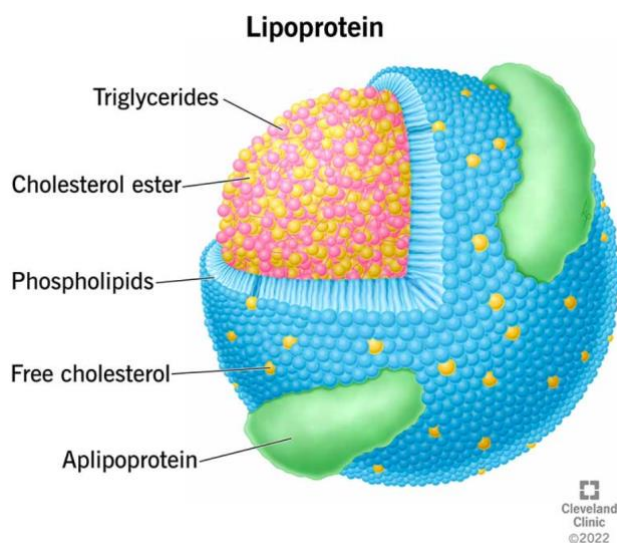


**Figure 2** – Lipoprotein structural composition [23].

The specific composition of this outer layer determines the interactions of lipoproteins with cells and receptors, influencing metabolic pathways [24]. Based on their size, lipid composition, and apolipoprotein content, plasma lipoproteins are classified into seven categories: chylomicrons, chylomicron remnants, VLDL, VLDL remnants (IDL), LDL, HDL, and Lp(a), each with distinct metabolic functions and destinies in circulation [21] (Table 1).

<b>Lipoprotein</b>	<b>Density (g/mL)</b>	<b>Size (nm)</b>	<b>Major Lipids</b>	<b>Major Apoproteins</b>
<b>Chylomicrons</b>	<0.930	75-1200	Triglycerides	Apo B-48, Apo C, Apo E, Apo A-I, A-II, A-IV
<b>Chylomicron Remnants</b>	0.930 - 1.006	30-80	Triglycerides Cholesterol	Apo B-48, Apo E
<b>VLDL</b>	0.930 - 1.006	30-80	Triglycerides	Apo B-100, Apo E, Apo C
<b>IDL</b>	1.006 - 1.019	25-35	Triglycerides Cholesterol	Apo B-100, Apo E, Apo C
<b>LDL</b>	1.019 - 1.063	18- 25	Cholesterol	Apo B-100
<b>HDL</b>	1.063 - 1.210	5- 12	Cholesterol Phospholipids	Apo A-I, Apo A-II, Apo C, Apo E
<b>Lp (a)</b>	1.055 - 1.085	~30	Cholesterol	Apo B-100, Apo (a)

**Table 1** – overview of all the lipoprotein classes [21].

Among these, LDL particles, also known as “bad cholesterol”, primarily derived from VLDL and IDL, are the main cholesterol carriers in the bloodstream. Each LDL particle contains a single Apo B-100 molecule, but variations in the size and density of LDL significantly affect their atherogenic potential [25]. In contrast, HDL particles, often referred to as “good cholesterol”, play a protective role by mediating reverse cholesterol transport [25]. HDL facilitates the removal of excess cholesterol from peripheral tissues, including arterial walls, and transports it back to the liver for excretion or recycling, thereby reducing the risk of atherosclerosis [4]. The balance between LDL and HDL cholesterol is a crucial determinant of cardiovascular health, as excessive LDL accumulation leads to plaque formation in the arteries, while sufficient HDL levels help counteract this process [26].

At the molecular level, apolipoproteins are central to lipoprotein metabolism, acting as structural components, ligands for receptors, and enzyme regulators [27]. Apo B-100, synthesized in the liver, is a key structural element of VLDL, IDL, and LDL and plays a crucial role in LDL clearance by binding to LDL receptors [28].

LDL receptors, primarily expressed in the liver, are responsible for recognizing Apo B-100 and Apo E, thus mediating the endocytosis of LDL, chylomicron remnants, and IDL [21]. Once internalized, these lipoproteins are degraded in lysosomes, releasing cholesterol into the cell [21]. This available cholesterol exerts a feedback mechanism that regulates intracellular cholesterol homeostasis by inhibiting the activity of HMG-CoA reductase (a key enzyme in cholesterol synthesis), suppressing the expression of the LDL receptor, and thus modulating further cholesterol uptake [26]. The number of LDL receptors in hepatic cells is a crucial

determinant of plasma LDL levels [26]. When receptor expression is reduced, LDL clearance slows, leading to elevated plasma LDL concentrations, whereas an increase in receptor expression improves LDL uptake and reduces circulating LDL levels [26].

Due to their significant role in lipid metabolism and their implication in pathological conditions, extensive efforts have been made to establish reliable protocols for their isolation and purification [21][8]. Over the years, various techniques have been developed, each offering distinct advantages and limitations depending on the application, sample type, and desired purity level.

Typical protocols for LDL extraction have primarily relied on density-based methods, such as ultracentrifugation (UC), which separates lipoproteins based on their buoyant density [28]. This approach, often combined with salt gradients, remains one of the most widely used methods due to its high efficiency and reproducibility[28]. However, UC can be time-consuming and may alter the native structure of LDL particles. Furthermore, combining density gradient ultracentrifugation (DGUC) with SEC has been employed to isolate LDL, based not only on their density, but also on their size (Figure 3) [8].

Alternative approaches are also explored to optimize the isolation strategy and evaluate how different techniques may influence the characterization of the protein corona. Among these, polyethylene glycol (PEG) precipitation offers a simple and effective method to selectively aggregate and precipitate LDL while excluding smaller plasma proteins [29]. Another strategy is centrifugal filtration, which employs ultrafiltration membranes with a 100 kDa molecular weight cutoff (MWCO) to remove the protein corona. This process selectively retains LDL while washing away loosely bound proteins and plasma contaminants [30]. Each protocol presents unique challenges, including sample volume requirements, potential contamination by other lipoproteins, and variations in yield or purity.

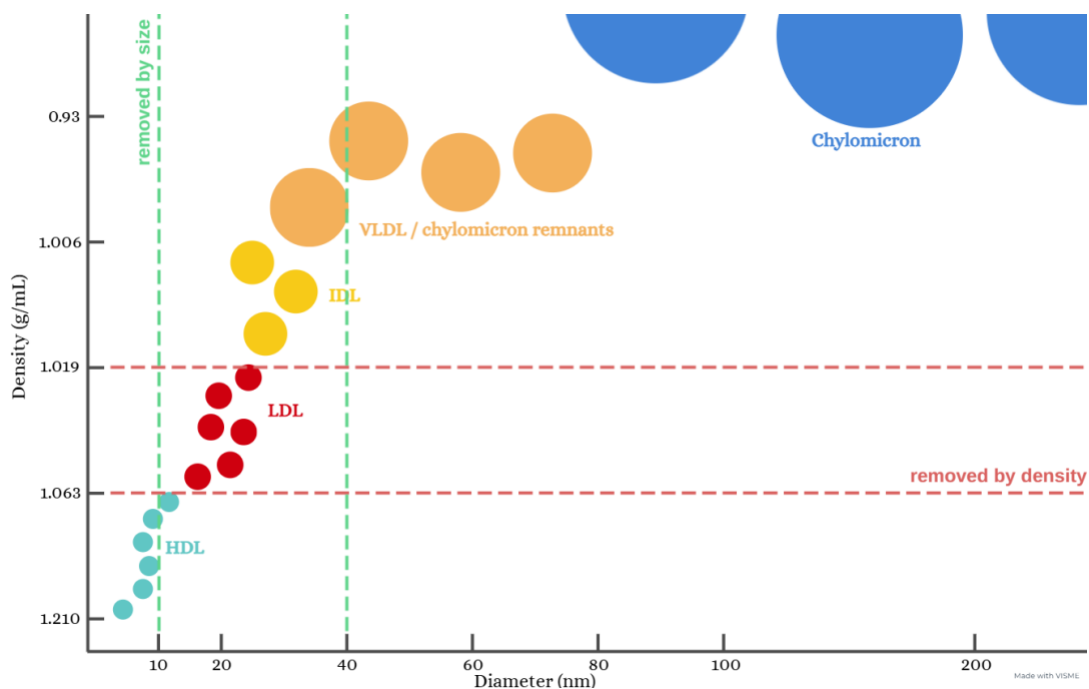


**Figure 3** – Schematic overview of the size and density of various lipoproteins, including high-density lipoproteins (HDL), low-density lipoproteins (LDL), intermediate-density lipoproteins (IDL), very low-density lipoproteins (VLDL), and chylomicrons [made with VISME].

### 1.3 Key Proteins in Human Serum

Human serum is a complex and dynamic fluid containing hundreds of proteins that serve essential physiological functions. The measurement of serum proteins is particularly relevant, as serum represents the fluid that remains after plasma has clotted, effectively removing fibrinogen and most clotting factors. The total serum protein concentration typically ranges between 6 and 8 g/dL, with albumin accounting for approximately 3.5 to 5.0 g/dL, while the remaining portion consists of globulins [31].

As depicted in Figure 4, the six most abundant proteins constitute approximately 85% of the total protein mass in human serum, whereas the 13 most abundant proteins account for about 94% of the total protein mass [31].

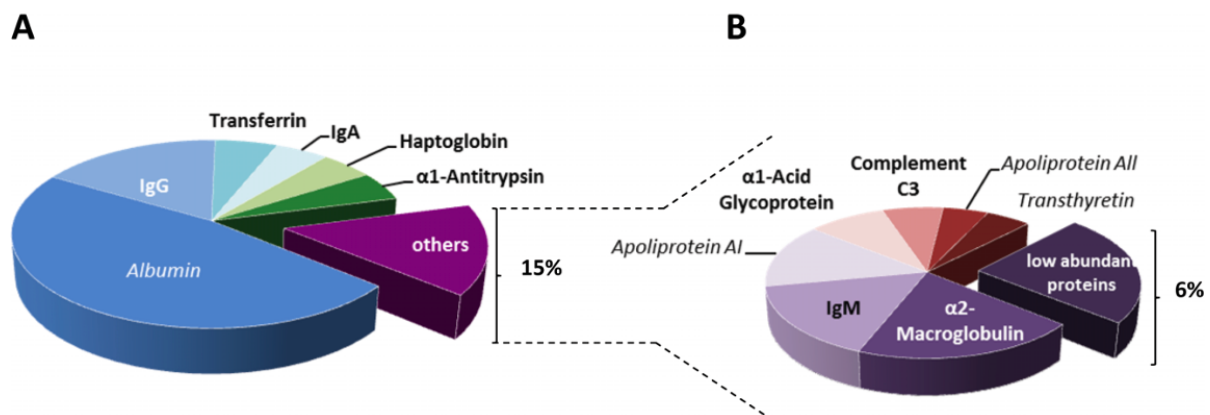


**Figure 4** – Charts representing human serum composition. (A) The 6 most abundant proteins represent approximately 85% of the total protein mass in human serum. (B) The 13 most abundant proteins are said to represent approximately 94% of the total protein mass in human serum. Apolipoprotein AI, AII and transthyretin are non-glycosylated proteins [31].

Albumin is the most abundant protein in human serum. Synthesized in the liver, it has a MW of approximately 66 kDa and represents nearly 45-50% of total serum protein and has multiple physiological functions, including maintaining colloid osmotic pressure, acting as a transporter for various molecules, and regulating fluid distribution across capillaries [33]. Due to its negative charge at physiological pH, albumin interacts with cations, particularly sodium ion, a phenomenon known as the Gibbs-Donnan effect [31]. Furthermore, it plays an essential role in binding and transporting bilirubin, hormones, metals, vitamins, and drugs, while also aiding in fat metabolism by solubilizing fatty acids in plasma [31].

The globulin fraction, which accounts for the remaining serum protein content, comprises a diverse group of proteins, including carrier proteins, enzymes, components of the complement system, and immunoglobulins. Globulins are classified into four primary groups ( $\alpha 1$ ,  $\alpha 2$ ,  $\beta$ , and  $\gamma$ ) based on their electrophoretic migration pattern. The immunoglobulin family consists of five major classes, IgG, IgA, IgM, IgE, and IgD, each with distinct functions and structural features [34].

IgG is the most abundant immunoglobulin in serum, with concentrations ranging between 600 and 1500 mg/dL [35]. It accounts for approximately 75% of total serum immunoglobulins and plays a crucial role in immune defence against bacterial and viral infections. It is a large 150 kDa molecule composed of two heavy and two light chains, with attached oligosaccharides that contribute to its stability and effector functions [36].

Apart from albumin and immunoglobulins, numerous other high-abundance serum proteins, primarily glycoproteins such as transferrin, play crucial roles in physiological processes [37]. Transferrin, with a normal serum concentration of approximately 200-360 mg/dL and a MW of 79 kDa, is responsible for iron transport and homeostasis. This liver-synthesized glycoprotein binds ferric iron derived from haemoglobin degradation and delivers it to cells [38].

## 1.4 The Analytical Ultracentrifugation (AUC) Theory

Analytical Ultracentrifugation (AUC) was introduced in the 1920s by Theodor Svedberg as a method for studying gold particle size distributions. His innovative work on dispersed systems, including the development of AUC, earned him the Nobel Prize in Chemistry in 1926. This technique remains a highly effective approach for characterizing nanoparticles, providing precise measurements of sedimentation coefficients, particle size and shape, molar mass, and density across the colloidal scale. AUC offers exceptional resolution at the Angstrom level, combined with robust statistical analysis, making it a valuable tool for studying nanoparticles in both solution and suspension [39]. Its ability to separate particles based on density and molecular weight enables the analysis of nanoparticles ranging from 1 nm up to 5000 nm in size. Additionally, its adaptability to various solvents, including both organic and aqueous solutions, has expanded its applications in nanoparticle research.

As illustrated in Figure 5, when a solute particle is suspended in a solvent and subjected to a gravitational field, three distinct forces influence its movement.

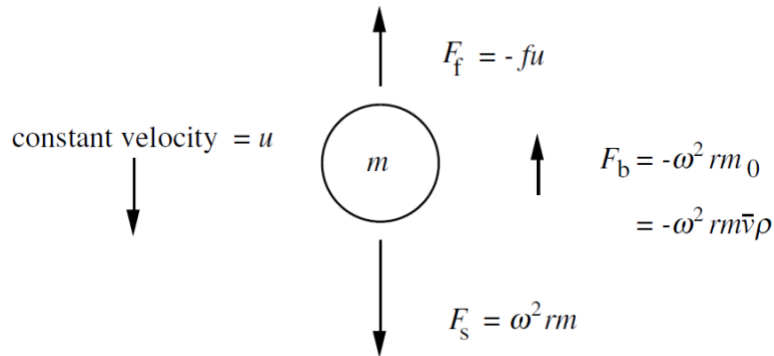


**Figure 5** – Forces acting on a solute particle in a gravitational field [11].

First, there is a sedimenting (or gravitational) force,  $F_s$ , which is expressed as

$$F_s = m\omega^2 r = \frac{M}{N}\omega^2 r \quad (1)$$

where  $m$  represents the mass of an individual particle in grams, and  $\omega^2 r$  corresponds to the acceleration. In a spinning rotor, the acceleration of a particle is determined by its distance from the axis of rotation, denoted as  $r$ , and the square of the angular velocity,  $\omega$ , which is measured in radians per second. The parameter  $M$  represents the molar mass of the solute in g/mol and  $N$  refers to Avogadro's number.

Second, a buoyant force,  $F_b$ , acts on the particle, which can be described as

$$F_b = -m_0\omega^2 r \quad (2)$$

where  $m_0$  is the mass of fluid displaced by the particle, as determined by Archimedes' principle, and is calculated as

$$m_0 = m\bar{v}\rho = \frac{M}{N}\bar{v}\rho \quad (3)$$

$\bar{v}$  represents the partial specific volume, which is the reciprocal of the solute's density per gram, while  $\rho$  represents the solvent's density, measured in g/mL.

As the particle moves radially toward the bottom of the sample compartment, known as the cell, its velocity,  $u$ , increases as the radial distance grows. When moving through a viscous fluid, the particle experiences a frictional resistance that is directly proportional to its velocity, generating a frictional force that can be described as

$$F_f = -fu \quad (4)$$

In this context,  $f$  represents the frictional coefficient, which is influenced by the particle's shape and size. The negative signs in equations (2) and (4) indicate that these forces act in opposition to the direction of sedimentation.

The balance between centrifugal force, buoyancy, and viscous drag is established in less than  $10^{-6}$  s. Following this equilibrium, solute particles start to sediment toward the bottom of the cell at a rate defined as

$$\frac{M(1-\bar{v}\rho)}{Nf} = \frac{u}{\omega^2 r} \equiv s \quad (5)$$

The sedimentation coefficient, denoted as  $s$ , is defined as the velocity of the particle per unit of gravitational acceleration, represented by  $\frac{u}{\omega^2 r}$ . According to equation (5),  $s$  is directly proportional to the molar mass of the particle, adjusted for buoyancy effects, and inversely proportional to the frictional coefficient. The sedimentation coefficient is expressed in seconds, with typical values ranging from 1 and  $100 \times 10^{-13}$  s. In honor of Svedberg, the Svedberg unit (symbolized as S), defined as  $10^{-13}$  s, is used to quantify the sedimentation rate of particles [11].

The concentration distributions of the analyte,  $c(r, t)$ , depend on both time  $t$  and distance from rotor center  $r$ , and these distributions can be superimposed. The shape and changes over time can be described using the Lamm equation (6), which allows for the separation of the sedimentation  $s$  and diffusion  $D$  coefficients [40].

$$\frac{\partial c}{\partial t} = D \left( \frac{\partial^2 c}{\partial r^2} + \frac{1}{r} \frac{\partial c}{\partial r} \right) - \omega^2 s \left( r \frac{\partial c}{\partial r} + 2c \right) \quad (6)$$

Given the challenge of solving the Lamm equation analytically, researchers often resort to approximate numerical solutions to interpret experimental AUC data [39].

Schuck et al. [41] were pioneers in creating software tools like SEDFIT and SEDPHAT, which calculate the sedimentation coefficient distribution function by fitting it to experimental observations. These tools provide user-friendly platforms for assessing predefined models of

both homogeneous and heterogeneous protein-protein interactions, accommodating different stoichiometries [40].

Assuming a constant shape factor, meaning a frictional ratio  $\left(\frac{f}{f_0}\right)$  that remains consistent across all species, the software calculates the Gaussian distribution corresponding to the  $s$ -values for each species, resulting in a " $c(s)$  distribution". This distribution effectively accounts for diffusional broadening associated with high diffusion coefficients through an empirical scaling relationship between  $s$  and  $D$  [41]. Individual species are depicted as peaks within the distribution. The  $c(s)$  method provides high resolution and sensitivity, making it a reliable tool for quantitatively assessing sample heterogeneity and contaminants. However, caution is needed when analyzing systems that undergo rapid self- or hetero-association/dissociation, as such dynamics can lead to misinterpretation of the data.

## **1.5 Challenges of AUC Theory in Describing Protein-Nanoparticle Interactions**

The formation of a protein corona around nanoparticles is a dynamic and competitive process that significantly affects their biological identity and behavior. This corona is subjected to rapid changes, as initially bound proteins, which are often abundant but low affinity, are gradually replaced by less abundant proteins with a higher affinity for the nanoparticle surface. Additionally, there is a continuous exchange between the proteins on the nanoparticles and those free in the surrounding medium [42].

AUC has long been regarded as a robust method for characterizing macromolecular and colloidal systems, providing insights into particle size distribution, density, and interaction dynamics. However, applying SV-AUC to study the protein corona presents challenges, both theoretical and experimental. The heterogeneity and dynamic evolution of the protein corona under physiological condition complicate AUC data interpretation. Moreover, the density and size differences between nanoparticles and bound proteins can hinder the resolution of individual components during sedimentation analysis. Classical AUC methods struggle to fully capture the weak and transient interactions between proteins and nanoparticles, which are influenced by factors like protein concentration, fluid viscosity, and the dynamic nature of protein exchange. Additionally, obtaining a narrow distribution of LDL is essential for differentiating specific interactions at the nanoparticle surface from general protein adsorption effects, enhancing the resolution and accuracy of protein corona characterization.

To accurately characterize the protein corona, it is essential to integrate AUC data with complementary techniques, such as Dynamic Light Scattering (DLS), Fast Protein Liquid Chromatography (FPLC), Sodium Dodecyl Sulphate-PolyAcrylamide Gel Electrophoresis (SDS-PAGE), to achieve a comprehensive understanding.

## **1.6 Thesis Objectives**

The primary objective of this thesis is to explore and elucidate the influence of the protein corona on the interactions between key proteins present in human plasma and LDL particles. To achieve this, SV-AUC has been employed as the central analytical technique, allowing for a detailed assessment of the binding dynamics and structural modifications induced by the

formation of the protein corona.

To obtain a comprehensive understanding, various LDL extraction protocols are developed and evaluated for their efficiency and integrity through DLS, Transmission Electron Microscopy (TEM) and SDS-PAGE.

DLS is employed to measure the size distribution of LDL particles, TEM provided high-resolution imaging to assess morphological features and confirm particle integrity at the nanoscale while, SDS-PAGE allows the identification and analysis of proteins that constitute LDL by separating them based on size. By integrating sedimentation velocity analysis with these characterization techniques, this project aims to provide a thorough analysis of how the protein corona affects the physicochemical properties and biological interactions of LDL particles.

Moreover, the findings highlight the potential to actively modulate the protein corona through targeted isolation and analytical strategies, paving the way for improved lipoprotein-based therapeutic approaches. Such advancements could significantly contribute to precision medicine, where the fine-tuning of protein-nanoparticle interactions enables more targeted and effective disease detection and treatment.



## 2. Materials

1X phosphate buffer saline (pH = 7.4, without calcium, magnesium), sodium chloride (NaCl), ethylenediaminetetraacetic acid disodium (EDTA), sodium bromide (NaBr), sudan red 7B, polyethylene glycol (PEG) 10000, albumin from human serum, IgG from human serum, healthy human serum H5667 were purchased from Sigma-Aldrich. This serum was from USA males with AB type blood and was heat-inactivated serum extracted from clotted whole blood.

Sodium hydroxide (NaOH), acetone, qubit Protein Assay Kit (100 assays), NuPAGE™ 4 to 12% Bis-Tris Gel, NuPAGE™ LDS Sample Buffer (4×), Invitrogen™ NuPAGE™ Sample Reducing Agent (10×), NuPAGE™ MES SDS Running Buffer (20×), Invitrogen™ NuPAGE™ Tricine SDS Sample Buffer (2×), PageRuler Unstained Broad Range Protein Ladder, uranyl acetate, low-density lipoprotein from human plasma (LDL) were purchased from ThermoFisher Scientific.

Potassium bromide (KBr), Transferrin, Apo- were purchased from Millipore.

Ultra-Clear centrifuge tubes were purchased from Beckman Coulter.

Chromafil Xtra PES-45/25 syringe filters were purchased from Macherey-Nagel GmbH & Co.

InstantBlue® Coomassie Protein Stain was purchased from Abcam.

Carbon Film 400 Mesh Copper Grid was purchased from Electron Microscopy Sciences.

Polystyrene (PS) cuvettes were purchased from Sarstedt.



### 3. Methods

#### 3.1 Low-Density Lipoproteins (LDL) Extraction Protocols

##### 3.1.1 1<sup>st</sup> Protocol

The protocol established by Seneshaw et al.[43] [43] is employed with modifications. Specifically, 11.4 g sodium chloride (NaCl), 0.1 g Ethylenediaminetetraacetic Acid Disodium (EDTA) and 1 mL 1M sodium hydroxide (NaOH) are dissolved in 1000 mL Milli-Q water to achieve a density of 1.006 g/mL. The solution is marked as A. 2.52 g sodium bromide (NaBr) is dissolved in 10 mL of solution A to achieve a solution with density at 1.182 g/mL, marked as B. The densities of both solutions A and B are calibrated with a digital precision density meter (DMA 4500 M, Anton Paar).

30 mL of solution A are then added into a 38.5 mL ultra-clear centrifuge tube (25 × 89 mm). Next, 5 mL of Human Serum H5667 are carefully layered beneath solution A using a syringe to create a clear interphase, with serum at the bottom and solution A on top. The prepared tube is centrifugated with the Optima XPN-80 Ultracentrifuge (Beckman Coulter) overnight at 31500 rpm and 8 °C using a swinging-bucket rotor SW32 (Beckman Coulter). After centrifugation, the top 9 mL of the solution are carefully removed using a pipette with a cut tip without disturbing the interphase.

20 mL of the bottom fraction are then mixed to form homogeneous mixture with 10 mL of solution B, maintaining a volume ratio of 2:1, while the remaining 6 mL are discarded. This mixture is then centrifugated for 8 hours at 31500 rpm and 8 °C. Subsequently, 7.5 mL are extracted from the top of the gradient and collected in a separate tube (Figure 6), marked as C.

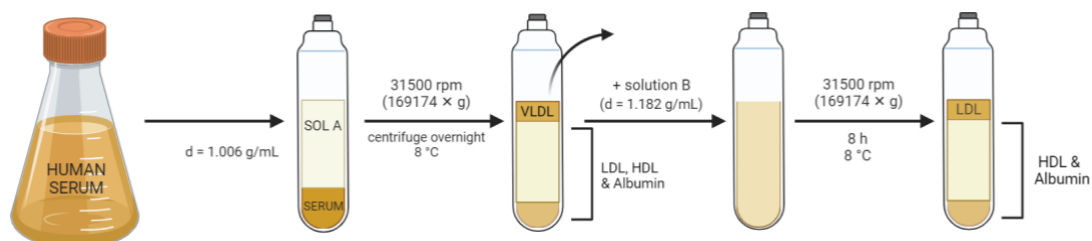


**Figure 6** – Schematic representation of the 1<sup>st</sup> protocol for LDL extraction.

Low-density lipoproteins (LDL) are purified from C using size-exclusion chromatography (SEC). The fast-protein liquid chromatography (FPLC) workstation consists of an automatic ÄKTA go<sup>TM</sup> system Cytiva, and a Superdex 200 Increase 10/300 GL agarose-crosslinked column (Cytiva, Sweden AB). 1X phosphate-buffered saline (PBS, pH 7.4, without  $Mg^{2+}$  and  $Ca^{2+}$ ) is used as the elution and equilibration buffer.

Two injections are performed into the column using a 500  $\mu$ L capillary loop, and a flow rate of 0.75 mL/min: one with 500  $\mu$ L of diluted C and another with 500  $\mu$ L of C concentrated using an Amicon Ultra-15 Centrifugal Filters Ultracel-10K (20 min, 5000 rpm, 10 °C) before injection into the FPLC system (Figure 7).

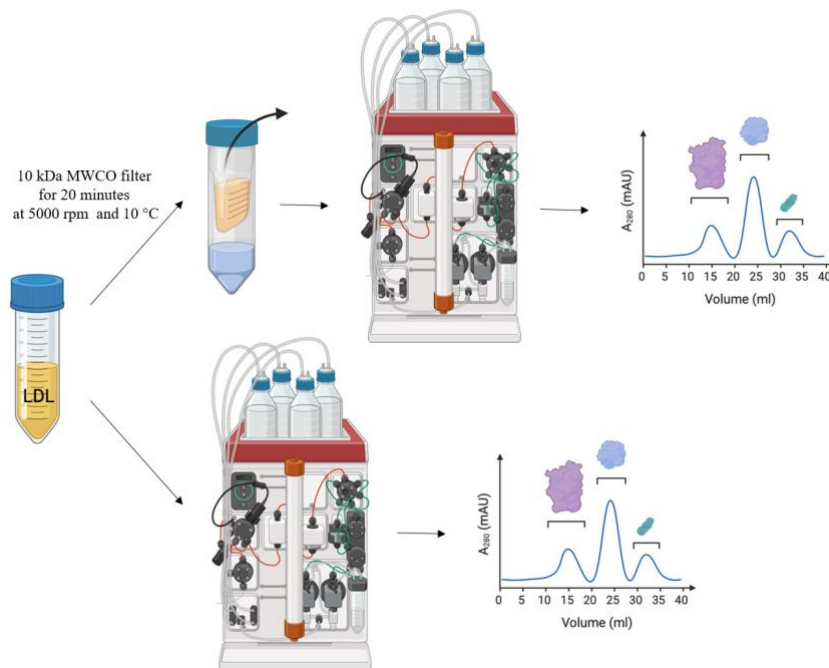


**Figure 7** – Schematic representation of the steps after DGUC.

The sample absorption at 280 nm is automatically recorded and applied to group different fractions based on absorption peaks. For collection, the fraction size is kept at 0.5 mL. Liquids from the same peak are collected. Specifically, peak 1 includes fractions 5, 6 and 7 and it corresponds to 8-9 mL of the elution volume, while peak 2 and peak 3 consist of fractions 13 and 14 and fractions 17, 18 and 19, respectively, as shown in Figure 8.

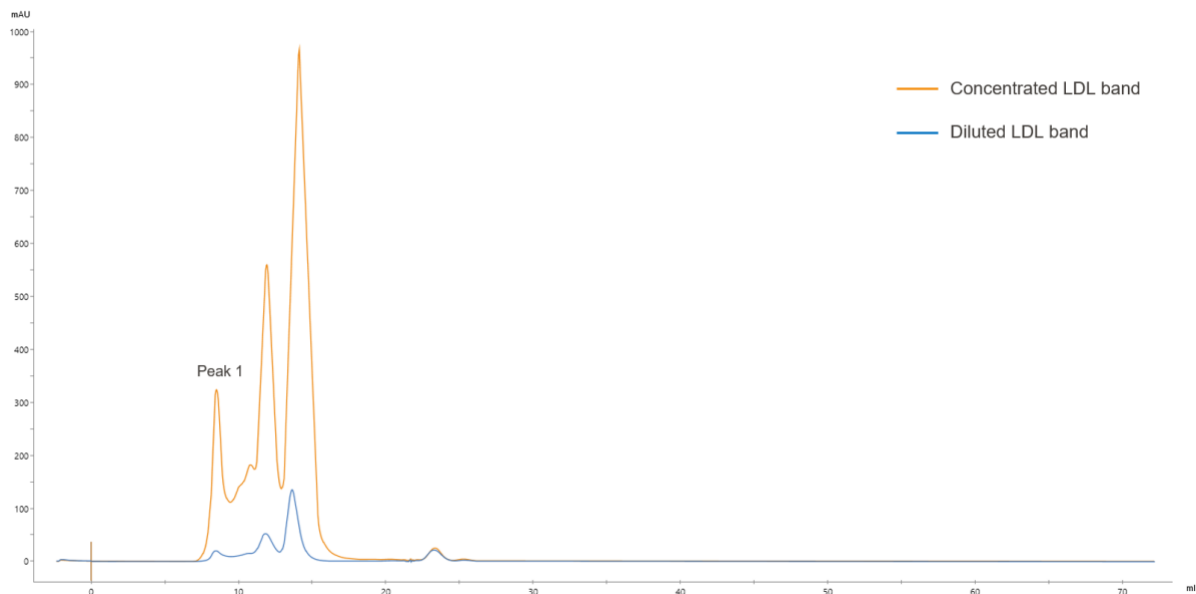


**Figure 8** – Chromatograms obtained from FPLC. In blue and orange are reported the diluted and the concentrated LDL band with a 10 kDa MWCO filter, respectively.

### 3.1.2 2<sup>nd</sup> Protocol without Staining

The protocol established by Redgrave et al. [44] is employed with modifications. A discontinuous density gradient is prepared into a 38.5 mL Ultra-Clear centrifuge tube. The solutions are carefully introduced into the centrifuge tube using a syringe with a large needle. Each solution is sequentially layered from the bottom to the top in order of increasing density. 4 mL of solution A with density at 1.006 g/mL, followed by 9 mL of a solution containing 1.017 g of NaBr per 100 mL of solution A to reach density at 1.019 g/mL, marked as solution B, are layered into the tube. Solution C, composed of 9 mL of 7.83 g of NaBr per 100 mL of solution A to reach density at 1.063 g/mL, is then layered. The final layer consists of 9 mL of Human Serum H5667, adjusted to density at 1.21 g/mL by adding potassium bromide (KBr) at a concentration of 0.325 g per mL of serum.

The prepared tubes are placed into the rotor of the Optima XPN-80 Ultracentrifuge equipped with a swinging-bucket rotor SW32. The samples are centrifuged at 31500 rpm and 8 °C for 48 hours, as shown in Figure 9.

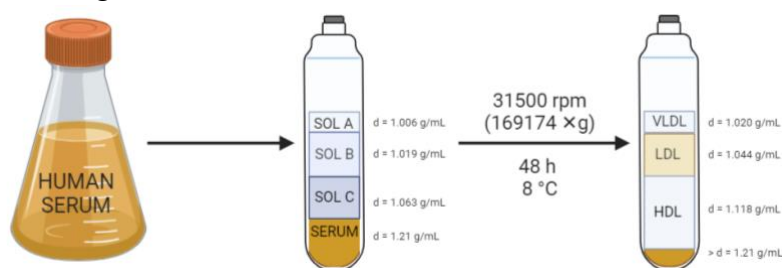


**Figure 9** – Schematic representation of the 2<sup>nd</sup> protocol for LDL extraction.

Following ultracentrifugation, the upper 5 mL of the gradient, corresponding to the very low-density lipoproteins (VLDL) fraction, is carefully removed and discarded using a pipette with a cut tip. The visible 8 mL of yellow band (Figure 10), representing the LDL fraction, is then collected, while the remaining 18 mL are discarded.

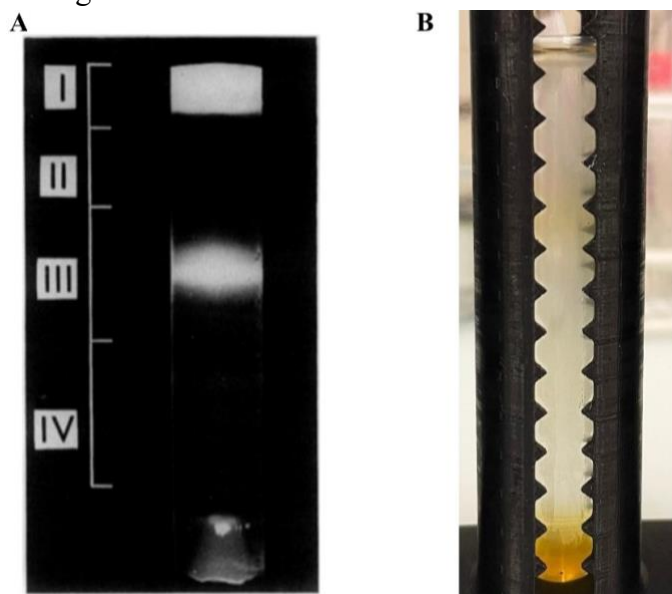


**Figure 10** – Photographs of the gradient in the centrifuge tube following lipoproteins separation. (A) In band III, LDL is clearly visible as a distinct orange-yellow band [44]. (B) Consistently with findings from [44], the formation of band III, corresponding to LDL, is also observed in this experiment.

An additional centrifugation at 31500 rpm and 8 °C for 24 hours is performed by first adding 4 mL solution A, followed by the previously collected LDL band (Figure 11). 9 mL is collected starting from the top using a pipette with a cut tip.

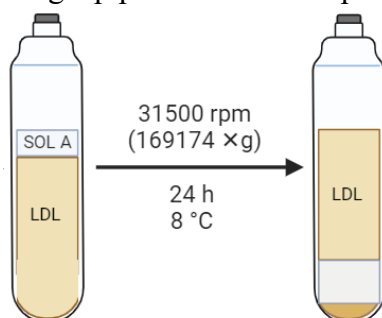


**Figure 11** – Schematic representation of the 2<sup>nd</sup> run of centrifuge.

LDL is purified from the collected bands using SEC.

Two injections are performed into the column using a 500  $\mu$ L capillary loop, and a flow rate of 0.75 mL/min: 500  $\mu$ L of the LDL band collected after a single centrifugation step (LDL band UC1) and another 500  $\mu$ L of the LDL band collected after two centrifugation steps (LDL band UC2) after concentrating them using Amicon Ultra-15 Centrifugal Filters Ultracel-100K (20 min, 5000 rpm, 10 °C), before injection into the FPLC system. The sample absorption at 280 nm is automatically recorded and applied to group different fractions based on absorption peaks. For collection, the fraction size is kept at 0.5 mL. Liquids from the same peak are collected. Specifically, the only peak (Figure 12) includes fractions 5, 6 and 7 and it corresponds to 8-9 mL of the elution volume.

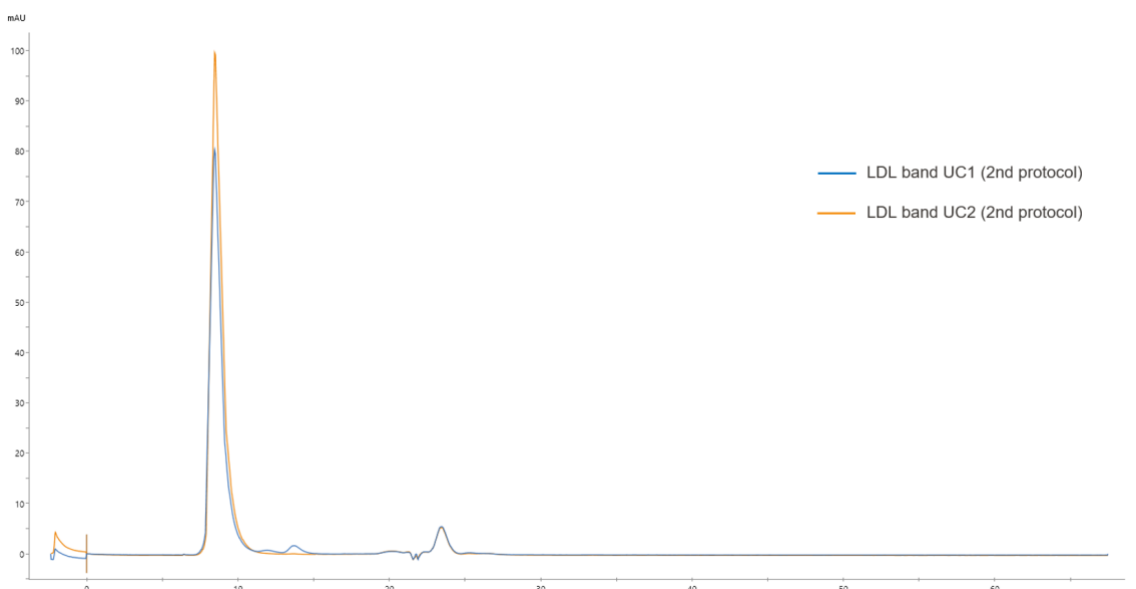


**Figure 12** – Chromatograms obtained from FPLC. In blue and orange are reported the LDL band collected from 2<sup>nd</sup> protocol after the first and second centrifuge, respectively.

### 3.1.3 2<sup>nd</sup> Protocol with Staining

The protocol established by Redgrave et al. [44] is employed with modifications. Specifically, Sudan Red 7B is prepared at a concentration of 8.5 mg/mL in acetone. A discontinuous density gradient is prepared in a 38.5 mL Ultra-Clear centrifuge tube (25 × 89 mm). The solutions are carefully introduced into the centrifuge tube using a syringe with a large needle, ensuring sequential layering from the bottom up in order of increasing density.

The gradient consists of 4 mL of solution A with density at 1.006 g/mL, followed by 9 mL of solution B with density at 1.019 g/mL. 9 mL of solution C with density at 1.063 g/mL is then layered. The final layer consists of 9 mL of Human Serum H5667, adjusted to a density of 1.21 g/mL by adding KBr at a concentration of 0.325 g per mL of serum, with 300 µL of Sudan Red 7B dye (Figure 13A).

The prepared tubes are placed into the rotor of the Optima XPN-80 Ultracentrifuge equipped with a swinging-bucket rotor SW32. The samples are centrifuged at 31500 rpm and 8 °C for 48 hours.

Following ultracentrifugation, the upper 5 mL of the gradient, corresponding to the VLDL fraction, is carefully removed with a pipette. The visible 8 mL of reddish band (Figure 13B), representing the LDL fraction, is then collected, while the remaining 18.3 mL are discarded.

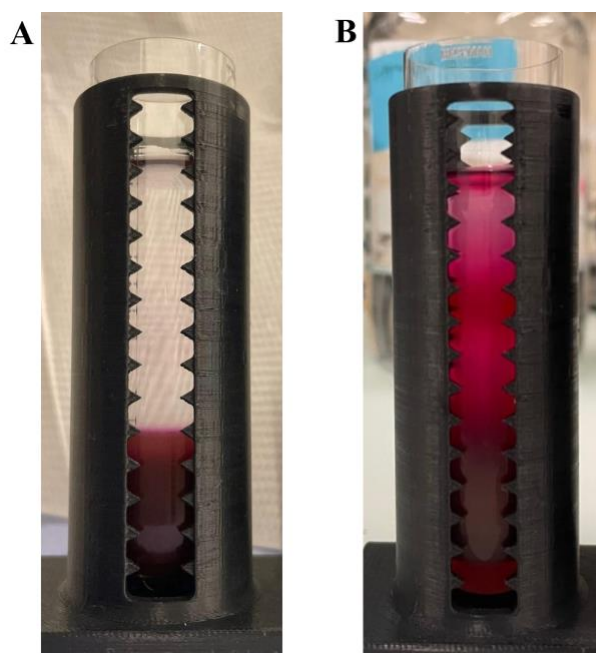


**Figure 13** – Photographs of the gradient in the centrifuge tube (A) before and (B) after centrifuge.

Stained LDL is purified using SEC. The collected band is concentrated using Amicon Ultra-15 Centrifugal Filters Ultracel-100K (20 min, 5000 rpm, 10 °C).

It is performed one injection into the column using a 500 µL capillary loop, and a flow rate of 0.75 mL/min. The obtained fraction is labeled as LDL-S.

### 3.1.4 2<sup>nd</sup> Protocol with PEG Precipitation

5 mL of the LDL band collected after DGUC is concentrated using Amicon Ultra-15 Centrifugal Filters Ultracel-100K under 5500 rpm, 4 °C until the total volume is 0.6 mL. The concentrated sample is then diluted to a final volume of 6.0 mL with 1X PBS and centrifuged at  $17000 \times g$  for 30 minutes at 4 °C using the Sorvall Legend X1R Centrifuge.

The sample is filtered through a 0.45  $\mu\text{m}$  polyethersulfone (PES) membrane. 1.2 mL of a 50% (w/v) PEG 10K solution is added to the supernatant. After thorough vortexing, the sample is incubated at 4 °C for 1 hour and then centrifuged at  $1800 \times g$  for 15 minutes at 4 °C using the same centrifuge. The supernatant is carefully discarded, and the sedimented lipoproteins are resuspended in 0.7 mL of 1X PBS. Complete dissolution of the pellet is achieved through vortexing and sonication using an ultrasonic bath. The outlined procedure is shown in Figure 14.

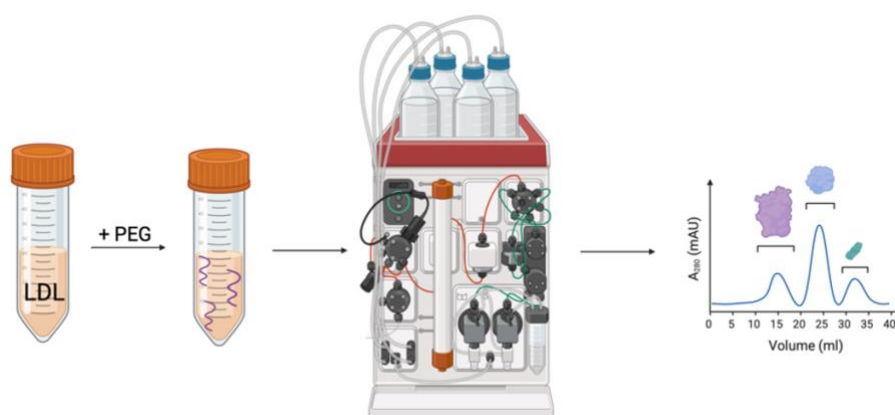


**Figure 14** – Schematic representation of the procedure outlined above.

LDL is purified after PEG precipitation using SEC. It is performed one injection into the column using a 500  $\mu\text{L}$  capillary loop, and a flow rate of 0.75 mL/min. The fractions 5, 6, 7, corresponding to 8-9 mL of the elution volume, are collected (Figure 15).

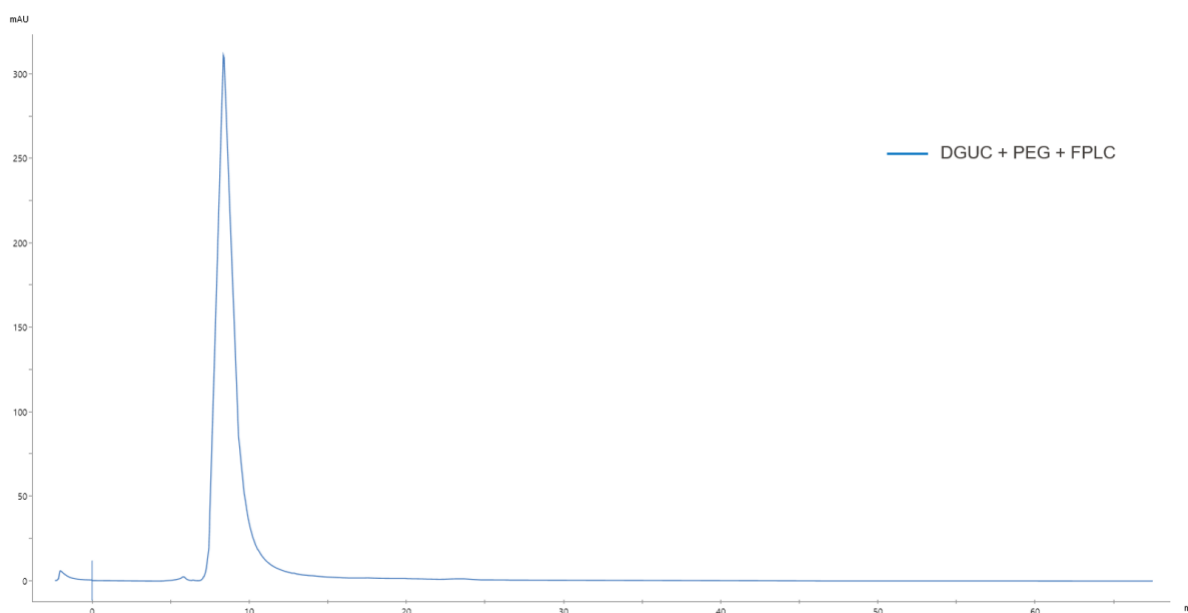


**Figure 15** – Chromatogram obtained through FPLC according to the outlined protocol.

### 3.1.5 2<sup>nd</sup> Protocol with Filtering Several Times

After collecting the LDL band following DGUC, 5 mL is subjected to multiple filtrations using a Amicon Ultra-15 Centrifugal Filters Ultracel-100K under 5500 rpm, 4 °C until the total volume is 0.6 mL.

Subsequently, FPLC is performed. It is performed one injection into the column using a 500  $\mu$ L capillary loop, and a flow rate of 0.75 mL/min. The procedure is shown in Figure 16.

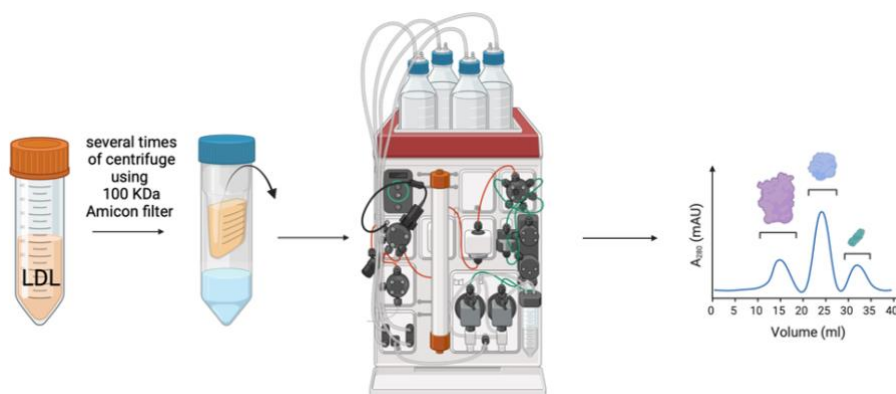


**Figure 16** – Schematic representation of the procedure outlined above.

The only peak is collected, and it includes fractions 5, 6 and 7 and it corresponds to 8-9 mL of the elution volume (Figure 17).

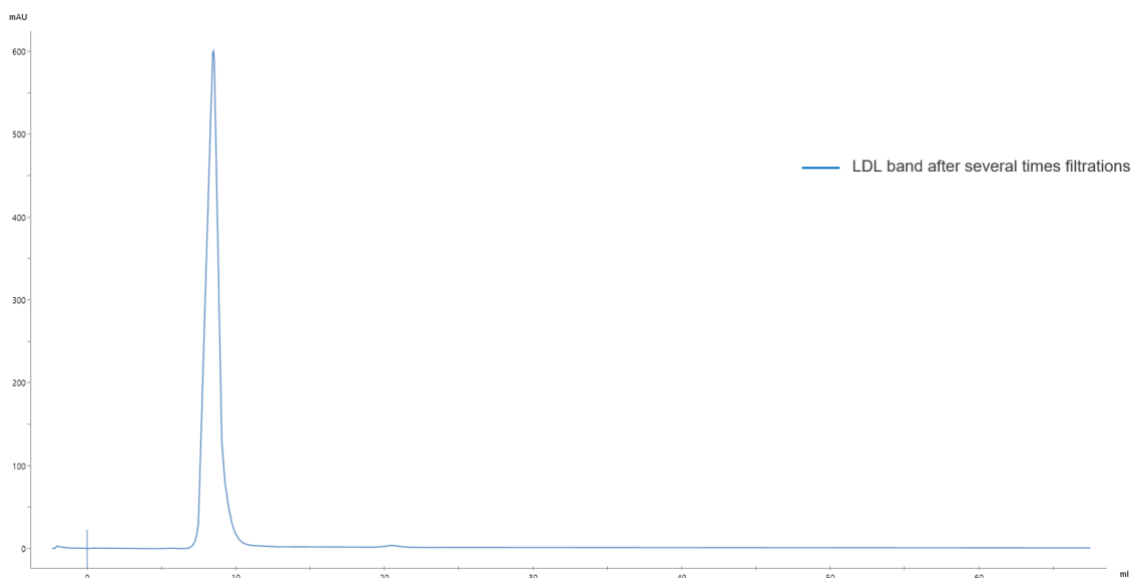


**Figure 17** – Chromatogram obtained from FPLC of the several times filtrated LDL band collected after DGUC.

### 3.1.6 SEC-based purification of commercial LDL

In this thesis, commercial LDL are used as model lipoprotein nanoparticles. These LDL particles are provided at a concentration of 2.5 mg/mL. 200  $\mu$ L of commercial LDL are taken and diluted to 600  $\mu$ L with 1X PBS. Prior to further use, the commercial LDL sample undergoes purification through FPLC. It is performed one injection into the column using a 500  $\mu$ L capillary loop, and a flow rate of 0.75 mL/min.

The only peak is collected, and it includes fractions 6, 7 and 8 and it corresponds to  $\sim$ 9 mL of the elution volume (Figure 18).

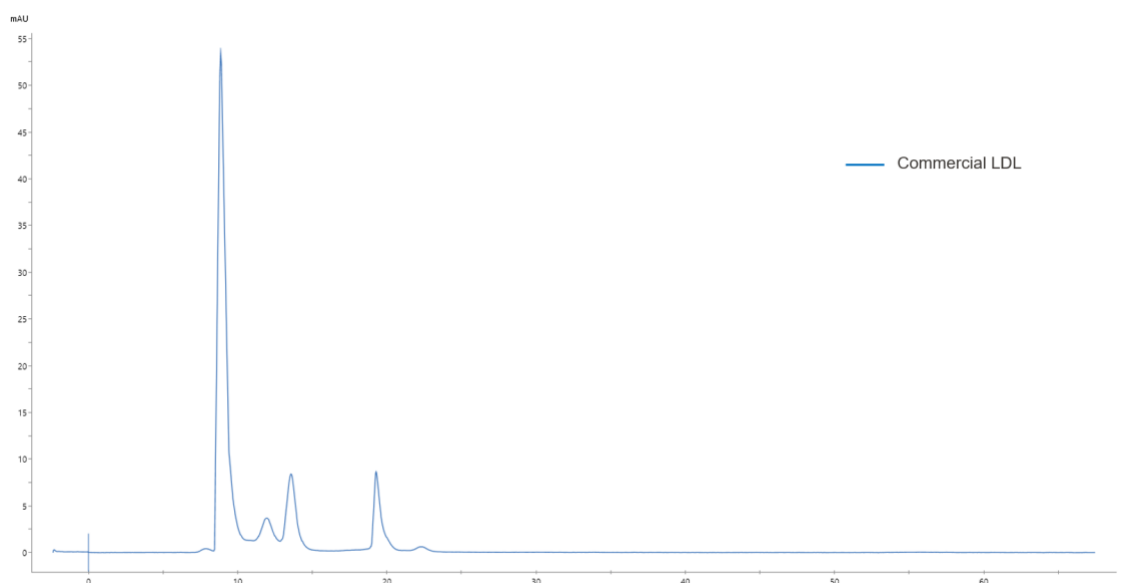


**Figure 18** – Chromatogram obtained from FPLC of the commercial LDL sample.

## 3.2 LDL and Protein Incubation Procedure

### 3.2.1 Interactions between LDL particles and Human Serum Albumin (HSA)

1.5 mL of the LDL solution from 3.1.2 is incubated with albumin from human serum (HSA). Specifically, 0.3 mL of the sample is mixed with 0.3 mL of protein at the desired final concentration. To obtain a final concentration of 60  $\mu$ M in 0.6 mL, 2.4 mg of HSA is weighed and dissolved in 0.3 mL of PBS. Similarly, to achieve a final concentration of 602  $\mu$ M in 0.6 mL, 24.0 mg of HSA is weighed and dissolved in 0.3 mL of PBS, and for the 1503  $\mu$ M in 0.6 mL, 60.0 mg of HSA is weighed and dissolved in 0.3 mL of PBS.

Five different incubations are performed: one with LDL with 0  $\mu$ M of HSA as a control, and four with LDL mixed with HSA at different concentrations and conditions. The 60  $\mu$ M and 602  $\mu$ M incubations are carried out overnight at 4°C, while an additional 602  $\mu$ M incubation is performed for 1 hour at 37°C. Lastly, LDL is also incubated with HSA at 1503  $\mu$ M overnight at 4°C.

After the incubations, FPLC is performed again, and the LDL peak fraction (elution volume  $\sim$ 8–9 mL) is collected (Figure 19, Figure 20). A total of 1.5 mL from fractions 5, 6, and 7 is then individually concentrated using Amicon Ultra-15 Centrifugal Filters Ultracel-30K at 1800  $\times$  *g* and 8°C until the optical density (OD) reaches a value between 0.2 and 1.2.

The optical density is measured using a Nanophotometer (Implen). The instrument is blanked with PBS. A drop of the sample is then placed on the measurement surface, and the optical density (OD) is recorded.

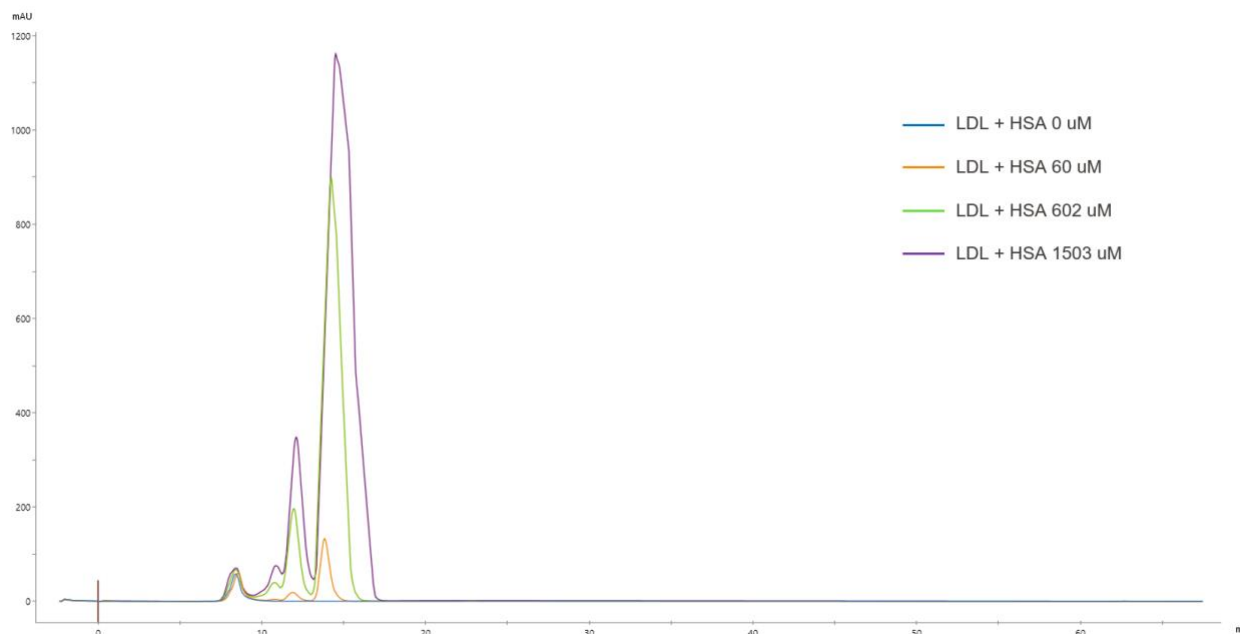


**Figure 19** – Chromatogram obtained from FPLC of the LDL with HSA at different concentrations overnight at 4°C.

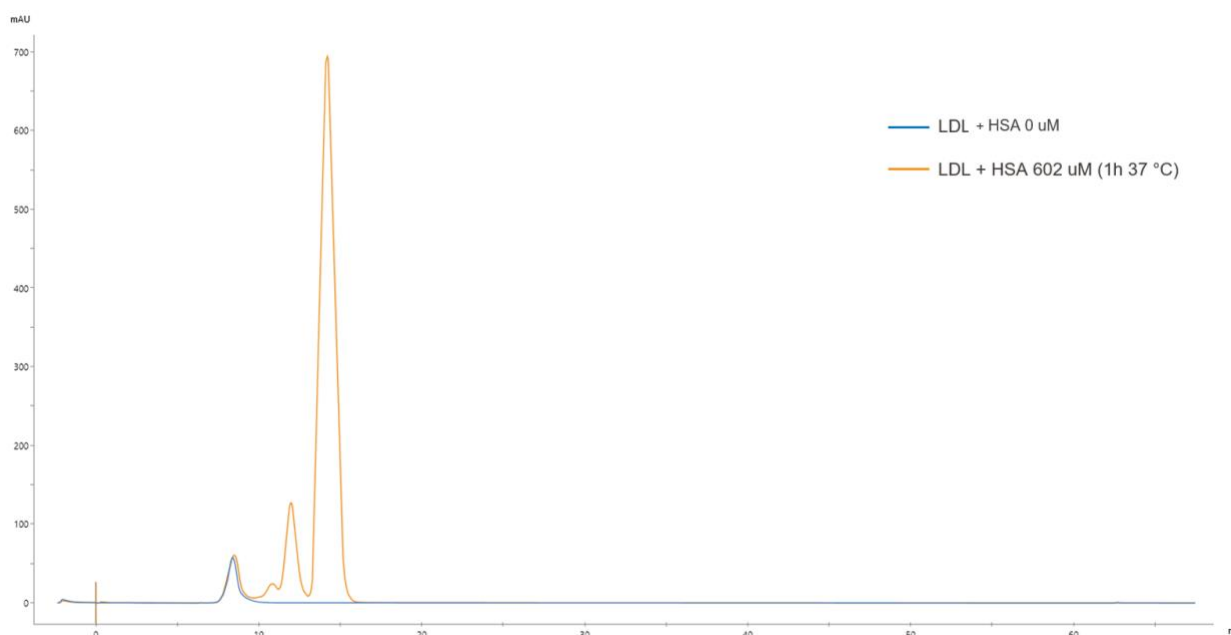


**Figure 20** – Chromatogram obtained from FPLC of the LDL with HSA at 602 μM, 1h at 37°C.

### 3.2.2 Interactions between stained LDL particles and HSA

0.3 mL of LDL-S from 3.1.3 is mixed and incubated with 0.3 mL of HSA with its concentration at 0 μM, 1503 μM, respectively overnight 4°C.

Following incubation, FPLC is carried out again, and the LDL peak fraction (elution volume ~8–9 mL) is collected (Figure 21).

Subsequently, 1.5 mL from fractions 5, 6, and 7 is concentrated using Amicon Ultra-15 Centrifugal Filters Ultracel-30K at  $1800 \times g$  and  $8^{\circ}\text{C}$  until the optical density (OD) falls within the range of 0.2–1.2.

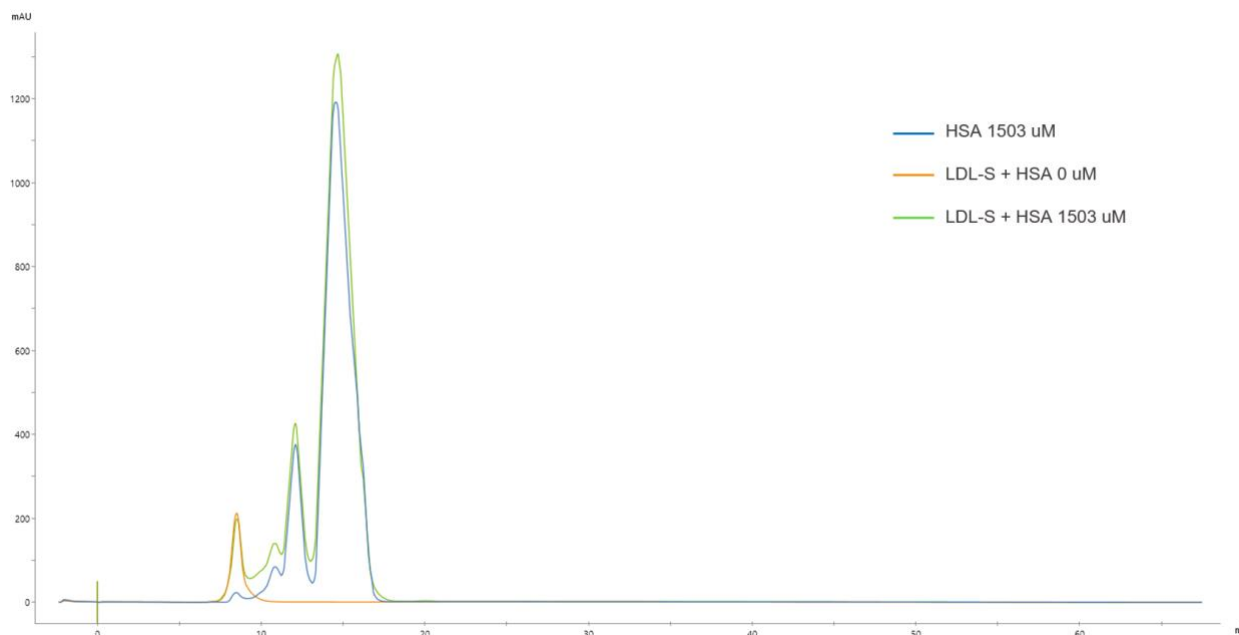


**Figure 21** – Chromatograms obtained from FPLC of LDL stained and HSA 1503  $\mu\text{M}$ , overnight  $4^{\circ}\text{C}$ .

### 3.2.3 Interactions between LDL particles and Immunoglobulin G (IgG)

0.3 mL of the LDL solution from 3.1.2 is mixed and incubated with 0.3 mL of immunoglobulin (IgG) to achieve the desired final concentration.

Three incubations are performed with IgG  $0 \mu\text{M}$ ,  $6.7 \mu\text{M}$ ,  $80 \mu\text{M}$ , overnight at  $4^{\circ}\text{C}$ .

To obtain a final concentration of  $6.7 \mu\text{M}$  in 0.6 mL, 0.6 mg of IgG is weighed and dissolved in 0.3 mL of PBS. Similarly, to achieve a final concentration of  $80 \mu\text{M}$  in 0.6 mL, 7.2 mg of IgG is weighed and dissolved in 0.3 mL of PBS. Figure 22 shows chromatograms of IgG at different concentrations.

Following incubation, FPLC is carried out again, and the LDL peak fraction (elution volume  $\sim 8\text{--}9 \text{ mL}$ ) is collected (Figure 22B).

Subsequently, 1.5 mL from fractions 5, 6, and 7 is individually concentrated using Amicon Ultra-15 Centrifugal Filters Ultracel-30K at  $1800 \times g$  and  $8^{\circ}\text{C}$  until the optical density (OD) falls within the range of 0.2–1.2.

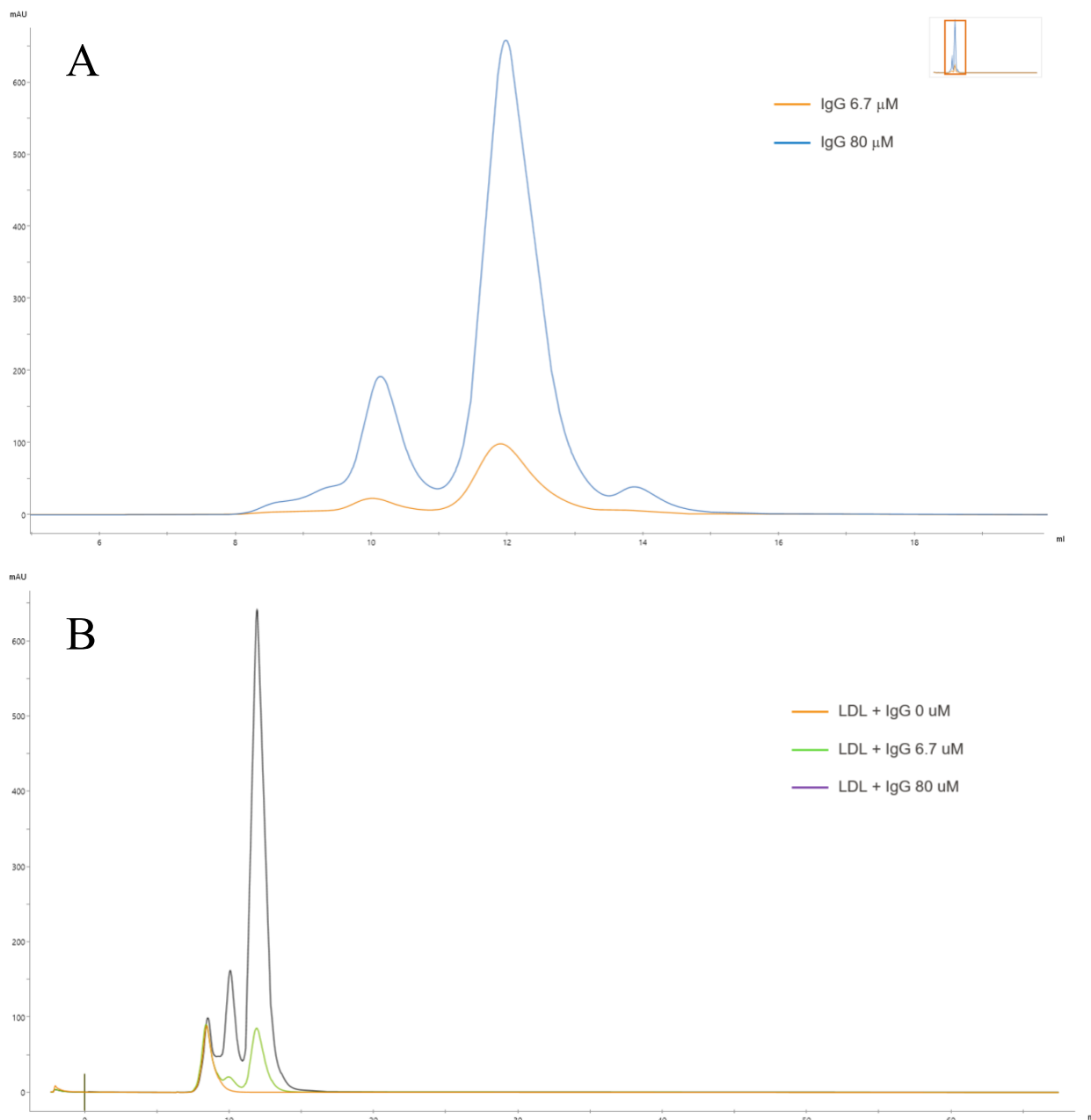


**Figure 22** – (A) Chromatogram obtained from FPLC of IgG at different concentration. (B) Chromatogram obtained from FPLC of mixing LDL and IgG at different concentrations, overnight 4°C.

0.3 mL of the LDL solution from 3.1.2 is mixed with 0.3 mL of IgG to achieve the desired final concentration.

Five incubations are performed with IgG 0  $\mu$ M, 6.7  $\mu$ M, 20  $\mu$ M, 40  $\mu$ M, 80  $\mu$ M overnight at 4°C. To obtain a final concentration of 20  $\mu$ M in 0.6 mL, 1.8 mg of IgG is weighed and dissolved in 0.3 mL of PBS. Similarly, to achieve a final concentration of 40  $\mu$ M in 0.6 mL, 3.6 mg of IgG is weighed and dissolved in 0.3 mL of PBS.

Following incubation, FPLC is carried out again, and the LDL peak fraction (elution volume  $\sim$ 8–9 mL) is collected (Figure 23).

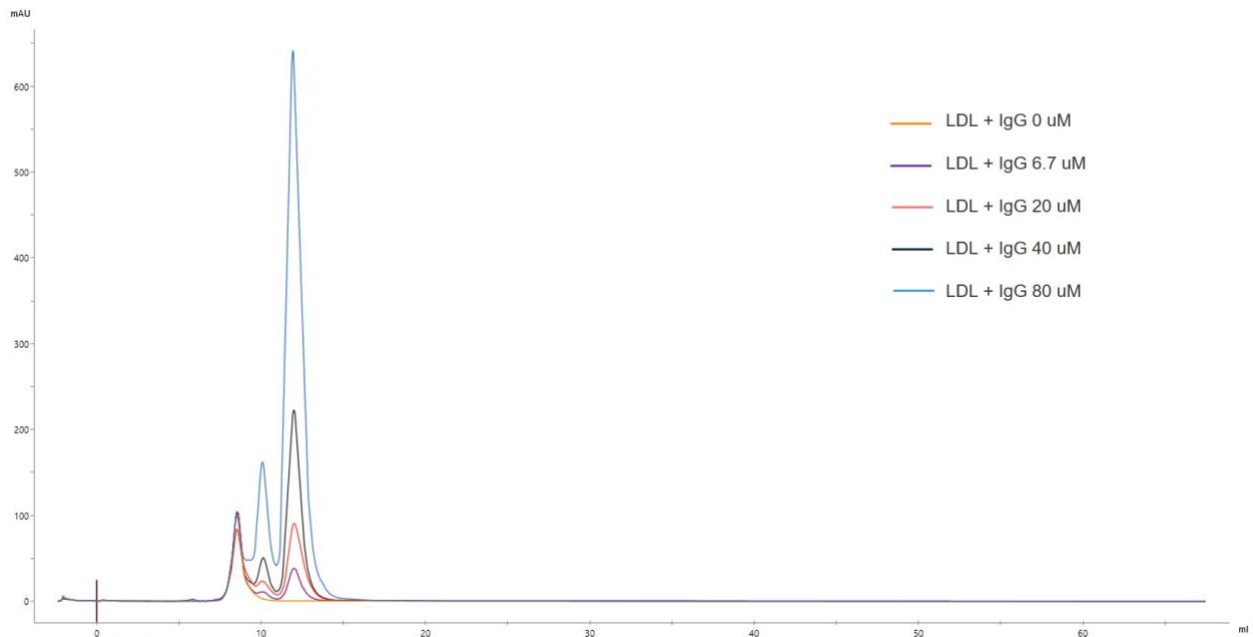


**Figure 23** – Chromatogram obtained from FPLC of mixing LDL and IgG at different concentrations, overnight 4°C.

Additionally other four incubations are performed with IgG 0  $\mu\text{M}$ , 80  $\mu\text{M}$  at different conditions. Specifically, LDL is incubated with IgG overnight at 4°C, for 1 hour at 37°C and also overnight at 37°C.

Following incubation, FPLC is carried out again, and the LDL peak fraction (elution volume  $\sim$ 8–9 mL) is collected (Figure 24).

Subsequently, 1.5 mL from fractions 5, 6, and 7 is individually concentrated using Amicon Ultra-15 Centrifugal Filters Ultracel-30K at  $1800 \times g$  and 8°C until the optical density (OD) falls within the range of 0.2–1.2.

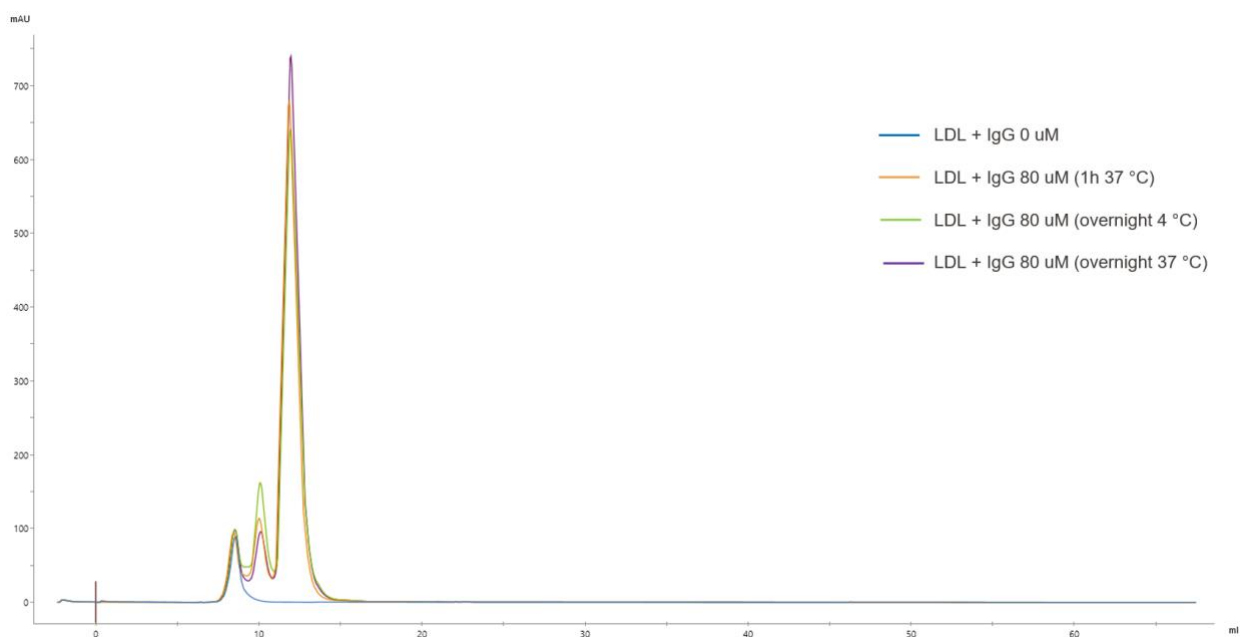


**Figure 24** – Chromatogram obtained from FPLC of mixing LDL and IgG 80, overnight 4°C, overnight 37°C, 1h 37°C.

0.3 mL of the LDL solution from 3.1.5 is mixed with 0.3 mL of IgG to achieve the desired final concentration.

Three incubations are performed with IgG 0  $\mu\text{M}$ , 20  $\mu\text{M}$ , 80  $\mu\text{M}$  overnight at 4°C. Following incubation, FPLC is carried out again, and the LDL peak fraction (elution volume ~8–9 mL) is collected (Figure 25).

Subsequently, 1.5 mL from fractions 5, 6, and 7 is individually concentrated using Amicon Ultra-15 Centrifugal Filters Ultracel-30K at  $1800 \times g$  and 8°C until the optical density (OD) falls within the range of 0.2–1.2.

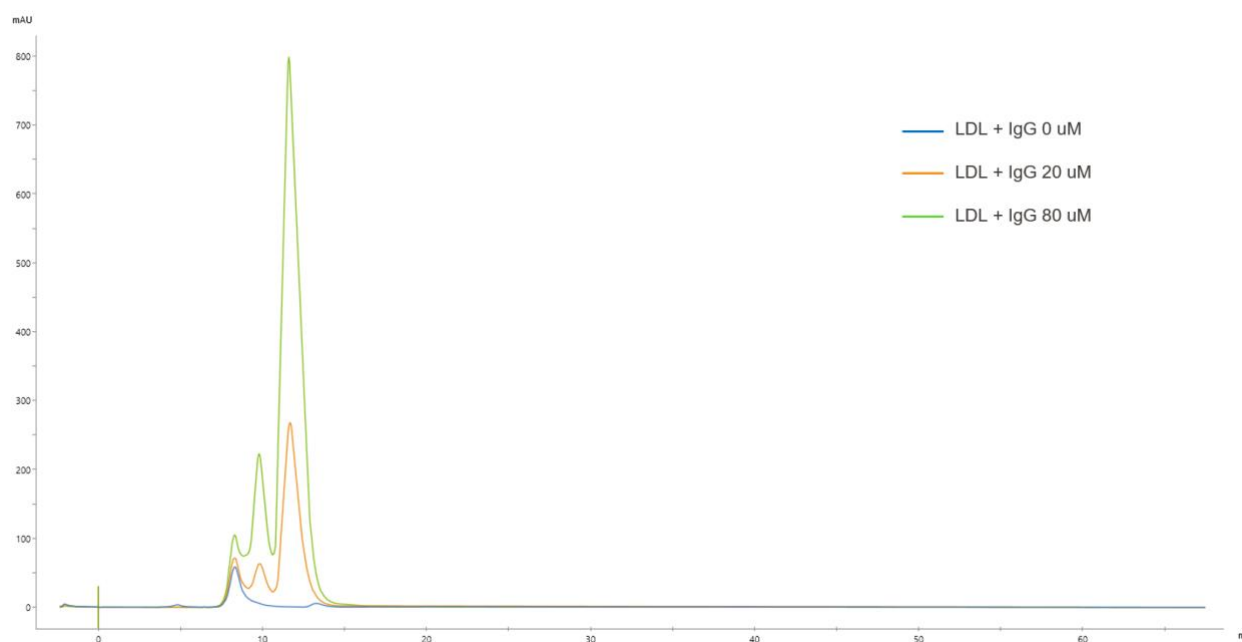


**Figure 25** – Chromatogram obtained from FPLC of mixing LDL and IgG at different concentrations, overnight 4°C.

### 3.2.4 Interactions between stained LDL particles and IgG

0.3 mL of the LDL-S solution from 3.1.3 is mixed with 0.3 mL of IgG at the desired final concentration.

Five incubations are performed with IgG 0  $\mu\text{M}$ , 80  $\mu\text{M}$ , 160  $\mu\text{M}$ , 320  $\mu\text{M}$ , 480  $\mu\text{M}$  overnight at 4°C. Following incubation, FPLC is carried out again, and the LDL peak fraction (elution volume ~8–9 mL) is collected (Figure 26).

To obtain a final concentration of 160  $\mu\text{M}$  in 0.6 mL, 14.4 mg of IgG is weighed and dissolved in 0.3 mL of PBS. Similarly, to achieve a final concentration of 320  $\mu\text{M}$  in 0.6 mL, 28.8 mg of IgG is weighed and dissolved in 0.3 mL of PBS and for 320  $\mu\text{M}$  in 0.6 mL, 57.6 mg of IgG is weighed and dissolved in 0.3 mL of PBS.

Subsequently, 1.5 mL from fractions 5, 6, and 7 is concentrated using Amicon Ultra-15 Centrifugal Filters Ultracel-30K at  $1800 \times g$  and 8°C until the optical density (OD) falls within the range of 0.2–1.2.

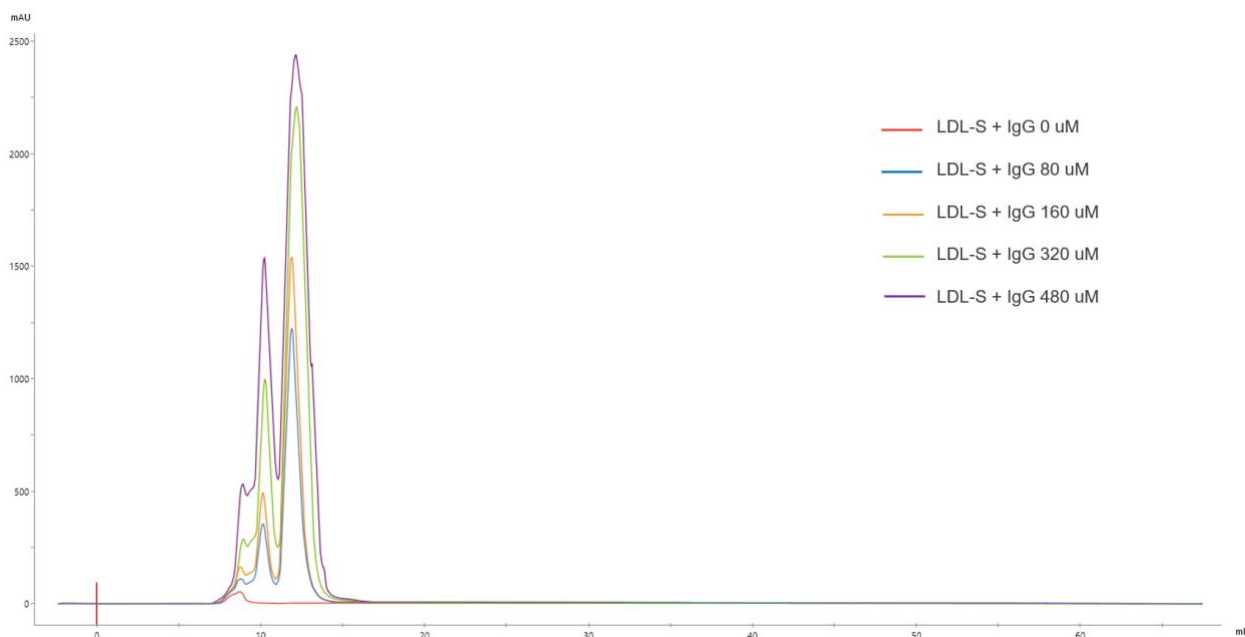


**Figure 26** – Chromatogram obtained from FPLC of mixing stained LDL and IgG at different concentrations, overnight 4°C.

### 3.2.5 Interactions between LDL particles with HSA and IgG

A stock solution of HSA and IgG, at a 7.53:1 concentration ratio, is diluted 2, 4, and 8 times, maintaining the optical density within the range of 0.2-1.2.

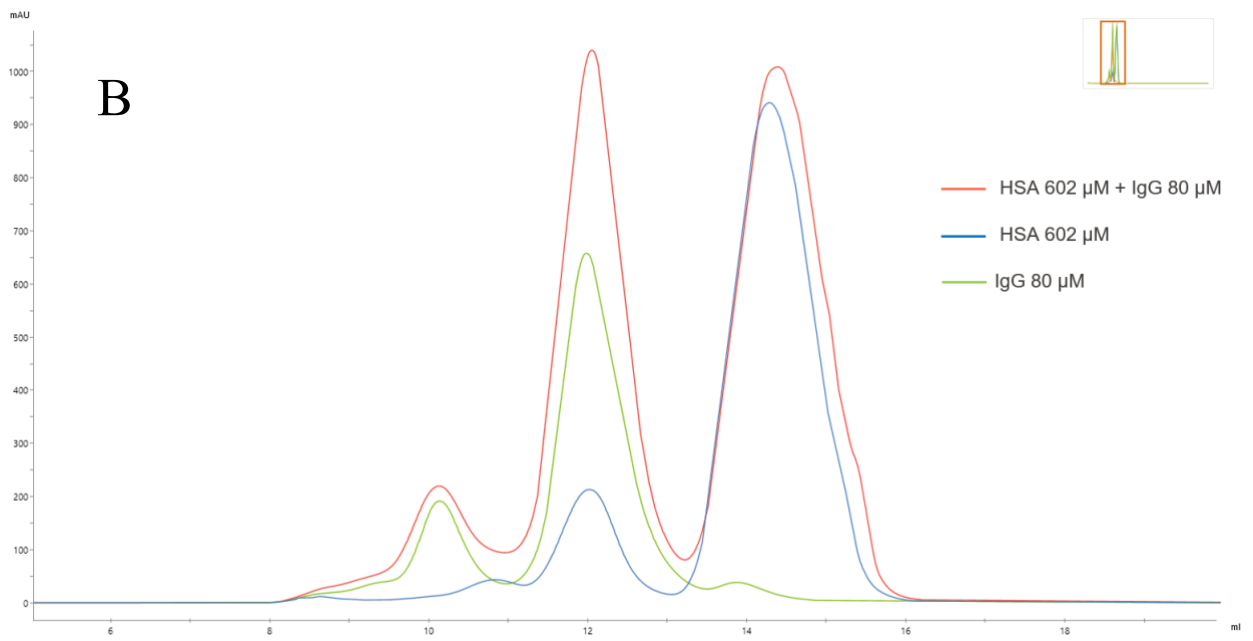
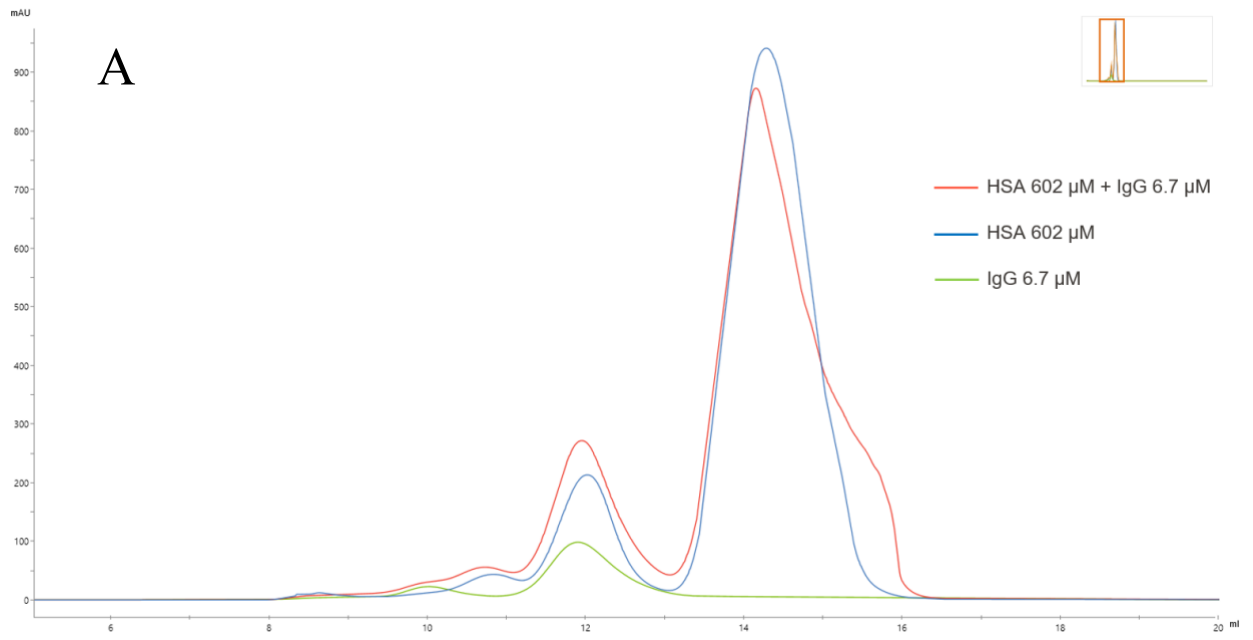
0.3 mL of the LDL solution from 3.1.2 is mixed with 0.3 mL of with HSA at a fixed concentration and IgG at different concentrations.

To obtain a final concentration of HSA 602  $\mu\text{M}$  and IgG 6.7  $\mu\text{M}$  in 0.6 mL, 0.6 mg of IgG is weighed and dissolved with 24.0 mg of HSA in 0.3 mL of PBS. Similarly, to achieve a final concentration of HSA 602  $\mu\text{M}$  and IgG 80  $\mu\text{M}$  in 0.6 mL, 7.2 mg of IgG is weighed and dissolved with 24.0 mg of HSA in 0.15 mL of PBS.

The mixture of HSA and IgG is illustrated in Figure 27A and Figure 27B.

Three incubations are performed with IgG 0  $\mu\text{M}$ , 6.7  $\mu\text{M}$ , 80  $\mu\text{M}$  overnight at 4°C. Following incubation, FPLC is carried out again, and the LDL peak fraction (elution volume ~8–9 mL) is collected (Figure 27).

Subsequently, 1.5 mL from fractions 5, 6, and 7 is concentrated using Amicon Ultra-15 Centrifugal Filters Ultracel-30K at 1800  $\times g$  and 8°C until the optical density (OD) falls within the range of 0.2–1.2.



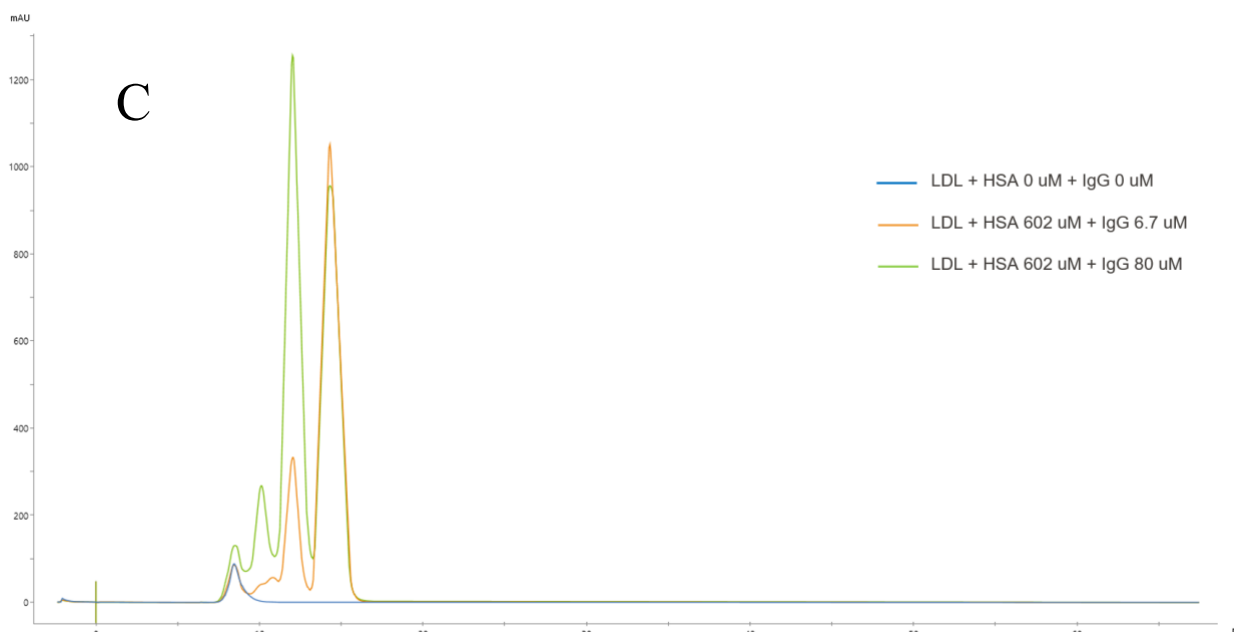


**Figure 27** – (A) Chromatogram of mixture of HSA 602  $\mu\text{M}$  and IgG 6.7  $\mu\text{M}$ . (B) Chromatogram of mixture of HSA 602  $\mu\text{M}$  and IgG 80  $\mu\text{M}$ . (C) Chromatogram obtained from FPLC of mixing LDL, HSA 602  $\mu\text{M}$  and IgG at different concentrations, overnight 4°C.

### 3.2.6 Interactions between LDL particles and Apo-Transferrin

0.3 mL of LDL solution from 3.1.2 is mixed with 0.3 mL of Apo-Transferrin at the desired final concentration.

Two incubations are performed with Apo-Transferrin 0  $\mu\text{M}$ , 37.7  $\mu\text{M}$ , overnight at 4°C. To obtain a final concentration of Apo-Transferrin 3  $\mu\text{M}$  in 0.6 mL, 1.8 mg of Apo-Transferrin is weighed and dissolved in 0.3 mL of PBS.

Following incubation, FPLC is carried out again, and the LDL peak fraction (elution volume  $\sim$ 8–9 mL) is collected (Figure 28).

Subsequently, 1.5 mL from fractions 5, 6, and 7 is concentrated using Amicon Ultra-15 Centrifugal Filters Ultracel-30K at 1800  $\times g$  and 8°C until the optical density (OD) falls within the range of 0.2–1.2.

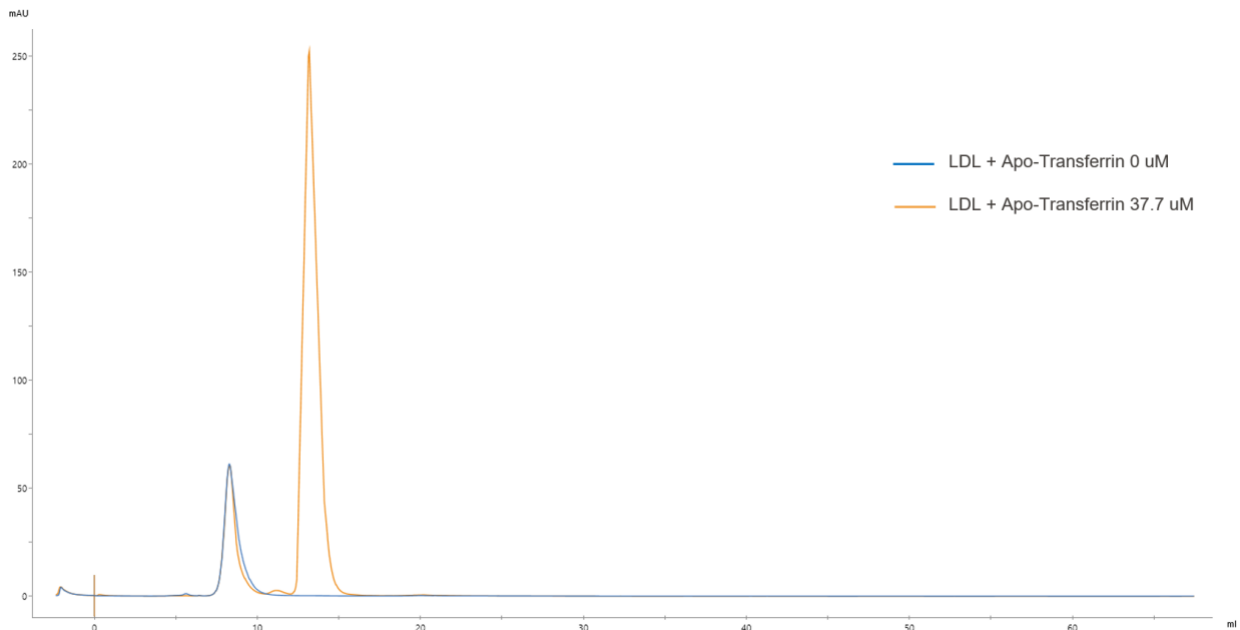


**Figure 28** – Chromatogram obtained from FPLC of mixing LDL and Apo-Transferrin 37.7  $\mu\text{M}$ , overnight 4°C.

0.3 mL of LDL solution from 3.1.5 is mixed with 0.3 mL of Apo-Transferrin to achieve the desired final concentration.

Two incubations are performed with Apo-Transferrin 0  $\mu\text{M}$  and 37.7  $\mu\text{M}$ , overnight at 4°C.

Following incubation, FPLC is carried out again, and the LDL peak fraction (elution volume ~8–9 mL) is collected (Figure 29).

Subsequently, 1.5 mL from fractions 5, 6, and 7 is concentrated using Amicon Ultra-15 Centrifugal Filters Ultracel-30K at  $1800 \times g$  and 8°C until the optical density (OD) falls within the range of 0.2–1.2.

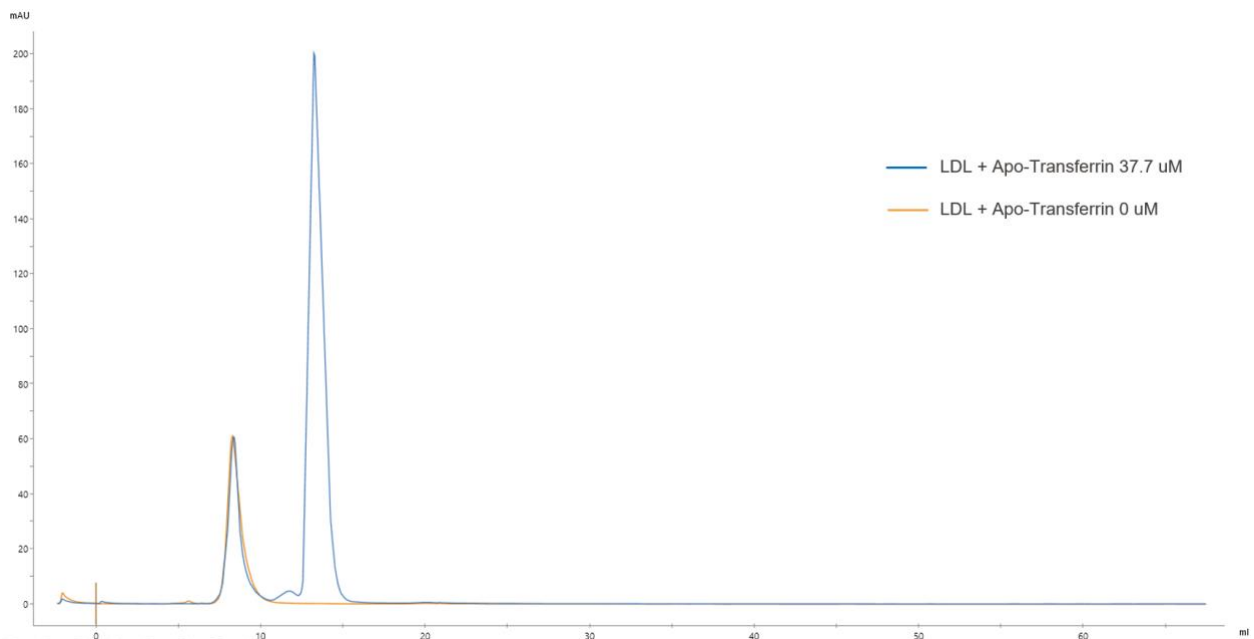


**Figure 29** – Chromatogram obtained from FPLC of mixing LDL filtered several times and Apo-Transferrin 37.7  $\mu\text{M}$ , overnight 4°C.

### 3.3 Characterization Techniques for Isolated LDL

#### 3.3.1 FPLC

FPLC is a medium-pressure technique used for protein purification. It utilizes a peristaltic pump to ensure a stable flow rate, while injection valves regulate the eluent composition [45]. The system is automated, integrating sample injectors, gradient controllers, and detectors to monitor separation efficiency [45].

For these experiments, the Superdex 200 Increase 10/300 GL column is used with an ÄKTA go™ system (Figure 30). This SEC column, composed of a cross-linked agarose and dextran matrix, enables the separation of proteins ranging from 10 to 600 kDa. It has a total volume of 24 mL, operates at flow rates between 0.5 and 1.5 mL/min, and can withstand pressures up to 5 MPa [46].

Proper column maintenance and sample preparation are essential. The process begins with selecting an appropriate buffer, typically 1X PBS. Before sample injection, the column must be equilibrated with at least two column volumes of PBS. After use, thorough washing with a PBS volume four times greater than the loop volume is required.

Sample volume and concentration are also critical factors. The Superdex 200 Increase 10/300 GL column is designed for protein concentrations between 1–5 mg/mL. In this thesis, a 500 µL injection loop is used, determining the injection volume.



Figure 30 – ÄKTA go™ protein purification system from Cytiva.

### **3.3.2 Sodium Dodecyl Sulphate-PolyAcrylamide Gel Electrophoresis (SDS-PAGE)**

Sodium Dodecyl Sulphate-PolyAcrylamide Gel Electrophoresis (SDS-PAGE) is a technique used to separate proteins primarily by their molecular weight. In this method, proteins are treated with SDS, which imparts a uniform negative charge to them.

To perform SDS-PAGE, a NuPAGE™ 4-12% Bis-Tris Gel (1.0 mm × 12 well) is used in combination with NuPAGE™ MES SDS Running Buffer (20×). The running buffer is diluted at a 1:20 ratio by mixing 50 mL of the stock solution with 1 L of Milli-Q water. Once prepared, the gel cassette is carefully opened to create the wells for sample loading. The gel is then placed into the electrophoresis chamber, and the running buffer is poured into the chamber to cover the gel.

For sample preparation, 5 µg of protein is taken from each sample, with the corresponding volume calculated based on the protein concentration measured using the Qubit Protein Assay Kit and the Qubit 4 Fluorometer (Thermo Fisher Scientific).

If the samples require reduction, 5 µL of Bolt LDS Sample Buffer (4×) and 5 µL of NuPAGE™ Sample Reducing Agent (10×) are added to each tube. For non-reducing SDS-PAGE, 10 µL of Tricine SDS Sample Buffer (2×) is used instead. A total volume of 20 µL from each prepared sample is then loaded into the wells of the gel. For molecular weight reference, 5 µL of PageRuler Unstained Broad Range Protein Ladder is loaded into one well.

Electrophoresis is carried out at 150 V, 120 mA, and 150 W for a total duration of 45 minutes, during which proteins migrate through a polyacrylamide gel matrix. Once the electrophoresis is complete, the gel is carefully removed from the apparatus and placed into a container with InstantBlue® Coomassie Protein Stain. The protein bands are visualized and imaged using the GelDoc Go Gel Imaging System (Bio Rad).

Under reducing conditions, the bands correspond to the molecular weight of individual polypeptide subunits, while in the absence of reducing agents, the bands reflect the molecular weight of the intact protein [47]. By comparing migration patterns under both conditions, the total protein size and the size of its subunits can be determined [48].

### **3.3.3 Dynamic Light Scattering (DLS)**

Dynamic Light Scattering (DLS) is a technique used to analyze the size distribution of particles, typically in the nanometer to the submicron range, by measuring the scattering of laser light caused by particles in suspension [49]. The scattered light intensity fluctuates due to the random motion of particles driven by Brownian motion [50]. These fluctuations provide insights into the hydrodynamic size and movement of the particles, with smaller particles moving more rapidly than larger ones [50]. However, DLS has limited resolution, which can complicate the accurate characterization of polydisperse samples that contain a wide range of particle sizes.

This technique operates by directing a monochromatic laser at particles suspended in a liquid. As the laser interacts with the particles, it scatters in different directions, creating an interference pattern that fluctuates due to particle motion. These fluctuations are captured by a detector positioned at a fixed angle, typically 90° or 173°, and analyzed for Doppler

broadening [51]. The intensity fluctuations are processed by a digital autocorrelator, which generates a correlation function that provides information about the particles' diffusion coefficients. Using the Stokes-Einstein equation, the hydrodynamic radius of the particles can be determined, reflecting their apparent size, including the hydration shell and solvation layers surrounding them [49].

In this thesis, the Litesizer 500 (Anton Paar) is used to determine the hydrodynamic size and distribution of LDL particles (Figure 31). Specifically, the size distribution chart is generated through the one-page workflow of the Litesizer 100/500 software.

For DLS analysis, samples are prepared in disposable polystyrene cuvettes ( $10 \times 10 \times 45$  mm). The system temperature is kept constant at  $20\text{ }^{\circ}\text{C}$ , and up to 60 scans are performed, each lasting 10 seconds. Measurements are conducted in a backscatter configuration, with a 10 mM NaCl solution used as the solvent to minimize electrostatic interactions between particles.



**Figure 31** – Anton Paar Litesizer 500 Particle Analyzer.

### 3.3.4 Transmission Electron Microscopy (TEM)

Transmission Electron Microscopy (TEM) is a method used for visualizing structures at the atomic level. To produce an image in TEM, a high-energy electron beam is transmitted through an ultra-thin sample, typically less than 100 nm thick, which is transparent to electrons [52]. The microscope consists of a series of electromagnetic lenses and apertures that focus the electron beam onto the sample and magnify the resultant image [53]. This image is then projected onto a phosphor screen or captured by a specialized camera [53].

For negative-stained TEM characterization, sample preparation begins with 400 Mesh Copper Grids coated with a carbon film. Since these grids are hydrophobic, they are treated using the ELMO Glow Discharge System. This treatment exposes the grids to a glow discharge at 30 mA for 30 seconds.

Subsequently, 4  $\mu\text{L}$  of the sample are applied to the carbon-coated side of the grid. The sample is allowed to sediment for 1 minute, then excess liquid is blotted off with filter paper. The grid is then washed with a drop of water for 30 seconds, blotted again, and stained with 5  $\mu\text{L}$  of 1% (v/v) uranyl acetate for 1 minute. Finally, the grid is blotted once more and allowed

to air-dry at room temperature for 2 minutes before being ready for TEM analysis. The images are recorded and acquired using a Talos L120C (120 kV) microscope equipped with a Ceta S 16M CMOS camera (4k × 4k).

### 3.3.5 Sedimentation Velocity Analytical Ultracentrifugation (SV-AUC)

Analytical Ultracentrifugation (AUC) is a technique used to study particles' sedimentation behaviour and provide insights into their size, molar mass, and density. Developed by Svedberg in the 1920s [39], AUC analyzes nanoparticles ranging from 1 nm to 5000 nm by separating them based on density and molecular weight. It operates through two main approaches: sedimentation velocity (SV) and sedimentation equilibrium (SE). In SV experiments, high-speed centrifugation forces particles to sediment, allowing for the determination of particle size and shape based on the sedimentation coefficient  $s$  and diffusion coefficient  $D$  [39]. This approach enables the analysis of particle motion under high centrifugal forces [39]. Conversely, SE experiments, conducted at lower speeds, establish an equilibrium between sedimentation and back-diffusion of particles in solution [54]. They are primarily used to determine molar mass, stoichiometry, and equilibrium constants in protein interactions [55][40].

The Beckman Coulter XL-I ultracentrifuge is utilized in these experiments (Figure 32).



**Figure 32** – Beckman Coulter XL-I.

For velocity runs, sector-shaped sample compartments are employed to minimize convection disturbances [56]. These compartments are essential as they allow the particles to move along radial paths, preventing interference from wall collisions [56]. Double-sector cells are used to measure absorbance differences between the sample and solvent sectors, helping to account for solvent redistribution and absorption effects under high centrifugal forces (Figure 33) [56].

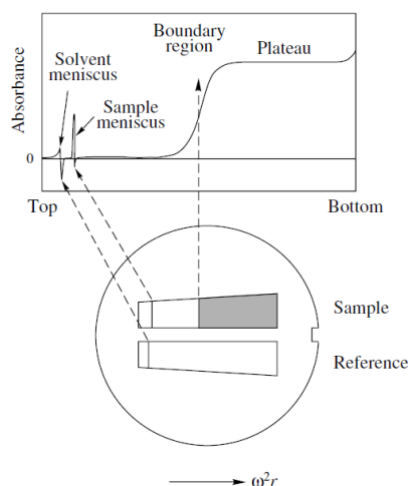


**Figure 33** – In a double-sector centerpiece, the sample moves towards the bottom of the sector-shaped container to minimize convection. The reference sector is typically filled just slightly more than the sample sector to ensure that the solvent meniscus does not overlap with the sample profile.

With the 8-hole Beckman rotors, up to seven samples can be analyzed simultaneously, with one position reserved for a radial calibration cell.

The absorbance detection system operates similarly to a double-beam spectrophotometer and follows the Beer-Lambert law [57]. It uses monochromatic light across a broad wavelength range, allowing the identification of different species with non-overlapping absorption spectra [56].

The system includes several key components: a Xenon flash lamp for light generation, a monochromator to select the desired wavelength, a sample cell to hold the sample, a slit assembly to track radial absorbance changes, and a photomultiplier tube (PMT) to convert light signals into digital data (Figure 34) [58].

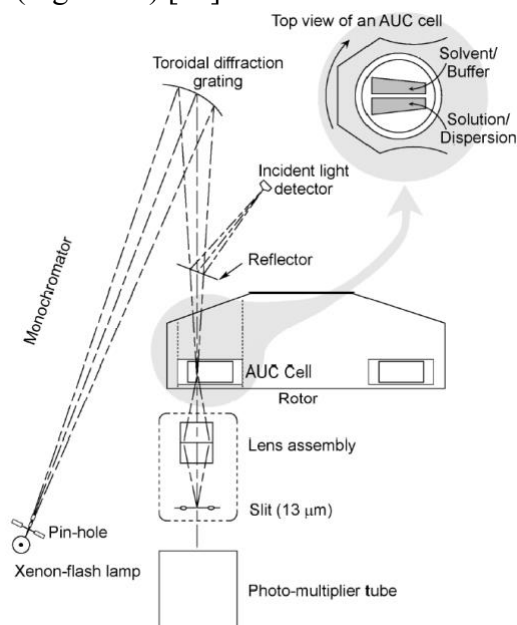


**Figure 34** – The light path in an absorbance optical system (Beckman Coulter Optima XL-A/XL-I AUC).

This setup ensures high precision, with a typical accuracy of  $\pm 0.01$  optical density (OD) [56]. The SV experiments are conducted using absorbance optics. For this reason, it is essential to keep the absorbance within the linear range of Beer's Law (0.2–1.0 OD).

The sample cells are assembled with standard double-sector centerpieces featuring quartz windows. The reference sector is filled with 430  $\mu\text{l}$  of buffer, while the sample sector holds 420  $\mu\text{l}$  of the sample solution.

Once the cells are assembled, they are loaded into the rotor along with a properly balanced counterweight. The rotor is then inserted into the centrifuge, the monochromator is positioned, and the vacuum system is activated (Figure 35).

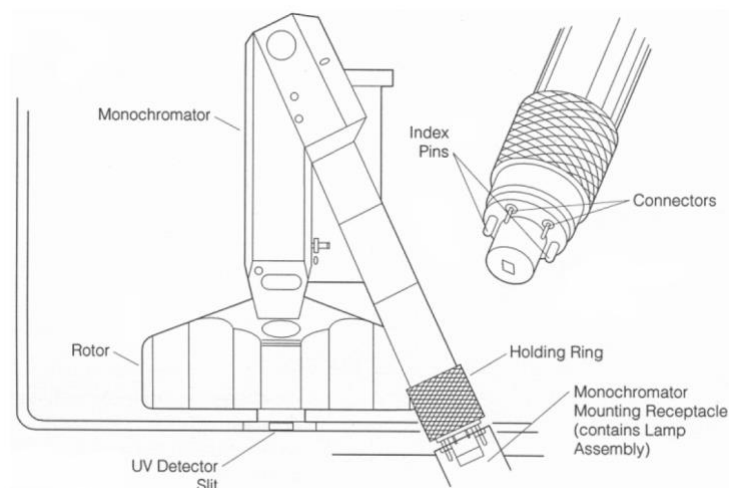


**Figure 35** – Mounting the monochromator [58].

Initially, the speed is set to zero while the rotor remains stationary, allowing the diffusion pump to activate and reduce the vacuum to below 100  $\mu\text{m}$ . This step ensures that the temperature measurement accurately reflects the rotor's temperature. Once the desired temperature is reached, the system is allowed to equilibrate for at least two hours before acceleration, minimizing convection effects caused by temperature gradients and stabilizing the samples.

Key operating parameters in SV experiments include temperature, rotor speed, scan timing, and the number of scans. To maximize the number of data sets for analysis, the scan delay and scan interval should be set to zero in the Beckman Coulter ProteomeLab software.

The resolution of solution components is proportional to  $\omega^2$ , meaning higher rotor speeds improve the differentiation of components. Additionally, to ensure consistent hydrodynamic measurements, sedimentation and diffusion coefficients are typically standardized to 20  $^{\circ}\text{C}$ .

All these parameters are controlled through the instrument's hard-key console, with real-time values displayed alongside preset conditions for continuous monitoring (Figure 36).



**Figure 36** – Console of Beckman Coulter XLI.



## 4. Results and Discussion

### 4.1 Evaluation of Low-Density Lipoprotein (LDL) Extraction Methods

#### 4.1.1 Analysis of Fast Protein Liquid Chromatography (FPLC)

To assess which protocol yields the purest LDL sample, the chromatograms obtained from FPLC are analyzed and compared. The evaluation focuses on differences in elution profiles, peak resolution, potential overlaps with other lipoproteins, and variations in intensity. This comparison provides insights into the efficiency and selectivity of each method in isolating LDL with minimal contamination.

From SEC analysis of the 1<sup>st</sup> protocol, 3 main peaks are collected, as shown in Figure 8. SEC analysis of the 2<sup>nd</sup> protocol, unlike the previous one, results in a single peak, which encompassed fractions 5, 6 and 7. This observation suggests that the lipoprotein population is more homogeneous, indicating a higher degree of uniformity in particle composition and size. This, in turn, implies that the separation process has been enhanced, leading to greater efficiency and resolution compared to the previously employed method (Figure 37).

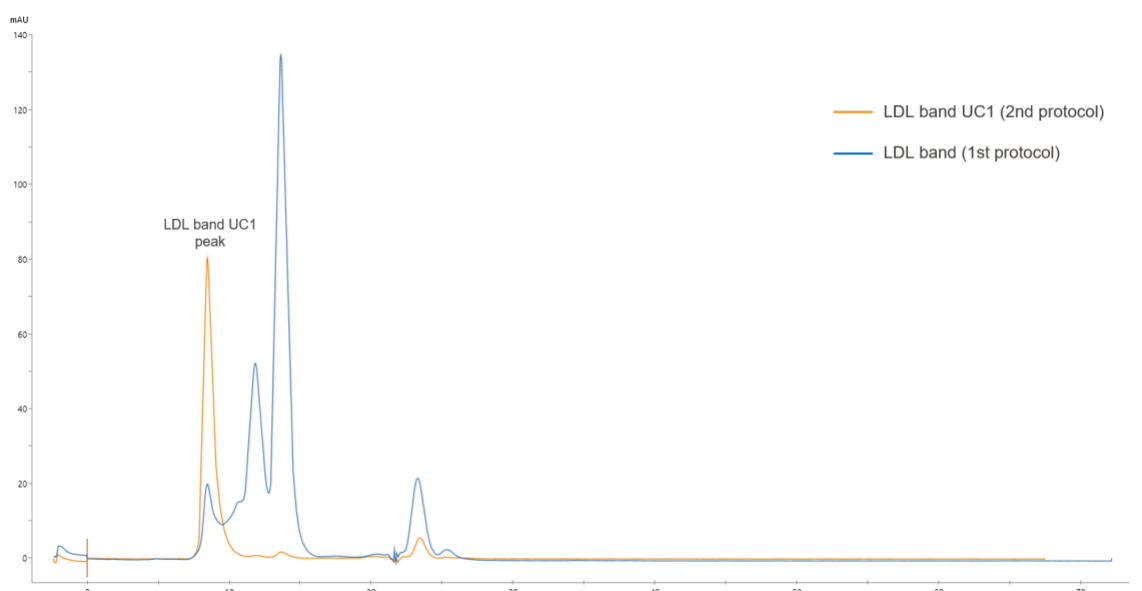


**Figure 37** – Chromatograms obtained from FPLC. In blue and orange are reported the LDL band collected from 1<sup>st</sup> protocol and the LDL band obtained from 2<sup>nd</sup> protocol after the first centrifuge, respectively.

Figure 12 presents the FPLC profile obtained using the 2<sup>nd</sup> protocol, comparing the results with one centrifuge versus two centrifuges. While the use of two centrifuges leads to a higher degree of purity in the final sample, the overall difference between the two curves is not particularly pronounced. The profiles appear relatively similar, suggesting that although additional centrifugation improves purity, its impact on the overall chromatographic pattern remains subtle.

The comparison between the chromatogram obtained from the FPLC of the LDL band collected after DGUC and the LDL band collected from DGUC after multiple filtrations using a 100 kDa MWCO filter is shown in Figure 38. The two curves appear to overlap completely, with the only difference being the sample concentration.

This confirms that the filtration process is effective in refining the sample while preserving the structural integrity and chromatographic behavior of LDL, ensuring consistency in subsequent analyses.



**Figure 38** – Comparison between chromatograms obtained from FPLC of the several times filtrated LDL band collected after DGUC and the LDL band after first centrifuge of 2<sup>nd</sup> protocol.

Figure 18 shows FPLC result of commercial LDL. The chromatogram reveals not only the expected main peak but also several additional peaks, although these are relatively minor in intensity. These smaller peaks suggest the presence of impurities or other components within the sample. To isolate the primary component of interest, the fractions corresponding to the first and most prominent peak have been carefully collected for further analysis. This step has been taken to ensure the purity and integrity of the LDL fraction, minimizing the influence of any potential contaminants that might affect downstream applications or results.

A comparison of chromatograms obtained from FPLC for two distinct LDL samples is illustrated in Figure 39: one collected after DGUC and the other a commercial LDL sample. The chromatograms reveal differences in peak position, indicating variations in the LDL obtained.

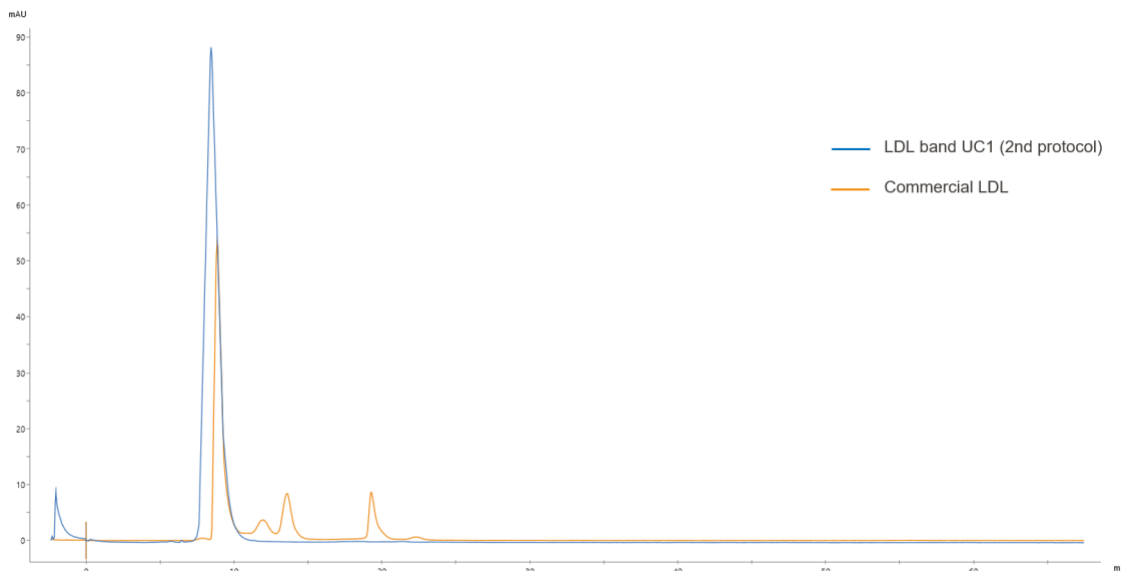


**Figure 39** – Comparison of the chromatograms obtained from FPLC for the LDL band collected after DGUC and the commercial LDL sample.

#### 4.1.2 Dynamic Light Scattering (DLS) Characterization

To identify which peak of the FPLC obtained from the 1<sup>st</sup> protocol corresponds to LDL particles, each of these is analyzed through DLS to determine the dimensions of the collected fractions. This evaluation shows that peak 1 corresponds to the LDL fraction, as shown in Figure 40. In fact, the peak is 20.365 nm with a standard deviation of 3.686 nm.

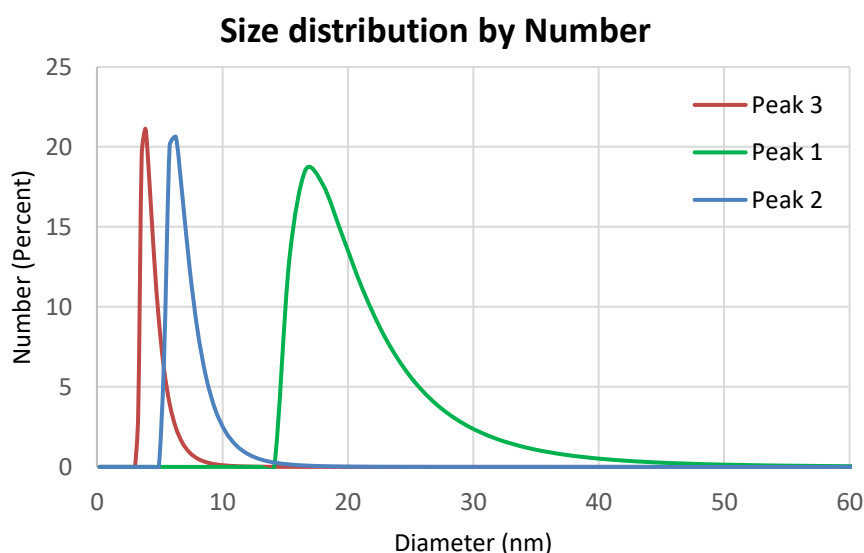


**Figure 40** – Number Distribution from DLS of the three peaks obtained from FPLC of 1<sup>st</sup> protocol.

Figure 41 presents a comparison of the Number Distribution from DLS for the 2nd protocol, which includes DGUC followed by FPLC, DGUC followed by multiple filtration steps and then FPLC, and DGUC followed by PEG precipitation and FPLC. The three distribution curves show a strong overlap, further confirming the results obtained from the FPLC chromatograms. The peak of DGUC + FPLC is at 21.487 nm with a standard deviation of 3.816 nm, the peak of DGUC + multiple filtrations + FPLC is at 21.692 nm with a standard

deviation of 3.947 nm, and the peak of DGUC + PEG + FPLC is at 20.873 nm with a standard deviation of 4.025 nm.

The LDL fractions obtained via DGUC + FPLC exhibit a slightly more pronounced peak, indicating a tendency toward a more uniform particle population. In contrast, the DGUC + PEG + FPLC method shows a broader distribution, suggesting a higher presence of polydisperse species, although the distinction is not highly pronounced.

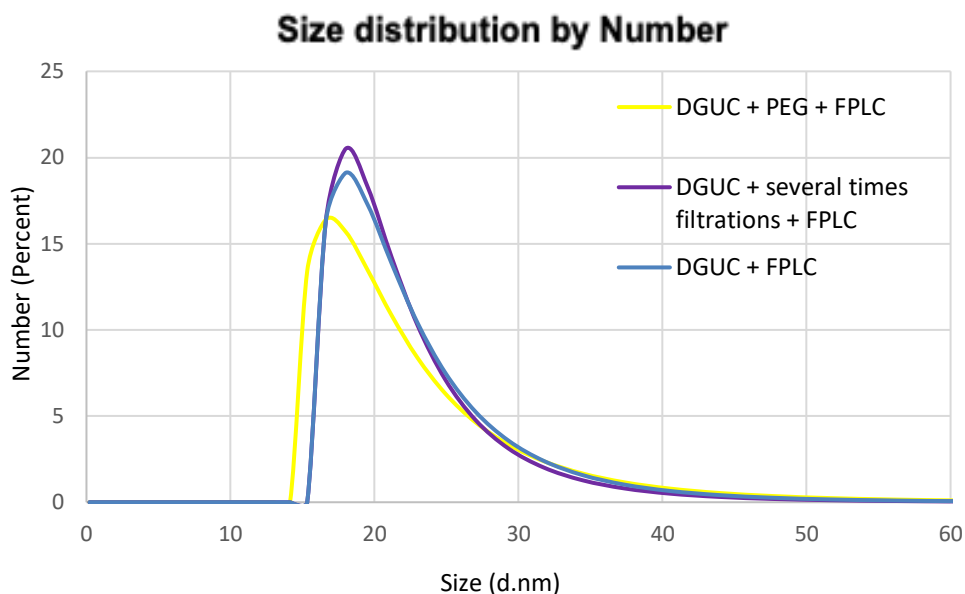


**Figure 41**– Number Distribution from DLS of 2<sup>nd</sup> protocol.

### 4.1.3 Transmission Electron Microscopy (TEM) Characterization

Negative-stained TEM is performed to visualize the morphological characteristics and size of the nanoparticles. The concentrations of the samples obtained from the 1<sup>st</sup> and 2<sup>nd</sup> protocols are approximately 0.5 mg/mL and 0.25 mg/mL, respectively, used to obtain the TEM images. As shown in Figure 42, the nanoparticles obtained using the 2<sup>nd</sup> protocol after just one round of centrifugation appear more uniform with a significantly lower contamination compared to those in Figure 43 (peak 1 of the first protocol). The sample exhibits a consistent size distribution, predominantly ranging from 20 to 30 nm in diameter.

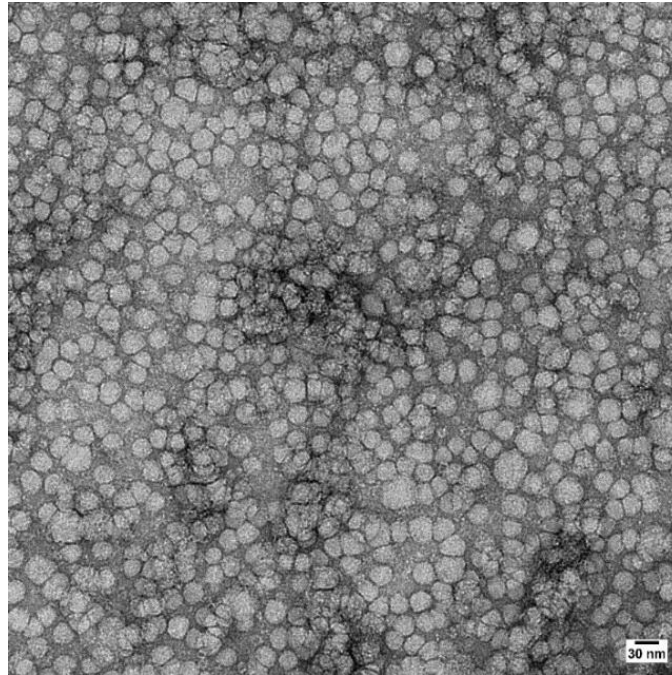


**Figure 42** – TEM peak 1 1<sup>st</sup> protocol.

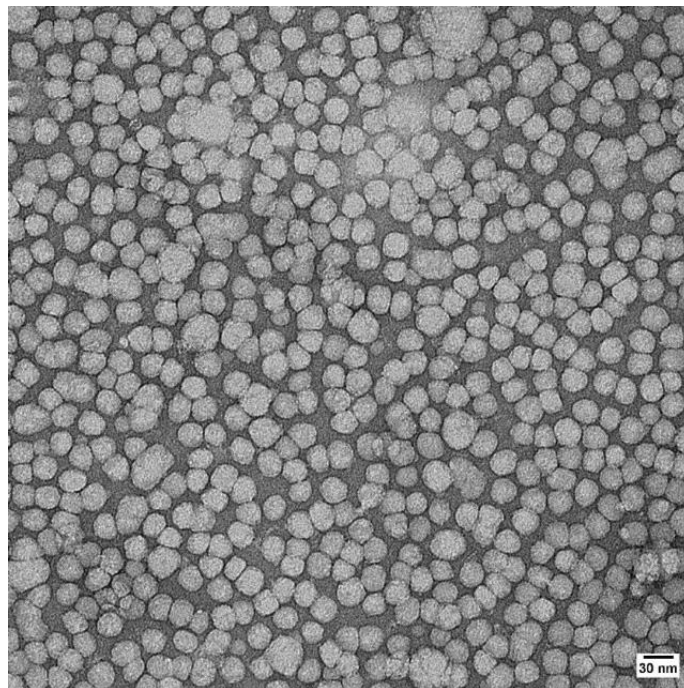


**Figure 43** –TEM peak of 2<sup>nd</sup> protocol.

#### **4.1.4 Sodium Dodecyl Sulphate- PolyAcrylamide Gel Electrophoresis (SDS-PAGE) characterization**

Sodium Dodecyl Sulphate-PolyAcrylamide Gel Electrophoresis (SDS-PAGE) analysis is performed to further validate the results (Figure 44). The purity of the samples is assessed using gel electrophoresis under both reducing and non-reducing conditions.

The gel images provide a clear visualization of the sample composition, confirming the hypothesis that peak 1 does not exhibit complete purity. This observation suggests the presence of additional protein species or contaminants that may not have been fully removed

during the purification process.

Specifically, in the 1<sup>st</sup> protocol, the protein corona does not appear to have been entirely stripped off, which could explain the presence of additional bands in the gel. This suggests that the applied conditions might not be sufficient to fully dissociate the adsorbed protein layer, potentially affecting the overall purity of the final sample.

Furthermore, evaluation of the 2<sup>nd</sup> protocol indicates that the additional centrifugation step in the second round does not significantly contribute to sample purification. The expected improvement in purity is not observed, and this result aligns with previous findings, further confirming that this step may not be effective under the current conditions. Among the tested protocols, the one involving a single centrifugation step yields the best results in terms of purity, suggesting that additional centrifugation may not be beneficial for sample quality. Further optimization or alternative approaches might be necessary to enhance the purification outcome.

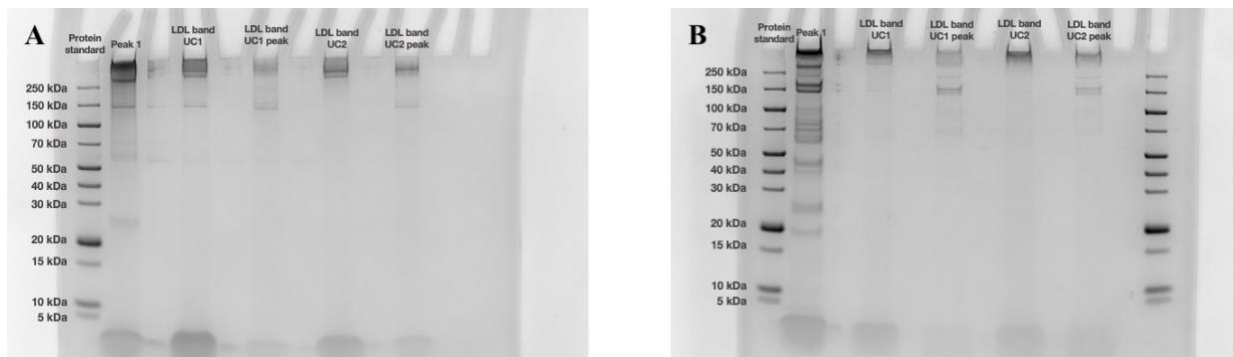


**Figure 44** – (A) SDS-PAGE without reducing agent. (B) SDS-PAGE with reducing agent.

SDS-PAGE analysis is also performed for the 2<sup>nd</sup> protocol, specifically for DGUC followed by FPLC and DGUC after several cycles with a 100 kDa MWCO filter followed by FPLC, DGUC followed by PEG precipitation. As shown in Figure 45, no significant changes are observed, confirming the consistency of this protocol and purification process. However, in the DGUC-FPLC sample, a specific band around 15 kDa is visible under non-reducing conditions, likely corresponding to a smaller fragment of Apo B.

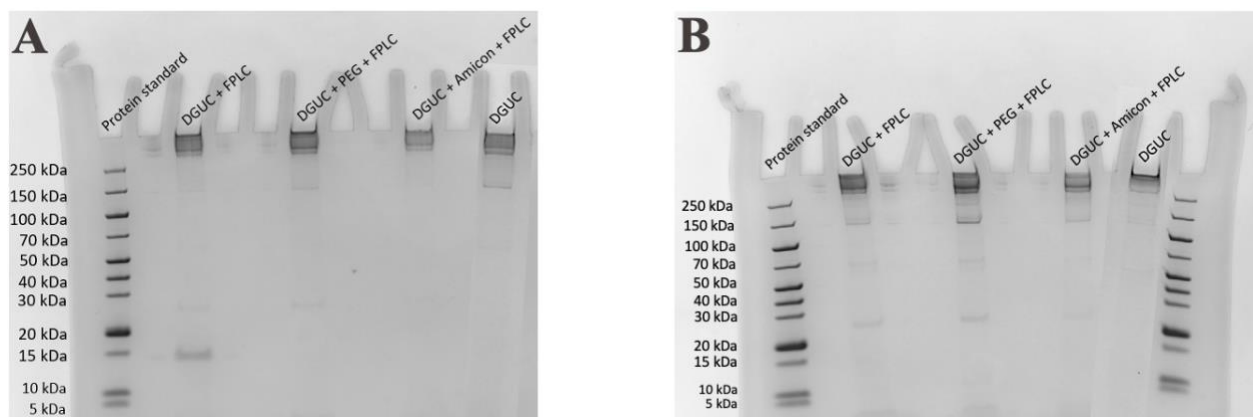


**Figure 45**– (A) SDS-PAGE without reducing agent. (B) SDS-PAGE with reducing agent.

### 4.1.5 Sedimentation Velocity Analytical Ultracentrifugation (SV-AUC) Characterization

The red curve in Figure 46 represents the sample obtained with the 2<sup>nd</sup> protocol, clearly highlighting the well-defined primary peak, while the secondary peaks are minimal. The blue curve, on the other hand, corresponding to the 1<sup>st</sup> protocol, shows a less defined profile with more prominent secondary peaks. This figure is obtained using normalization by max. The SV-AUC analysis confirms that the sample from the 2<sup>nd</sup> protocol is significantly purer, with the dominant primary peak corresponding to the purified form of the sample, while the weaker secondary peaks suggest a minimal presence of impurities. The lower intensity of these secondary peaks indicates that the 2<sup>nd</sup> protocol is more effective in removing contaminants, resulting in more homogeneous and uniform preparation.

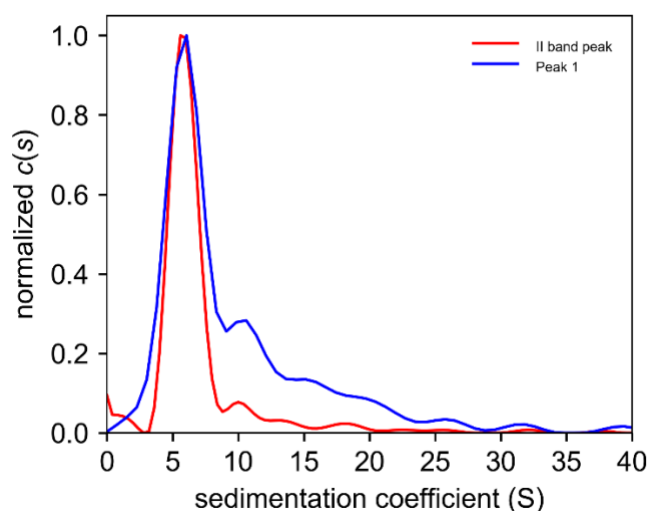


**Figure 46** – Sedimentation coefficient distributions normalized by max.

The SV-AUC of LDL-S, obtained according to the protocol in subsection 3.1.3, is performed, allowing for a comparison with unstained LDL. This comparison aims to determine whether the dye has affected the particles. This comparison is essential to determine if the dye integration impacted on the size, stability, or behavior of the LDL particles in solution, potentially influencing the results of subsequent experiments. As shown in Figure 47, the peak on the graph remains in the same position, showing no significant shift between the stained and unstained LDL. This indicates that the dye incorporation does not lead to any substantial changes in the overall size. The absence of a huge shift suggests that the structural integrity and characteristics of the LDL particles are maintained during the staining process. Additionally, the use of 540 nm wavelength in SV-AUC is advantageous because it is specifically optimized to detect LDL, minimizing interference from other proteins in the sample. This ensures a more specific result, as only the stained LDL is detected, preventing overlap with other proteins that could potentially influence the results.

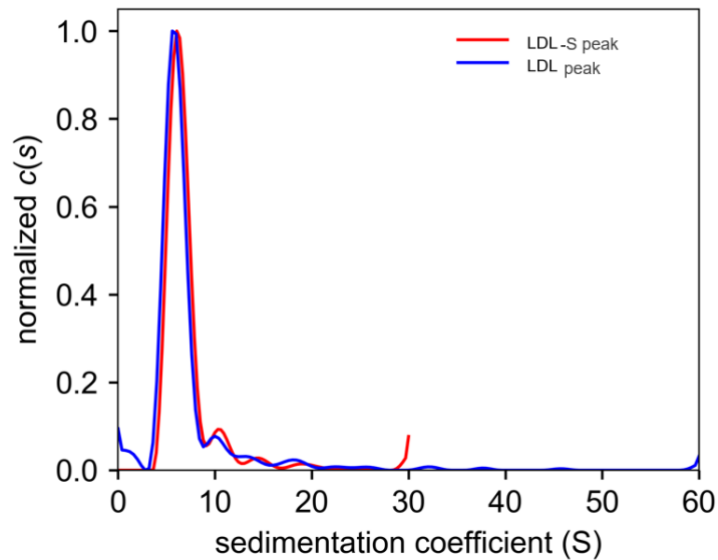


**Figure 47** – Sedimentation coefficient distributions normalized by max.

The SV-AUC analysis presented in provides insights into the sedimentation behavior of LDL fractions isolated via DGUC. The graph shows the normalized sedimentation coefficient distributions, enabling a comparative assessment of additional purification steps.

A main peak around  $\sim 7$  S suggests a similar predominant particle population across all methods, with overlapping curves indicating no substantial changes in average size. However, slight variations in peak width and position suggest differences in particle distribution and potential changes in sedimentation properties. Notably, the DGUC + PEG + FPLC peak is slightly shifted left compared to DGUC + FPLC, though the change is minimal.

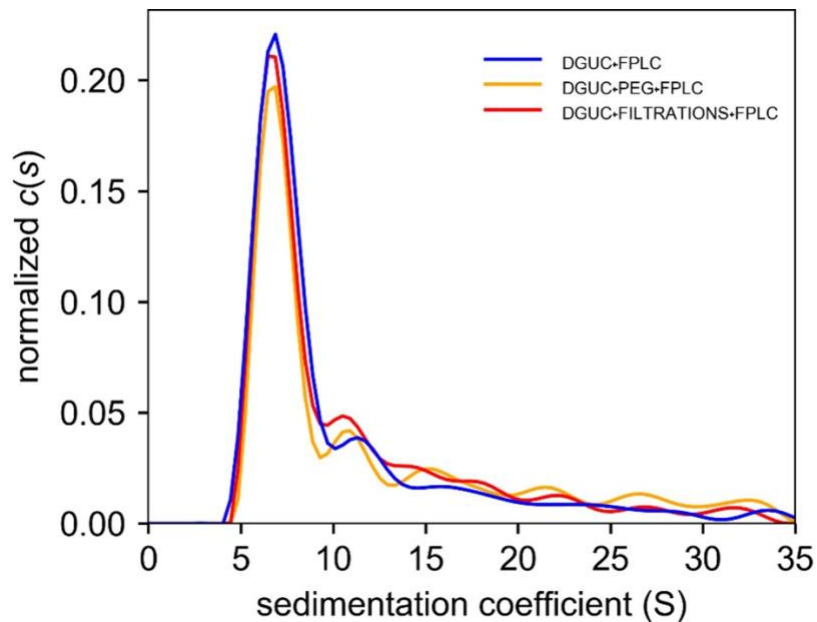


**Figure 48** – Sedimentation coefficient distributions normalized by area.

## 4.2 Interactions between LDL and Human Serum Albumin (HSA)

### 4.2.1 Interactions between unstained LDL particles and HSA

We examine the potential interactions between LDL extracted using the protocol described in subsection 3.1.2 and HSA, as it is the most abundant plasma protein. Given HSA's primary role in maintaining osmotic pressure and binding small hydrophobic molecules, significant interactions with LDL are not expected. Furthermore, LDL particles are primarily stabilized by their own protein and lipid components, making non-specific binding to albumin unlikely. However, if binding between albumin and LDL were to occur, it could influence several critical aspects of LDL metabolism, including its clearance from the bloodstream, stability, and susceptibility to oxidation.

This investigation is carried out to confirm this assumption before exploring interactions with other plasma components.

When LDL and HSA are combined, the resulting FPLC chromatogram clearly displays the characteristic LDL peak, with no detectable shift, which would indicate an interaction between the two molecules (**Figure 19** – Chromatogram obtained from FPLC of the LDL with HSA at different concentrations overnight at 4°C. Figure 19, Figure 20). The absence of changes in retention time suggests that, under the tested conditions, HSA does not significantly bind to LDL or alter its elution behavior. If strong binding were occurring, it would likely cause noticeable alterations in the chromatographic profile, such as peak broadening, shifts in retention time, or the emergence of new peaks corresponding to LDL-HSA complexes. This reinforces the hypothesis that their association is weak or negligible in this experimental setup.

To confirm the result obtained from FPLC, SV-AUC was performed. Figure 49 presents the normalized by max sedimentation coefficient distributions for LDL alone and in the presence of increasing HSA concentrations, under different incubation conditions. The distribution of LDL alone remains unchanged when HSA is added at concentrations of 60  $\mu\text{M}$  (4 mg/mL), 602  $\mu\text{M}$  (40.0 mg/mL or physiological concentration), and 1503  $\mu\text{M}$  (100 mg/mL), regardless of incubation time or temperature. The main LDL peak, around 7 S, is preserved across all conditions, with no apparent shift towards lower or higher sedimentation coefficients. If a strong interaction between LDL and HSA were occurring, an additional peak or a significant displacement of the LDL peak would be expected, corresponding to the formation of LDL-HSA complexes. It can be observed that when HSA concentration is significantly higher than the physiological one, there is a slight shift of the peak of the curve to the right, as seen in the cyan curve. The presence of free HSA is evident at lower sedimentation coefficients, as indicated by the characteristic peak at 4.5 S, yet this does not seem to influence LDL sedimentation behaviour. These findings reinforce the hypothesis that HSA does not significantly associate with LDL under the tested conditions.

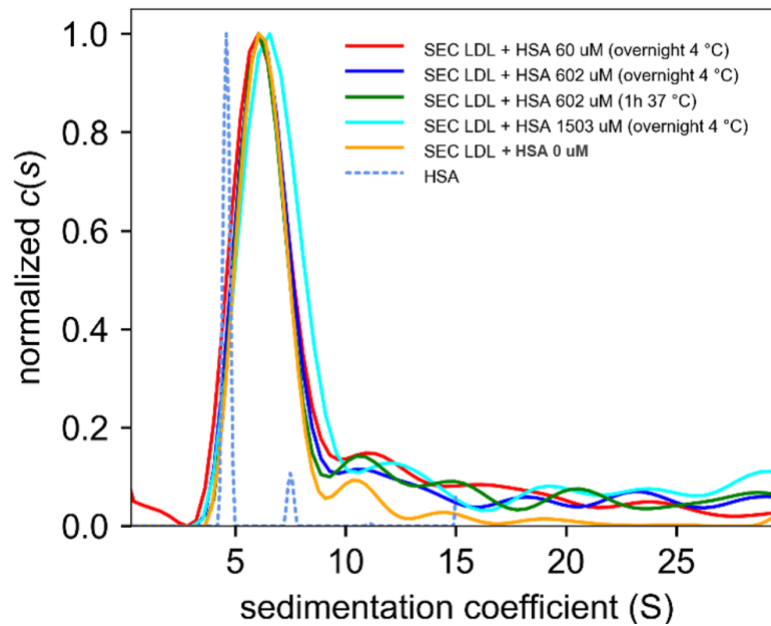


**Figure 49** – Sedimentation coefficient distributions normalized by max.

#### 4.2.2 Interactions between stained LDL particles and HSA

Based on the previous observation that there is a slight shift in the AUC curve peak at high HSA concentration, the behaviour of LDL-S particles, extracted using the protocol described in subsection 3.1.3, is analysed with high concentrations of HSA.

The absence of interaction between LDL and HSA is confirmed by the SV-AUC graph, as shown in Figure 50. The graph demonstrates that the curve for LDL-S aligns perfectly with the curve for LDL-S to which HSA is added at a concentration of 1503  $\mu\text{M}$ , strongly supporting the lack of significant interaction between the two.

The use of the dye offers several advantages in this analysis. It provides a clear and reliable method to track LDL particles throughout the experiment, enabling precise monitoring of their behavior during the process. This results in a more specific and focused assessment of LDL, improving the accuracy and interpretability of the data.

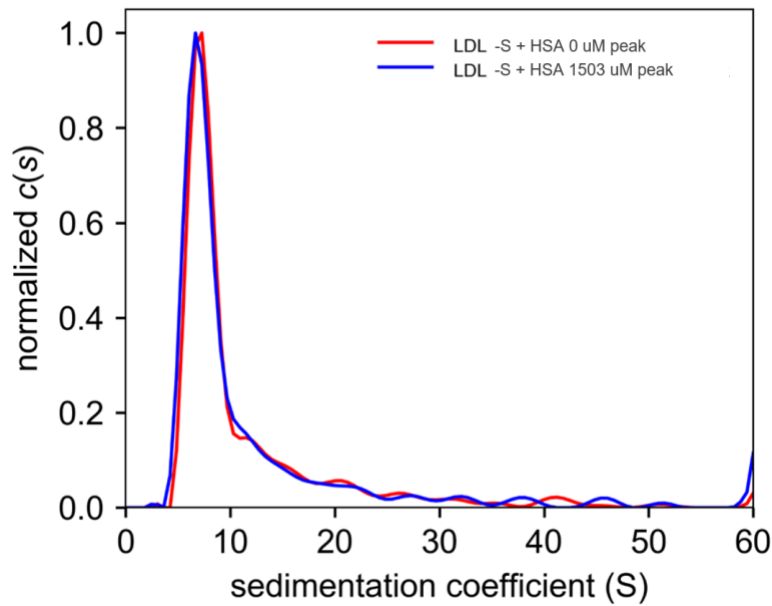


**Figure 50** – Sedimentation coefficient distributions normalized by max.

### 4.3 Interactions between LDL and Human Immunoglobulin G (IgG)

#### 4.3.1 Analysis of LDL-IgG Interaction – 1<sup>st</sup> Experiment

The fractions collected from the protocol described in 3.1.2 are incubated overnight with IgG at 4 °C and then subjected to a second FPLC for a purification step **Figure 47**.

The analysis of the results obtained through FPLC indicates that no significant variations can be detected in the LDL peak as the concentration of IgG increases, as shown in Figure 22. This suggests that FPLC lacks the sensitivity required to clearly and accurately reveal potential interactions between LDL and IgG. To overcome this limitation, SV-AUC analysis is performed on the fractions collected after purification step (Figure 51). The results reveal a noticeable shift in the peak position toward the right as IgG concentration increases. This shift serves as strong experimental evidence supporting a direct interaction between IgG and LDL. The observed change in sedimentation behavior is likely due to the formation of LDL-IgG complexes or aggregates, which could affect the overall distribution and signal intensity. As IgG concentration rises from 6.7  $\mu\text{M}$  ( $\sim 1$  mg/mL) to 80  $\mu\text{M}$  (12 mg/mL), these complexes appear to grow progressively larger, suggesting a dose-dependent association between LDL and IgG. This finding reinforces the hypothesis of a specific binding interaction.

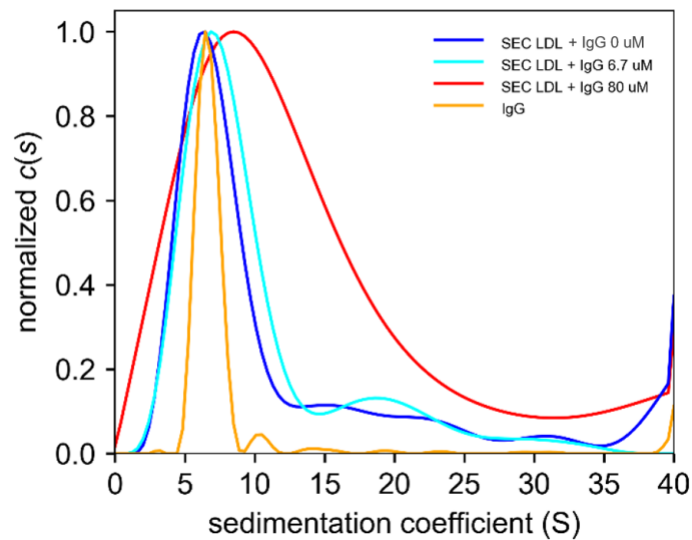


**Figure 51** – Sedimentation coefficient distributions normalized by max.

Figure 52 provides a representation of the results obtained. The LDL particles that interacted with IgG are collected following FPLC purification. In the SDS-PAGE analysis, the presence of both LDL and IgG can be clearly observed. The typical band for LDL appears at approximately 250 kDa, reflecting the size of the complex, primarily composed of the apolipoprotein B-100 and its associated lipid content. On the other hand, the IgG bands are observed at around 150 kDa, corresponding to the immunoglobulin structure, which consists of two heavy chains (each about 50 kDa) and two light chains (each about 25 kDa).

The presence of both bands in the same lane offers strong evidence for the interaction between LDL and IgG, confirming the formation of LDL-IgG complexes and supporting the findings from previous analyses.

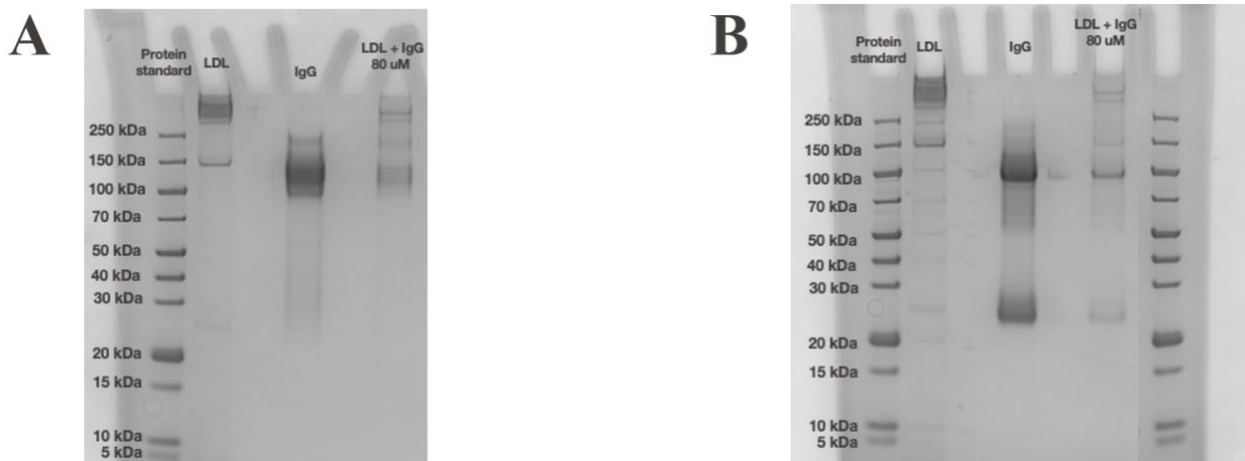


**Figure 52** – (A) SDS-PAGE without reducing agent. (B) SDS-PAGE with reducing agent.

### 4.3.2 Analysis of LDL-IgG Interaction – 2<sup>nd</sup> Experiment

Figure 53 shows the sedimentation coefficient distribution of LDL purified by FPLC after the protocol described in 3.2.3. The curves correspond to LDL samples overnight incubated at 4 °C with increasing concentrations of IgG, ranging from the control without antibodies to 80 μM, which approximates the physiological concentration.

In the untreated samples, the sedimentation profile exhibits a main peak around 7 S, consistent with monomeric LDL. However, upon IgG addition, this peak gradually decreases, and new species with higher S values appear. The observed effect is clearly dose-dependent: as the IgG concentration increases, there is a progressive decrease in the fraction of plain LDL. At the same time, new absorption peaks appear between 10 and 20 S, suggesting the formation of intermediate complexes.

There is a difference between this graph (Figure 53) and the previous one (Figure 51), and the hypothesis that has been made is that the starting sample has a different level of purity. This could imply that the variations observed in the current data, compared to the earlier ones, are not solely due to the experimental conditions or IgG concentration. Instead, the purity of the initial sample may play a crucial role in determining the results.

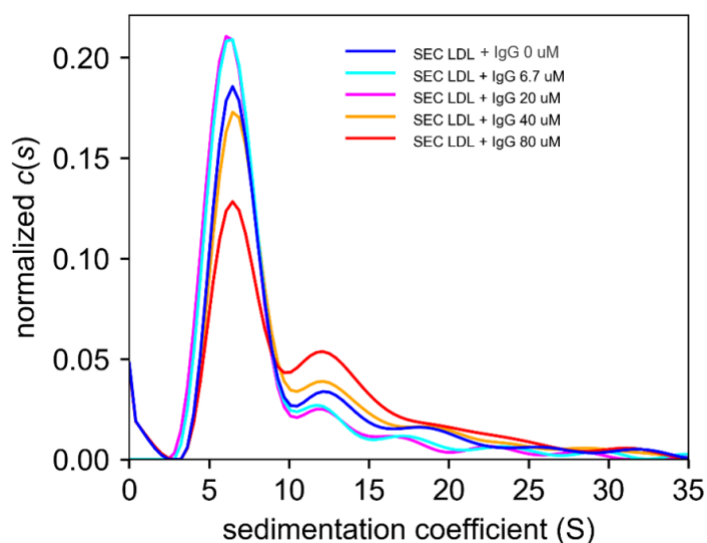


**Figure 53** – Sedimentation coefficient distributions normalized by area.

To further support this hypothesis, both DLS characterization and SV-AUC are performed. The DLS results shown in Figure 54 indicate that in the first experiment, the formation of larger particles occurred, suggesting the presence of possible aggregates. The peak corresponding to the first experiment is broader and shifted toward larger diameters compared to the second one. This suggests a higher degree of polydispersity, likely due to the presence of impurities in the LDL sample, which may have promoted intermolecular interactions or altered the physicochemical properties of the system.

Similarly, the SV-AUC analysis of the LDL samples from both experiments further supports this observation. As illustrated in Figure 55 the curve corresponding to 4.3.1, exhibits a broader profile and a more pronounced peak spreading compared to the other one. This indicates a greater heterogeneity in particle size distribution and suggests the presence of aggregates and LDL-IgG complexes in 4.3.1. Conversely, in 4.3.2, the sharper peak and reduced broadening suggest a more homogeneous LDL population, likely due to improved sample purity.

These findings highlight the crucial role of sample purity in determining LDL particles behaviour and reinforce the importance of optimizing experimental conditions to accurately assess LDL-IgG interactions and potential aggregate formation.

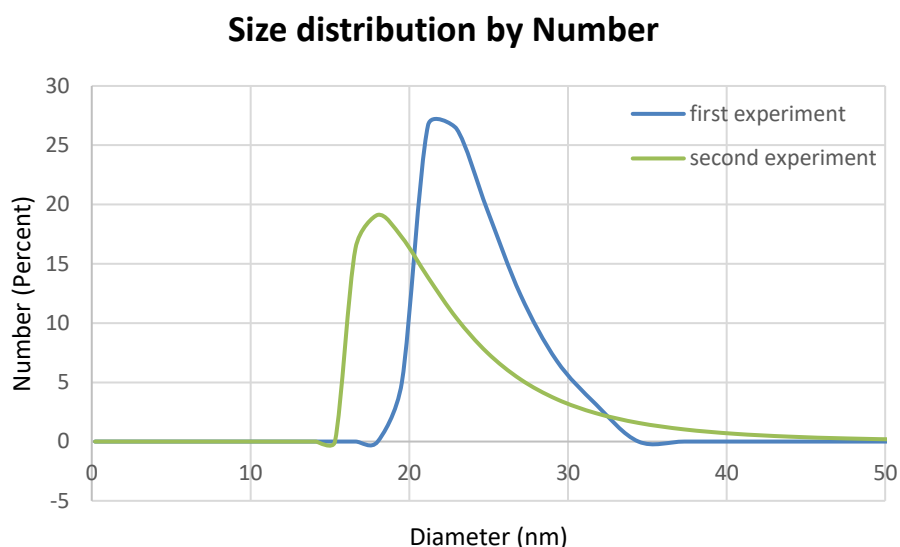


**Figure 54** – Number Distribution from DLS of the first and the second experiments.

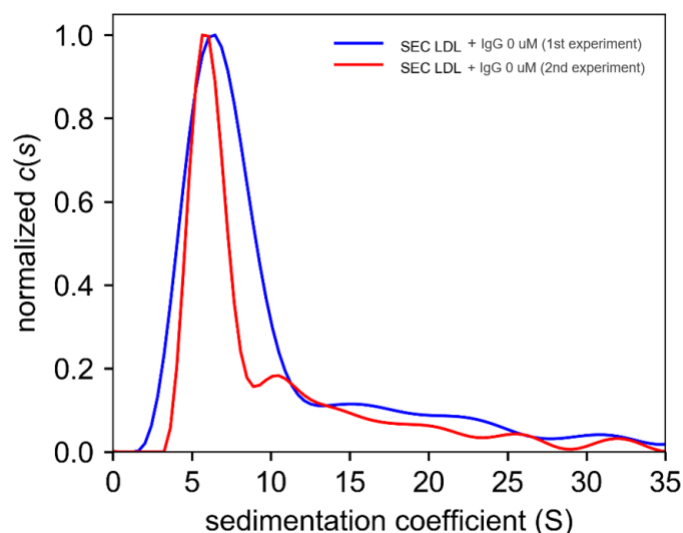


**Figure 55** – Sedimentation coefficient distributions normalized by max.

Furthermore, the sedimentation profiles of LDL in the presence of IgG are analysed under different incubation conditions using SV-AUC. Figure 56 presents the normalized sedimentation coefficient distributions for LDL incubated with IgG at 4 °C overnight, 37 °C for 1 hour, and 37 °C overnight, compared to a control sample of LDL. These conditions are chosen to evaluate the influence of both temperature and incubation time on LDL-IgG interactions, particularly regarding potential complex formation and particle stability.

The control sample exhibits a dominant peak around 7 S, corresponding to unbound LDL. When LDL is incubated with IgG at 4 °C overnight, the sedimentation profile remains largely unchanged, suggesting minimal interactions over time at low temperature. However, at 37 °C, both after 1 hour and overnight, a slight shift toward higher sedimentation coefficients occurs, along with peak broadening.

One possible explanation is that at physiological temperature, LDL undergoes structural rearrangements that increase the exposure of antigenic epitopes on ApoB-100, facilitating IgG binding [59]. Additionally, the increased lipid fluidity at 37 °C may alter LDL stability,

making the particles more prone to aggregation or complex formation [60].

Overall, these findings highlight the role of both temperature and incubation time in modulating LDL-IgG interactions.

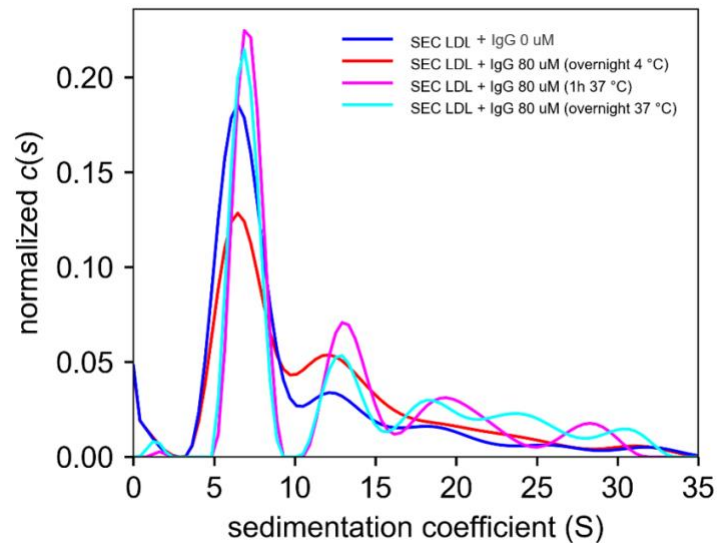


**Figure 56** – Sedimentation coefficient distributions normalized by area.

The interaction is also studied using SDS-PAGE under both non-reducing and reducing conditions.

In Figure 57A, the non-reducing conditions preserve potential protein complexes, as indicated by the presence of bands at higher molecular weights. Variations in band intensity reflect differences in protein concentration, while the presence of both LDL and IgG in the same lanes suggests possible interaction or co-migration.

In Figure 57B, the reducing conditions break disulfide bonds, leading to a shift toward lower molecular weights. Despite this, both LDL and IgG remain detectable, confirming their presence together in the samples. These results indicate that LDL and IgG coexist, supporting the idea of interaction, regardless of the electrophoretic conditions.

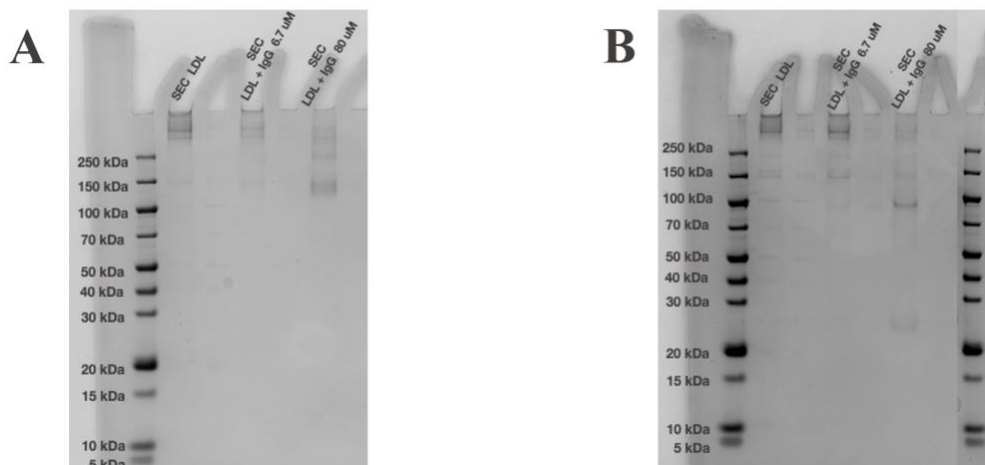


**Figure 57** – (A) SDS-PAGE without reducing agent. (B) SDS-PAGE with reducing agent.

### 4.3.3 Analysis of the Interaction of LDL Filtered Several Times with IgG

The SV-AUC analysis presented in Figure 58 offers detailed information on the sedimentation characteristics of nanoparticles derived from LDL after undergoing multiple filtration steps with a 100K-Amicon filter and incubated with IgG. This analysis allows for an in-depth evaluation of how the different purification processes affect the sedimentation behavior of the LDL fraction and its interaction with IgG.

The interpretation of this result is challenging because the peak of IgG is very close to the peak associated with LDL, making it difficult to directly associate the observed shift at a physiological concentration of 80  $\mu\text{M}$  with the interaction between these lipoproteins and IgG. This proximity between the peaks complicates the identification of a clear, specific interaction, as the shift could be attributed to factors unrelated to the LDL-IgG binding. Further studies might be necessary to isolate and characterize the specific interaction between LDL and IgG more accurately.

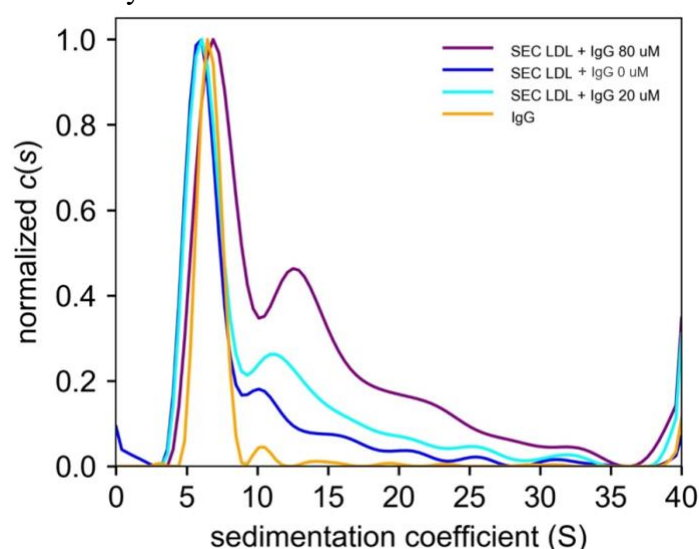
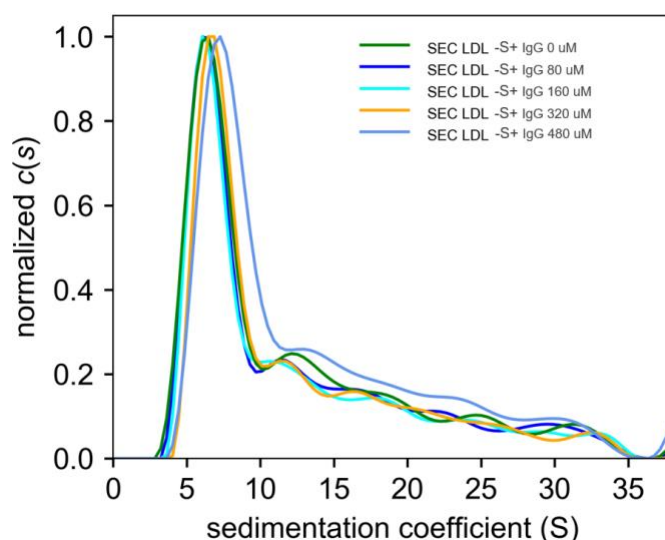


Figure 58 – Sedimentation coefficient distributions normalized by max.

### 4.3.4 Analysis of the Interaction of Stained LDL with IgG

SV-AUC is performed on stained samples as described in 3.2.4 , allowing the selection of a specific wavelength (540 nm) to detect only LDL, thus determining whether any interaction with IgG occurs. Interaction with IgG is also studied by significantly increasing the IgG concentration in the sample, well beyond the physiological concentration, thereby forcing the interaction with LDL.

The main peak of LDL shifts to higher sedimentation coefficient (SC) as IgG concentration increases (from 0 to 480  $\mu\text{M}$  or 72 mg/mL), likely due to the forced interaction between IgG and LDL, as shown in Figure 59. This increased interaction leads to an increased SC, as the binding of IgG to LDL induces changes in their hydrodynamic properties, resulting in a larger particle size or aggregation, which in turn affects the sedimentation behavior. A clear trend is observed in Figure 60 where SC is positively correlated to IgG concentration.



**Figure 59** – SC distributions normalized by max.

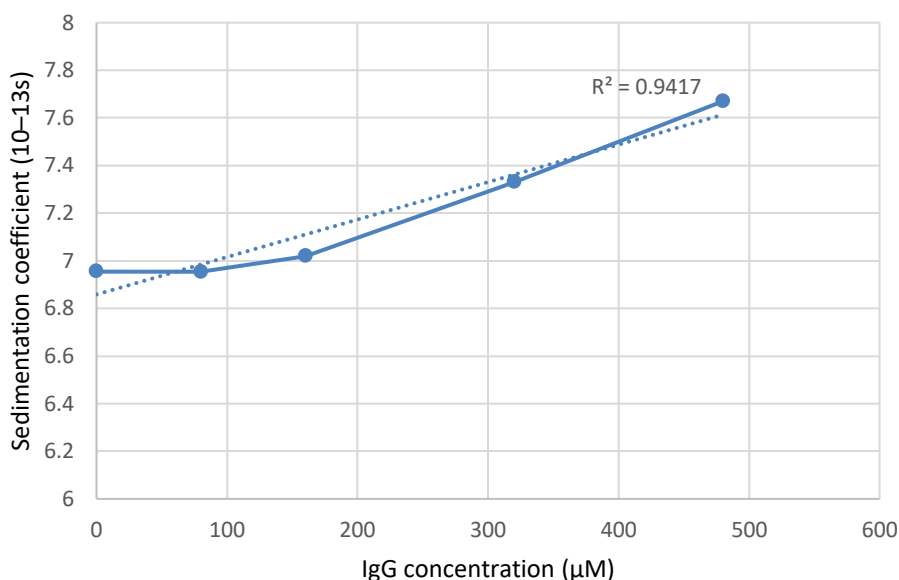


**Figure 60** - Representation of plot of average  $s$  versus IgG concentration for LDL-S.

#### 4.4 Interactions between LDL, HSA and IgG

The electrostatic interaction between HSA and IgG is being investigated based on their opposite charges. HSA has an isoelectric point (pI) of around 5.3 [61], while IgG has a pI of approximately 8.0 [62]. At physiological pH (7.4), HSA carries a net negative charge, while IgG is predominantly positively charged. This charge difference suggests the possibility of electrostatic interactions between the two proteins, which could, in theory, lead to the formation of complexes or transient binding in circulation.

To investigate this potential interaction, SV-AUC is being used for monitoring protein sedimentation and identifying potential complexes. It provides information on the formation of any aggregates or complexes by evaluating changes in sedimentation behavior of the two proteins when present together. Despite the theoretical expectations based on the opposite charges, the results obtained with SV-AUC do not confirm a significant interaction between IgG and HSA.

Starting from a stock solution of HSA and IgG with the same concentration ratio found in human plasma, the solution is diluted 2, 4 and 8 times (marked as HSA + IgG C0/2, HSA + IgG C0/4, HSA + IgG C0/8) to examine how the interactions between the two proteins vary at different concentrations. After preparing the samples, SV-AUC is performed to observe the behavior of the proteins in combination. The graph in Figure 61A, normalized by area and shows that the purple curve, representing the highest concentration, displays two distinct peaks corresponding to HSA and IgG, respectively. However, as the concentration decreases, the peaks become progressively less distinct. Further analysis is then conducted to explore the underlying causes of this observed behavior.

Additionally, Figure 61B shows HSA and IgG data obtained with SV-AUC, which are used as a control for interaction studies.

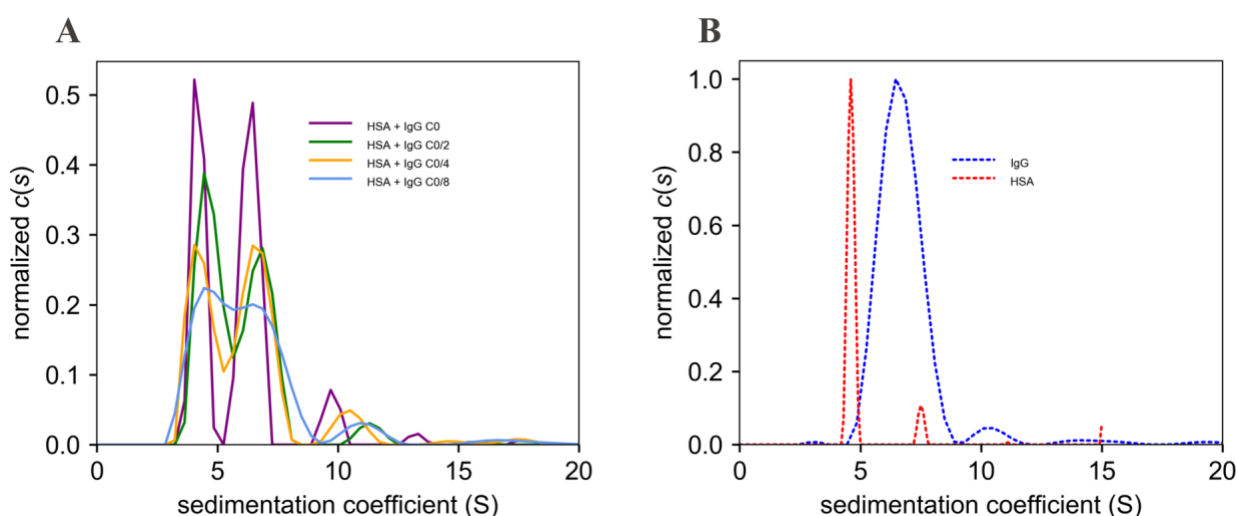
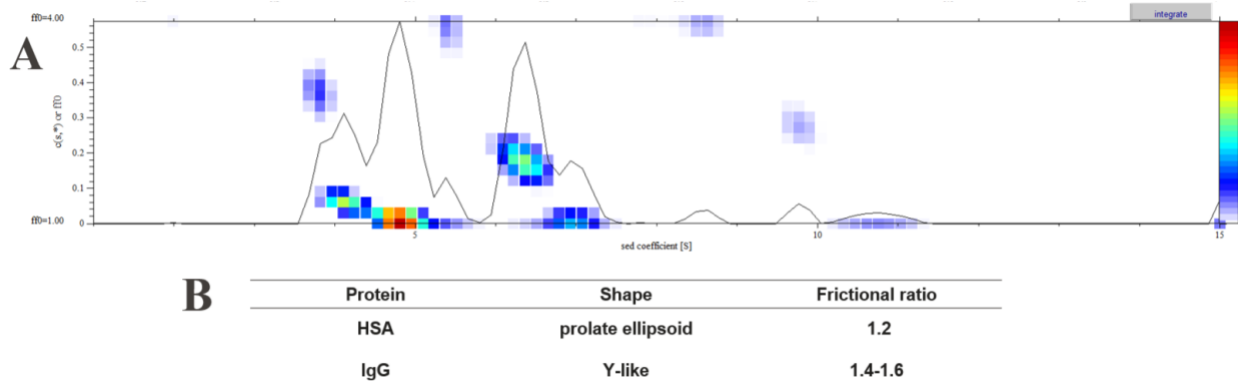


**Figure 61** – (A) Normalized SC distributions for different HSA + IgG concentrations. (B) Sedimentation behaviour of HSA and IgG.

SV-AUC is conducted to detect potential interactions between these two proteins while also assessing sample heterogeneity. If reversible interactions had occurred, additional peaks would likely have appeared between the main sedimentation peaks of HSA and IgG. The absence of such peaks suggests that either the interaction is too weak to be detected under these conditions or that a much higher concentration is needed to observe any binding effects, highlighting a limitation of AUC.

As described in 3.2.5, AUC analysis relies on the Lamm equation, which requires knowledge of both the sedimentation coefficient  $S$  and the diffusion coefficient  $D$ . The standard 1D approach involves fitting a range of  $S$  while assuming that all particles are spherical, using a fixed frictional ratio ( $\frac{f}{f_0} = 1$ ). However, this assumption does not account for the true asymmetry of molecules such as IgG, which is known to have a Y-shaped structure ( $\sim 12$  nm in length with three rod-like arms of  $\sim 3.5$  nm in diameter) [63]. To address this limitation, a 2D approach, shown in Figure 62A, is employed, allowing for a range of  $\frac{f}{f_0}$  values instead of a single assumed value. This approach provides a more accurate representation of the system's heterogeneity by considering different diffusion coefficients corresponding to each combination of  $S$  and  $\frac{f}{f_0}$ . The contribution of each solution to the Lamm equation fit is visualized using colour maps, offering a clearer depiction of the sample's complexity.

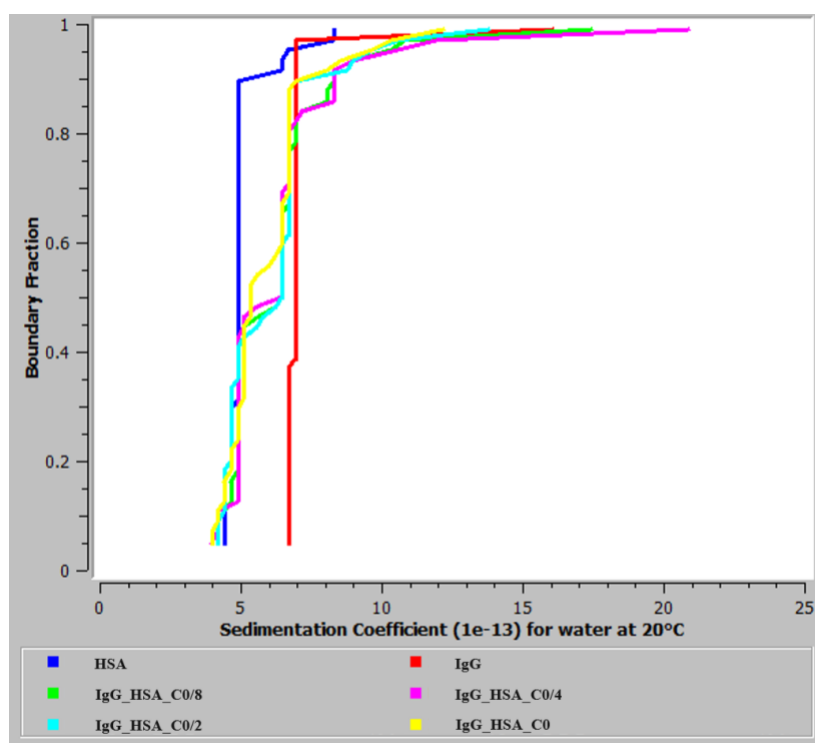
The results confirm that the two main peaks, corresponding to HSA and IgG, remain unchanged, indicating that the primary species in the sample do not undergo significant alterations or interactions under these conditions. Indeed, the absence of an additional peak beyond the two main species suggests that no significant interactions have occurred. Moreover, the structural differences between the proteins contribute to a degree of heterogeneity, further highlighting the lack of strong interactions between the examined proteins. The higher  $\frac{f}{f_0}$  values observed for IgG compared to HSA reflect its asymmetric shape, whereas HSA, being globular, maintains lower  $\frac{f}{f_0}$  values (Figure 62B).



**Figure 62** – (A) 2D SV-AUC analysis of the stock solution of HSA and IgG. (B) Table comparing the shape and the frictional ratio of HSA and IgG.

To further validate this result, additional analyses are performed. Figure 63 illustrates the cumulative fraction of molecules or particles that have sedimented up to a given SC. Steeper curves, such as the blue and red ones representing HSA and IgG, respectively, indicate a more homogeneous population with a narrow distribution of SCs.

When examining the sedimentation profiles of HSA and IgG at different concentrations, it is evident that the ratio of boundary contributions remains consistent across all conditions. Moreover, the relatively flat region between the peaks suggests that the two fractions remain separate and do not interact to form new species. This observation implies that no significant complex formation occurs between HSA and IgG under these experimental conditions.



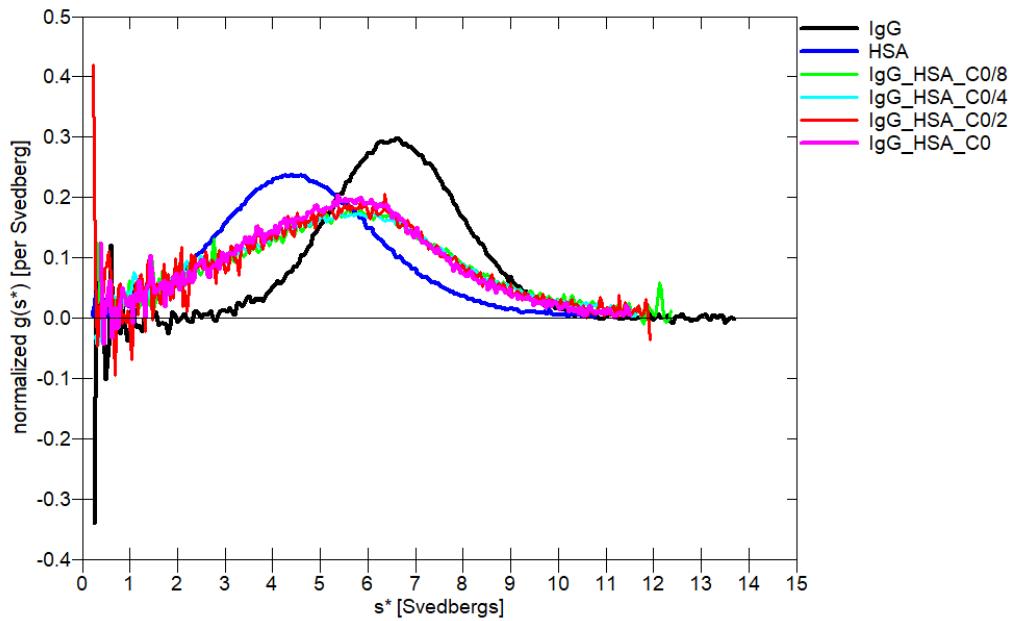
**Figure 63** – Boundary fraction analysis of SV-AUC data for IgG and BSA interaction.

Figure 64 represents the normalized distribution of HSA, IgG and their mixtures sedimenting at a given SC. Due to normalization, the area under each curve is equal to 1, allowing for a direct comparison of samples at different concentrations.

Looking at the individual curves, HSA and IgG exhibit broader distributions, with peaks around 4.5 S and 7 S, respectively.

The limited resolution of this technique prevents the detection of additional species present in low abundance, such as the HSA dimer, making only the dominant monomer peak visible. This low resolution is primarily due to the inherent averaging effect of the SV method, where species with similar SCs overlap, making it difficult to resolve closely spaced peaks.

Additionally, the consistent shape of the curves for HSA and IgG at different concentrations suggests that their interaction is weak and does not lead to the formation of new detectable species, despite potential electrostatic effects arising from charge differences.



**Figure 64** – Time derivative analysis of AUC data for IgG and BSA interaction.

Finally, SV-AUC is also performed to investigate the sedimentation behaviour of LDL in the presence of HSA at a constant physiological concentration and varying amounts of IgG, as shown in Figure 65.

The blue curve represents the sedimentation profile of purified LDL in the presence of HSA at its physiological concentration, serving as a control because, as demonstrated, the LDL peak remains unchanged under these conditions. Upon the addition of IgG at a low concentration, the primary peak remains at approximately the same position, but there is a noticeable increase in signal intensity at higher SCs (between 8–15 S). This indicates the formation of LDL-IgG or LDL-HSA-IgG complexes, leading to an increase in particle size and mass. However, the overall distribution suggests that a significant portion of LDL remains in its original, unbound state.

A more pronounced effect is observed when IgG concentration is increased to 80  $\mu\text{M}$ . Indeed, in this case, the peak associated to LDL particles shifts to the right, and a strong, broad distribution appears between 8–20 S. This suggests a substantial degree of association, leading to the formation of larger macromolecular complexes.

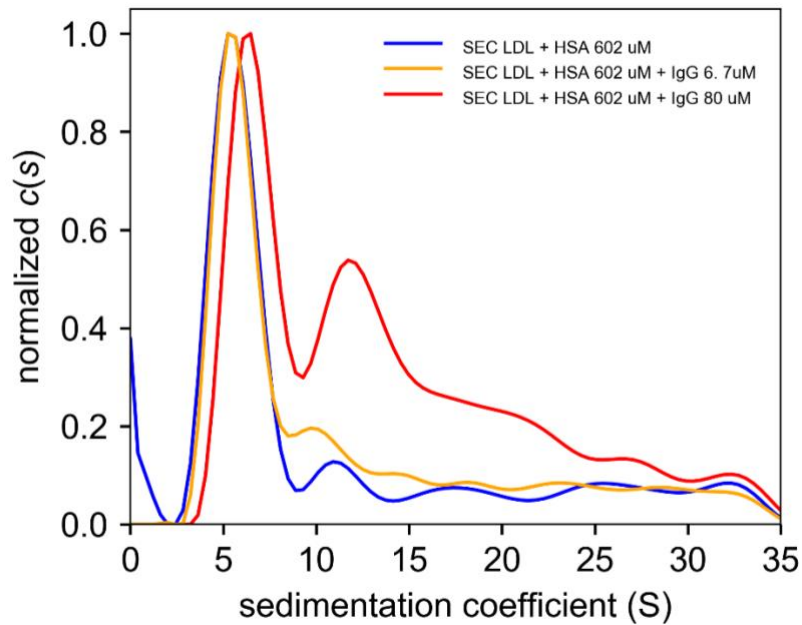


**Figure 65** – SC distributions normalized by max.

The SDS-PAGE analysis confirmed the co-presence of IgG, LDL, and HSA in the sample without providing additional information (Figure 66). A band corresponding to HSA is visible around 66 kDa, confirming its presence, also the bands related to IgG, around 150 kDa for the intact form or 50 kDa for two heavy chains and 25 kDa for two light chains are detectable. The band associated with LDL, though less defined, are also observable.

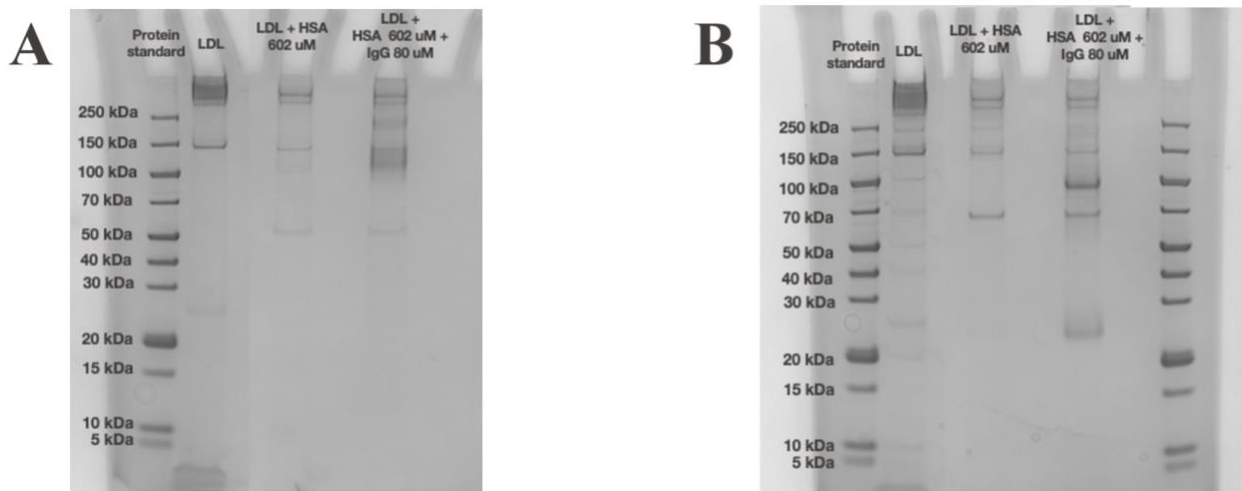


**Figure 66** – (A) SDS-PAGE without reducing agent. (B) SDS-PAGE with reducing agent.

## 4.5 Interactions between LDL and Human Apo-Transferrin Protein

### 4.5.1 Analysis of the Interaction of LDL and Apo-Transferrin Protein

Figure 67 represents the interaction between LDL and Apo-Transferrin as analyzed by SV-AUC. A single concentration of 3 mg/mL (37.7  $\mu$ M) is tested, with incubation overnight at 4°C. Notably, these LDL particles are obtained using the 2nd protocol and subsequently incubated with Apo-Transferrin, as described in 3.1.2.

Despite these controlled conditions, no detectable shift in the sedimentation peak is observed, suggesting that under these experimental settings, there is no significant interaction between LDL and Apo-Transferrin. This lack of observable changes in sedimentation behavior indicates that either the binding affinity between these molecules is low, or that any potential interaction does not significantly alter the hydrodynamic properties of LDL in a way that can be detected by SV-AUC.

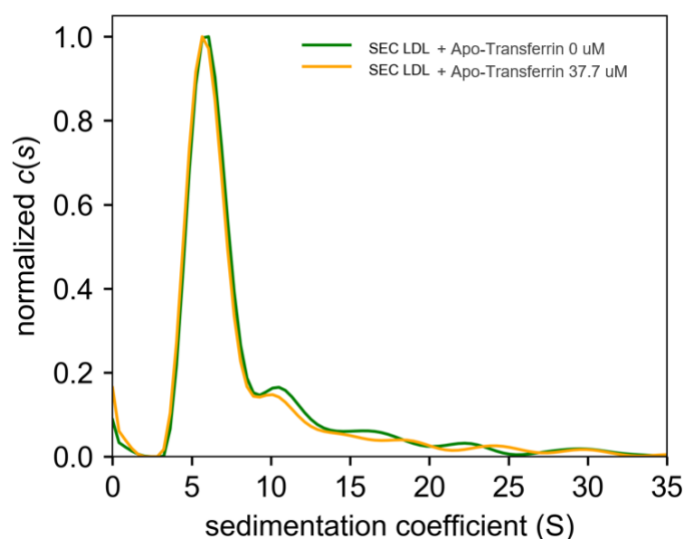


Figure 67 – SC distributions normalized by max.

### 4.5.2 Analysis of the Interaction of LDL Filtered Several Times and Apo-Transferrin Protein

The same experiment is conducted using an alternative LDL preparation protocol to assess whether the interaction with Apo-Transferrin could be influenced by differences in particle processing. Also in this case, it is tested the concentration of 3 mg/mL (37.7  $\mu$ M), with an overnight incubation at 4°C. In this case, LDL particles are obtained through multiple filtration steps, ensuring a high degree of purity and consistency before incubation with Apo-Transferrin, as described in 213.1.5. Despite the variation in the LDL preparation protocol compared to previous methods, no evident shift in the sedimentation peak is observed (Figure 68). This indicates that under these conditions, the interaction between LDL and Apo-Transferrin is either weak, transient, or insufficient to produce measurable changes in sedimentation behavior. The lack of significant alterations in the SC further reinforces the idea that, even after prolonged incubation and at the tested concentration, Apo-Transferrin does not strongly associate with LDL in a manner that affects its hydrodynamic properties or

promotes detectable aggregation.

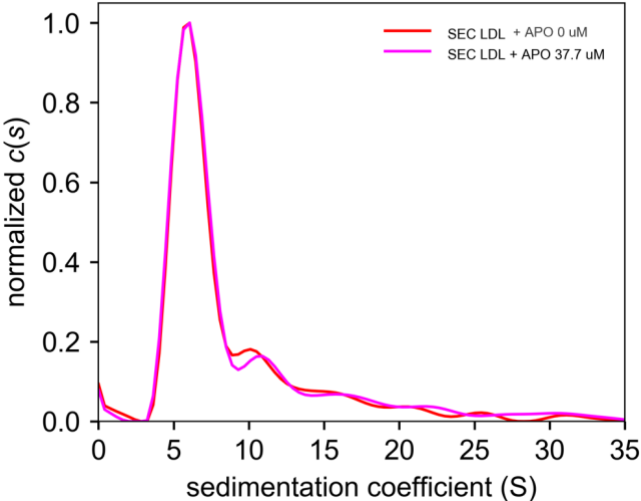


Figure 68 – SC distributions normalized by max.

## 5. Conclusions and Future Work

To accurately study LDL, it is essential to obtain highly pure preparations, free from unwanted protein contaminants. To this end, LDL is first isolated by DGUC and subsequently purified using various methods, including FPLC chromatography, multiple filtration steps, and PEG precipitation. Notably, the study confirms that PEG precipitation does not significantly alter LDL behavior under the tested conditions, thereby reinforcing the robustness and reliability of these precipitation strategies in preserving LDL integrity.

The results demonstrate that LDL readily engages with serum proteins, leading to the formation of both a hard and a soft corona. These interactions exhibit a high degree of protein specificity, with different serum proteins binding to LDL with varying affinities. IgG, in particular, displays a markedly strong affinity for LDL at concentrations as high as 480  $\mu\text{M}$ , facilitating the formation of larger, more complex macromolecular assemblies. In contrast, HSA, despite its higher concentration of 1503  $\mu\text{M}$ , does not exhibit significant binding to LDL. These observations suggest that both the abundance of a protein and its intrinsic binding affinity are critical determinants of the composition and structural characteristics of the LDL protein corona.

Building upon these results, future investigations should delve into the interaction between Apo-Transferrin and LDL. At physiological concentrations, Apo-Transferrin does not show significant binding to LDL, implying that its interaction dynamics may only become relevant at elevated concentrations. Further research at these higher levels could yield important insights into the potential structural effects of Apo-Transferrin on the protein corona. Additionally, exploring the impact of other serum proteins on LDL corona formation will further elucidate the complex network of interactions between lipoproteins and a diverse array of biomolecules. Expanding these studies to encompass a broader spectrum of proteins and experimental conditions will be essential for uncovering the mechanisms underlying protein corona formation and its subsequent influence on LDL function. These insights hold considerable promise for the development of targeted therapeutic strategies that exploit lipoprotein-protein interactions, thereby advancing the field of precision medicine.



## 6. List of Figures

<b>Figure 1</b> – Schematic representation of protein corona formation [4].	4
<b>Figure 2</b> – Lipoprotein structural composition [23].	4
<b>Figure 3</b> – Schematic overview of the size and density of various lipoproteins, including high-density lipoproteins (HDL), low-density lipoproteins (LDL), intermediate-density lipoproteins (IDL), very low-density lipoproteins (VLDL), and chylomicrons [made with VISME].	6
<b>Figure 4</b> – Charts representing human serum composition. (A) The 6 most abundant proteins represent approximately 85% of the total protein mass in human serum. (B) The 13 most abundant proteins are said to represent approximately 94% of the total protein mass in human serum. Apolipoprotein AI, AII and transthyretin are non-glycosylated proteins [32].	7
<b>Figure 5</b> – Forces acting on a solute particle in a gravitational field [11].	8
<b>Figure 6</b> – Schematic representation of the 1 <sup>st</sup> protocol for LDL extraction.	15
<b>Figure 7</b> – Schematic representation of the steps after DGUC.	16
<b>Figure 8</b> – Chromatograms obtained from FPLC. In blue and orange are reported the diluted and the concentrated LDL band with a 10 kDa MWCO filter, respectively.	16
<b>Figure 9</b> – Schematic representation of the 2 <sup>nd</sup> protocol for LDL extraction.	17
<b>Figure 10</b> – Photographs of the gradient in the centrifuge tube following lipoproteins separation. (A) In band III, LDL is clearly visible as a distinct orange-yellow band [15]. (B) Consistently with findings from [15], the formation of band III, corresponding to LDL, is also observed in this experiment.	17
<b>Figure 11</b> – Schematic representation of the 2 <sup>nd</sup> run of centrifuge.	18
<b>Figure 12</b> – Chromatograms obtained from FPLC. In blue and orange are reported the LDL band collected from 2 <sup>nd</sup> protocol after the first and second centrifuge, respectively.	18
<b>Figure 13</b> – Photographs of the gradient in the centrifuge tube (A) before and (B) after centrifuge.	19
<b>Figure 14</b> – Schematic representation of the procedure outlined above.	20
<b>Figure 15</b> – Chromatogram obtained through FPLC according to the outlined protocol.	20
<b>Figure 16</b> – Schematic representation of the procedure outlined above.	21
<b>Figure 17</b> – Chromatogram obtained from FPLC of the several times filtrated LDL band collected after DGUC.	21
<b>Figure 18</b> – Chromatogram obtained from FPLC of the commercial LDL sample.	22
<b>Figure 19</b> – Chromatogram obtained from FPLC of the LDL with HSA at different concentrations overnight at 4°C.	23
<b>Figure 20</b> – Chromatogram obtained from FPLC of the LDL with HSA at 602 μM, 1h at 37°C.	23
<b>Figure 21</b> – Chromatograms obtained from FPLC of LDL stained and HSA 1503 μM, overnight 4 °C.	24
<b>Figure 22</b> – (A) Chromatogram obtained from FPLC of IgG at different concentration. (B) Chromatogram obtained from FPLC of mixing LDL and IgG at different concentrations, overnight 4°C.	25
<b>Figure 23</b> – Chromatogram obtained from FPLC of mixing LDL and IgG at different concentrations, overnight 4°C.	26

<b>Figure 24</b> – Chromatogram obtained from FPLC of mixing LDL and IgG 80, overnight 4°C, overnight 37°C, 1h 37°C. ....	26
<b>Figure 25</b> – Chromatogram obtained from FPLC of mixing LDL and IgG at different concentrations, overnight 4°C. ....	27
<b>Figure 26</b> – Chromatogram obtained from FPLC of mixing stained LDL and IgG at different concentrations, overnight 4°C. ....	28
<b>Figure 27</b> – (A) Chromatogram of mixture of HSA 602 $\mu\text{M}$ and IgG 6.7 $\mu\text{M}$ . (B) Chromatogram of mixture of HSA 602 $\mu\text{M}$ and IgG 80 $\mu\text{M}$ . (C) Chromatogram obtained from FPLC of mixing LDL, HSA 602 $\mu\text{M}$ and IgG at different concentrations, overnight 4°C. ....	30
<b>Figure 28</b> – Chromatogram obtained from FPLC of mixing LDL and Apo-Transferrin 37.7 $\mu\text{M}$ , overnight 4°C. ....	31
<b>Figure 29</b> – Chromatogram obtained from FPLC of mixing LDL filtered several times and Apo-Transferrin 37.7 $\mu\text{M}$ , overnight 4°C. ....	31
<b>Figure 30</b> – ÄKTA go™ protein purification system from Cytiva. ....	32
<b>Figure 31</b> – Anton Paar Litesizer 500 Particle Analyzer. ....	34
<b>Figure 32</b> – Beckman Coulter XL-I. ....	35
<b>Figure 33</b> – In a double-sector centerpiece, the sample moves towards the bottom of the sector-shaped container to minimize convection. The reference sector is typically filled just slightly more than the sample sector to ensure that the solvent meniscus does not overlap with the sample profile. ....	36
<b>Figure 34</b> – The light path in an absorbance optical system (Beckman Coulter Optima XL-A/XL-I AUC). ....	36
<b>Figure 35</b> – Mounting the monochromator [58]. ....	37
<b>Figure 36</b> – Console of Beckman Coulter XLI. ....	37
<b>Figure 37</b> – Chromatograms obtained from FPLC. In blue and orange are reported the LDL band collected from 1 <sup>st</sup> protocol and the LDL band obtained from 2 <sup>nd</sup> protocol after the first centrifuge, respectively. ....	39
<b>Figure 38</b> – Comparison between chromatograms obtained from FPLC of the several times filtrated LDL band collected after DGUC and the LDL band after first centrifuge of 2 <sup>nd</sup> protocol. ....	40
<b>Figure 39</b> – Comparison of the chromatograms obtained from FPLC for the LDL band collected after DGUC and the commercial LDL sample. ....	41
<b>Figure 40</b> – Number Distribution from DLS of the three peaks obtained from FPLC of 1 <sup>st</sup> protocol. ....	41
<b>Figure 41</b> – Number Distribution from DLS of 2 <sup>nd</sup> protocol. ....	42
<b>Figure 42</b> – TEM peak 1 1 <sup>st</sup> protocol. ....	43
<b>Figure 43</b> –TEM peak of 2 <sup>nd</sup> protocol. ....	43
<b>Figure 44</b> – (A) SDS-PAGE without reducing agent. (B) SDS-PAGE with reducing agent. ....	44
<b>Figure 45</b> – (A) SDS-PAGE without reducing agent. (B) SDS-PAGE with reducing agent. ....	44
<b>Figure 46</b> – Sedimentation coefficient distributions normalized by max. ....	45
<b>Figure 47</b> – Sedimentation coefficient distributions normalized by max. ....	46
<b>Figure 48</b> – Sedimentation coefficient distributions normalized by area. ....	46
<b>Figure 49</b> – Sedimentation coefficient distributions normalized by max. ....	48
<b>Figure 50</b> – Sedimentation coefficient distributions normalized by max. ....	49
<b>Figure 51</b> – Sedimentation coefficient distributions normalized by max. ....	50

<b>Figure 52</b> – (A) SDS-PAGE without reducing agent. (B) SDS-PAGE with reducing agent.....	50
<b>Figure 53</b> – Sedimentation coefficient distributions normalized by area.....	51
<b>Figure 54</b> – Number Distribution from DLS of the first and the second experiments.....	52
<b>Figure 55</b> – Sedimentation coefficient distributions normalized by max. ....	52
<b>Figure 56</b> – Sedimentation coefficient distributions normalized by area.....	53
<b>Figure 57</b> – (A) SDS-PAGE without reducing agent. (B) SDS-PAGE with reducing agent.....	53
<b>Figure 58</b> – Sedimentation coefficient distributions normalized by max. ....	54
<b>Figure 59</b> – SC distributions normalized by max.....	55
<b>Figure 60</b> - Representation of plot of average $s$ versus IgG concentration for LDL-S. ....	55
<b>Figure 61</b> – (A) Normalized SC distributions for different HSA + IgG concentrations. (B) Sedimentation behaviour of HSA and IgG. ....	56
<b>Figure 62</b> – (A) 2D SV-AUC analysis of the stock solution of HSA and IgG. (B) Table comparing the shape and the frictional ratio of HSA and IgG.....	57
<b>Figure 63</b> – Boundary fraction analysis of SV-AUC data for IgG and BSA interaction. ....	58
<b>Figure 64</b> – Time derivative analysis of AUC data for IgG and BSA interaction. ....	59
<b>Figure 65</b> – SC distributions normalized by max.....	60
<b>Figure 66</b> – (A) SDS-PAGE without reducing agent. (B) SDS-PAGE with reducing agent.....	60
<b>Figure 67</b> – SC distributions normalized by max.....	61
<b>Figure 68</b> – SC distributions normalized by max.....	62



**7. List of Tables**

**Table 1** – overview of all the lipoprotein classes [21].....5



## References

- [1] Sun, Y., Zhou, Y., Rehman, M., Wang, Y-F., and Guo, S., Protein Corona of Nanoparticles: Isolation and Analysis, 2024, *Chem. Bio Eng.*, 1(9):757-772, [<https://doi.org/10.1021/cbe.4c00105>]
- [2] Strambeanu, N., Demetrovici, L., Dragos, D., Lungu, M., Nanoparticles: Definition, Classification and General Physical Properties, 2015, *Springer Cham.*, [DOI: [10.1007/978-3-319-11728-7\\_1](https://doi.org/10.1007/978-3-319-11728-7_1)]
- [3] Ohkawa, R., et al., Cholesterol transport between red blood cells and lipoproteins contributes to cholesterol metabolism in blood, 2020, *Journal of Lipid Research*, 61(12):1577 – 1588, [DOI: [10.1194/jlr.RA120000635](https://doi.org/10.1194/jlr.RA120000635)]
- [4] HDL (Good), LDL ([26]) Cholesterol and Triglycerides, American Heart Association, <https://www.heart.org/en/health-topics/cholesterol/hdl-good-ldl-bad-cholesterol-and-triglycerides>
- [5] Fangyuan G., Shuai L., Lianyi W., Mengqi W., Fang W., Yujia W., Yunlong J., Yinzhou D., Qingliang Y., Xiaoyan Y., Gensheng Y., Protein corona, influence on drug delivery system and its improvement strategy: A review, 2024, *International Journal of Biological Macromolecules*, [DOI: [10.1016/j.ijbiomac.2023.128513](https://doi.org/10.1016/j.ijbiomac.2023.128513)]
- [6] Pareek, V., Bhargava, A., Bhanot, V., Gupta, R., Jain, N., Panwar, J., Formation and Characterization of Protein Corona Around Nanoparticles: A Review, 2018, *J Nanosci Nanotechnol.*, 18(10):6653-6670, [DOI: [10.1166/jnm.2018.15766](https://doi.org/10.1166/jnm.2018.15766)]
- [7] García-Álvarez, R., Vallet-Regí, M., Hard and Soft Protein Corona of Nanomaterials: Analysis and Relevance, 2021, *Nanomaterials*, 11(4):888, [DOI: [10.3390/nano11040888](https://doi.org/10.3390/nano11040888)]
- [8] Zheng, J.J., Agus, J.K., Hong, B.V., et al., Isolation of HDL by sequential flotation ultracentrifugation followed by size exclusion chromatography reveals size-based enrichment of HDL-associated proteins, 2021, *Sci. Rep.*, 11, 16086, [<https://doi.org/10.1038/s41598-021-95451-3>]
- [9] Wazir, M., Olanrewaju, O.A., Yahya, M., Kumari, J., Kumar, N., Singh, J., Abbas Al-Itbi, A.Y., Kumari, K., Ahmed, A., Islam, T., Varrassi, G., Khatri, M., Kumar, S., Wazir, H., Raza, S.S., Lipid Disorders and Cardiovascular Risk: A Comprehensive Analysis of Current Perspectives, 2023, *Cureus*, 15(12):e51395, [DOI: [10.7759/cureus.51395](https://doi.org/10.7759/cureus.51395)]
- [10] Mourdikoudis, S., Pallares, M.R., Thanh, N.T.K., Characterization techniques for nanoparticles: comparison and complementarity upon studying nanoparticle properties, 2018, *Nanoscale*, 10(27):12871-12934, [<https://doi.org/10.1039/c8nr02278j>].

- [11] Ralston, G., Introduction to Analytical Ultracentrifugation
- [12] Cedervall, T., Lynch, I., Lindman, S., Berggård, T., Thulin, E., Nilsson, H., Dawson, K.A., & Linse, S., Understanding the nanoparticle–protein corona using methods to quantify exchange rates and affinities of proteins for nanoparticles, 2007, *Proc. Natl. Acad. Sci. U.S.A.*, 104(7):2050-2055, [<https://doi.org/10.1073/pnas.0608582104>]
- [13] Böhmert, L., et al. Isolation methods for particle protein corona complexes from protein-rich matrices, 2020, *Nanoscale Advances*, [<https://doi.org/10.1039/C9NA00537D>]
- [14] Walkey, C., Understanding and Controlling the Interaction of Nanomaterials with Proteins in a Physiological Environment, 2011, *Chemical Society Reviews*, 41(7):2780-99, [DOI: [10.1039/c1cs15233e](https://doi.org/10.1039/c1cs15233e)]
- [15] Hirsh, S.L., McKenzie, D.R., Nosworthy, N.J., Denman, J.A., Sezerman, O.U., Bilek, M.M.M., The Vroman effect: Competitive protein exchange with dynamic multilayer protein aggregates, 2013, *Colloids and Surfaces B: Biointerfaces*, 395-404, [<https://doi.org/10.1016/j.colsurfb.2012.10.039>]
- [16] Yanni, Y., Yaning, L., Wei, D., Dynamic process, mechanisms, influencing factors and study methods of protein corona formation, 2022, *International Journal of Biological Macromolecules*, 205: 731-739, [<https://doi.org/10.1016/j.ijbiomac.2022.03.105>]
- [17] Atkins, P.; de Paula, J.; Keeler, Atkins' Physical Chemistry, 2022, *J. Physical-Chemistry*, [<https://global.oup.com/ukhe/product/atkins-physical-chemistry-9780198847816?cc=gb&lang=en&>]
- [18] Gunawan, C., Lim, May., Marquis, C.P., Amal, R., Nanoparticle–protein corona complexes govern the biological fates and functions of nanoparticles, 2014, *J. Mater. Chem. B*, 2, 2060-2083, [<https://doi.org/10.1039/C3TB21526A>]
- [19] Moyano, D.F., Ray, M., Rotello, V.M., Nanoparticle–protein interactions: Water is the key, 2014, *MRS Bulletin*, 39(12):1069-1073, [<https://doi.org/10.1557/mrs.2014.255>]
- [20] Treuel, L., Nienhaus, G.U., Toward a molecular understanding of nanoparticle-protein interactions, 2012, *Biophysical reviews*, 4(2):137–147, [DOI: [10.1007/s12551-012-0072-0](https://doi.org/10.1007/s12551-012-0072-0)]
- [21] Feingold, K.R., Anawalt, B., Blackman, M.R., et al., Introduction to Lipids and Lipoproteins, 2000, *PubMed*, [<https://www.ncbi.nlm.nih.gov/books/NBK305896/>]
- [22] Feingold, K.R., Grunflod, C., Lipids: a key player in the battle between the host and microorganisms, [DOI: [10.1194](https://doi.org/10.1194)]
- [23] Lipoproteins, Cleveland Clinic, <https://my.clevelandclinic.org/health/articles/23229-lipoprotein>
- [24] Smith, L.C., Pownall, H.J., Gotto, A.M. Jr., The plasma lipoproteins: structure and metabolism, 1978, *Annu. Rev. Biochem.*, 47:751-757, [DOI:

[10.1146/annurev.bi.47.070178.003535](https://doi.org/10.1146/annurev.bi.47.070178.003535)]

- [25] Berneis, K.K., Krauss, R.M., Metabolic origins and clinical significance of LDL heterogeneity, 2002, *J. Lipid Res.*, 43(9):1363-1379, [DOI: [10.1194/jlr.r200004-jlr200](https://doi.org/10.1194/jlr.r200004-jlr200)]
- [26] Chroni, A., Leondaritis, G., Karlsson, H., Lipids and Lipoproteins in Atherosclerosis, 2012, *Journal of Lipids*, 2011(1), [<https://doi.org/10.1155/2011/160104>]
- [27] Goldstein, J.L., Brown, M.S., The LDL receptor, 2009, *Arterioscler. Thromb. Vasc. Biol.*, 2009, 29(4):431-438, [DOI: [10.1161/ATVBAHA.108.179564](https://doi.org/10.1161/ATVBAHA.108.179564)]
- [28] Dong, J., Guo, H., Yang, R., Li, H., Wang, S., Zhang, J., Chen, W., Serum LDL- and HDL-cholesterol determined by ultracentrifugation and HPLC, 2011, *J. Lipid Res.*, 52(2):383-388, [DOI: [10.1194/jlr.D008979](https://doi.org/10.1194/jlr.D008979)]
- [29] Viikari, J., Precipitation of Plasma Lipoproteins by PEG-6000 and Its Evaluation with Electrophoresis and Ultracentrifugation, 2009, *Scandinavian Journal of Clinical and Laboratory Investigation*, 36(3), [DOI: [10.1080/00365517609055259](https://doi.org/10.1080/00365517609055259)]
- [30] Tekie, F.S.M., Hajiramezanali, M., Geramifar, P., et al., Controlling evolution of protein corona: a prosperous approach to improve chitosan-based nanoparticle biodistribution and half-life, 2020, *Sci. Rep.*, 10, 9664, [DOI: [10.1038/s41598-020-66572-y](https://doi.org/10.1038/s41598-020-66572-y)]
- [31] Walker, H.K., Hall, W.D., Hurst, J.W., Clinical Methods: The History, Physical, and Laboratory Examinations, 1990, *Butterworths*, [<http://www.ncbi.nlm.nih.gov/books/NBK201/>]
- [32] Mariño, K., Saldova, R., Adamczyk, B., Rudd, P.M., Changes in Serum N-Glycosylation Profiles: Functional Significance and Potential for Diagnostics, 2011, *The Royal Society of Chemistry*, 3:57-93, [DOI: [10.1039/9781849732765-00057](https://doi.org/10.1039/9781849732765-00057)]
- [33] Hankins, J., The role of albumin in fluid and electrolyte balance, 2006, *Journal of infusion nursing : the official publication of the Infusion Nurses Society*, 29(5): 260 – 265, [<https://doi.org/10.1097/00129804-200609000-00004>]
- [34] Regeniter, A., Siede, W.H., Peaks and tails: Evaluation of irregularities in capillary serum protein electrophoresis, 2018, *Clinical biochemistry*, 51:48–55, [<https://doi.org/10.1016/j.clinbiochem.2017.09.017>]
- [35] Gonzalez-Quintela, A., Alende, R., Gude, F., Campos, J., Rey, J., Meijide, L.M., Fernandez-Merino, C., Vidal, C., Serum levels of immunoglobulins (IgG, IgA, IgM) in a general adult population and their relationship with alcohol consumption, smoking and common metabolic abnormalities, 2008, *Clin Exp Immunol.*, 151(1):42-50, [DOI: [10.1111/j.1365-2249.2007.03545.x](https://doi.org/10.1111/j.1365-2249.2007.03545.x)]
- [36] Kubota, T., Niwa, R., Satoh, M., Akinaga, S., Shitara, K., & Hanai, N., Engineered therapeutic antibodies with improved effector functions, 2009, *Cancer*

*science*, 100(9):1566–1572, [<https://doi.org/10.1111/j.1349-7006.2009.01222.x>]

- [37] Nguyen, V.H., Lee, B.J., Protein corona: a new approach for nanomedicine design, 2017, *Int J Nanomedicine*, 12:3137-3151, [<https://doi.org/10.2147/IJN.S129300>]
- [38] Klein, A., Human total serum N-glycome, 2008, *Advances in clinical chemistry*, 46:51–85, [<https://pubmed.ncbi.nlm.nih.gov/19004187/>] Norde, W., Anusiem, A. C.I., Adsorption, desorption and re-adsorption of proteins on solid surfaces, 1992, *Colloids and Surfaces*, 66(1):73-80, [[https://doi.org/10.1016/0166-6622\(92\)80122-1](https://doi.org/10.1016/0166-6622(92)80122-1)]
- [39] Planken, K.L., & Cölfen, H., Analytical ultracentrifugation of colloids, 2010, *Nanoscale*, 2, 1849–1869, [<https://doi.org/10.1039/C0NR00215A>]
- [40] Bekdemir, A., Stellacci, F., A centrifugation-based physicochemical characterization method for the interaction between proteins and nanoparticles, 2016, *Nat. Commun.*, 7, 13121, [doi: [10.1038/ncomms13121](https://doi.org/10.1038/ncomms13121)]
- [41] Schuck, P., Sedimentation Analysis of Noninteracting and Self-Associating Solutes Using Numerical Solutions to the Lamm Equation, 1998, *Biophys. J.*, 75, 1503-1512, [doi: [10.1016/S0006-3495\(98\)74069-X](https://doi.org/10.1016/S0006-3495(98)74069-X)]
- [42] Brown, P.H., Shuck, P., Macromolecular size-and-shape distributions by sedimentation velocity analytical ultracentrifugation, 2006, *Biophys. J.*, 90, 4651-4661, [doi: [10.1529/biophysj.106.081372](https://doi.org/10.1529/biophysj.106.081372)]
- [43] Seneshaw, M., Mirshahi, F., Min, H.K., Asgharpour, A., Mirshahi, S., Daita, K., Boyett, S., Santhekadur, P.K., Fuchs, M., Sanyal, A.J., Fast and Simplified Method for High Through-put Isolation of miRNA from Highly Purified High Density Lipoprotein, 2016, *J. Vis. Exp.*, (113):54257, [doi: [10.3791/54257](https://doi.org/10.3791/54257)]
- [44] Redgrave, T.G., Roberts, D.C.K, West, C.E., Separation of plasma lipoproteins by density-gradient ultracentrifugation, 1975, *Analytical Biochemistry*, 65, 42-49, [[https://doi.org/10.1016/0003-2697\(75\)90488-1](https://doi.org/10.1016/0003-2697(75)90488-1)]
- [45] Sharma, K., Fast Protein Liquid Chromatography: Features, Principle, Applications, 2024, <https://scienceinfo.com/fast-protein-liquid-chromatography-features-principle-applications/>
- [46] Superdex 200 Increase small-scale SEC columns, Cytiva Life Sciences, [https://www.cytivalifesciences.com/en/us/shop/chromatography/prepacked-columns/size-exclusion/superdex-200-increase-small-scale-size-exclusion-chromatography-columns-p-06190/parts-and-accessories/28990944/accessories?srsId=AfmBOoqZrvbfLt8rN9mZhxZC001Wjrza1Ir5lVnYgA0\\_fx5eiN5ta4oQ](https://www.cytivalifesciences.com/en/us/shop/chromatography/prepacked-columns/size-exclusion/superdex-200-increase-small-scale-size-exclusion-chromatography-columns-p-06190/parts-and-accessories/28990944/accessories?srsId=AfmBOoqZrvbfLt8rN9mZhxZC001Wjrza1Ir5lVnYgA0_fx5eiN5ta4oQ)
- [47] The principle and method of polyacrylamide gel electrophoresis (SDS-PAGE), MBL Life Science, <https://ruo.mbl.co.jp/bio/e/support/method/sds-page.html>
- [48] Protein Electrophoresis and SDS-PAGE, Khan Academy,

<https://www.khanacademy.org/test-prep/mcat/biomolecules/x04f6bc56:protein-analysis-techniques/a/protein-electrophoresis-and-sds-page>

- [49] The principle of Dynamic Light Scattering, Anton Paar, <https://wiki.anton-paar.com/en/the-principles-of-dynamic-light-scattering/>
- [50] Stetefeld, J., McKenna, S.A., Patel, T.R., Dynamic light scattering: a practical guide and applications in biomedical sciences, 2016, *Biophys Rev*, 8(4):409-427, [doi: [10.1007/s12551-016-0218-6](https://doi.org/10.1007/s12551-016-0218-6)]
- [51] Babick, F., Chapter 3.2.1 - Dynamic light scattering (DLS), 2020, *Micro and Nano Technologies*, 137-172, [<https://doi.org/10.1016/B978-0-12-814182-3.00010-9>]
- [52] Transmission Electron Microscopy, NanoScience Instruments, <https://www.nanoscience.com/techniques/transmission-electron-microscopy/>
- [53] MyScope Microscopy Training, Microscopy Australia, <https://myscope.training/>
- [54] Balbo, A., Brown, P.H., Braswell, E.H., Shuck, P., Measuring protein-protein interactions by equilibrium sedimentation, 2007, *Curr. Protoc. Immunol.*, 18, [doi: [10.1002/0471142735.im1808s79](https://doi.org/10.1002/0471142735.im1808s79)]
- [55] Rivas, G., Stafford, W., Minton A.P., Characterization of Heterologous Protein-Protein Interactions Using Analytical Ultracentrifugation, 1999, *Methods*, 19, 194-212, [doi: [10.1006/meth.1999.0851](https://doi.org/10.1006/meth.1999.0851)]
- [56] Cole, J.L., Lary, J.W., P. Moody, T., Laue, T.M., Analytical ultracentrifugation: sedimentation velocity and sedimentation equilibrium, 2008, *Methods Cell. Biol.*, 84:143-179, [doi: [10.1016/S0091-679X\(07\)84006-4](https://doi.org/10.1016/S0091-679X(07)84006-4)]
- [57] Ralston, G., Introduction to Analytical Ultracentrifugation
- [58] Schirf, V., & Planken, K.L., Analytical Ultracentrifuge User Guide Volume 1: Hardware, 2008
- [59] Kinoshita, M., Krul, E. S., Schonfeld, G, Modification of the core lipids of low density lipoproteins produces selective alterations in the expression of apoB-100 epitopes, 1990, *Journal of lipid research*, 31(4):701–708, [[https://doi.org/10.1016/S0022-2275\(20\)42839-1](https://doi.org/10.1016/S0022-2275(20)42839-1)]
- [60] Kumar, V., Butcher, S.J., Öörni, K., Engelhardt, P., Heikkonen, J., et al., Three-Dimensional cryoEM Reconstruction of Native LDL Particles to 16Å Resolution at Physiological Body Temperature, 2011, *PLOS ONE*, 6(5):e18841, [<https://doi.org/10.1371/journal.pone.0018841>]
- [61] Langer, K., Balthasar, S., Vogel, V., Dinauer, N., von Briesen, H., Schubert, D, Optimization of the preparation process for human serum albumin (HSA) nanoparticles, 2003, *International journal of pharmaceutics*, 257(1-2):169–180, [[https://doi.org/10.1016/s0378-5173\(03\)00134-0](https://doi.org/10.1016/s0378-5173(03)00134-0) ]
- [62] Prin, C., Bene, M. C., Gobert, B., Montagne, P., & Faure, G. C, Isoelectric restriction

of human immunoglobulin isotypes, 1995, *Biochimica et biophysica acta*, 1243(2):287–289, [DOI: [10.1016/0304-4165\(94\)00187-3](https://doi.org/10.1016/0304-4165(94)00187-3)]

- [63] Chapman, K., Pullen, N., Coney, L., Dempster, M., Andrews, L., Bajramovic, J., Baldrick, P., Buckley, L., Jacobs, A., Hale, G., Green, C., Ragan, I., Robinson, V., Preclinical development of monoclonal antibodies: considerations for the use of non-human primates, 2009, *MAbs*, 1(5):505-16, [doi: [10.4161/mabs.1.5.9676](https://doi.org/10.4161/mabs.1.5.9676)]

## **Acknowledgements**

Desidero esprimere la mia sincera gratitudine a tutti i professori che mi hanno accompagnato lungo questo percorso. Un ringraziamento speciale al Professor Francesco Stellacci e alla Professoressa Laura Fabris, il cui supporto continuo e la loro guida sono stati fondamentali per il mio percorso accademico. La fiducia che hanno riposto in me e il loro impegno nel valorizzare il mio potenziale hanno avuto un impatto decisivo sul mio sviluppo professionale.

I would like to extend my heartfelt thanks to the entire SuNMIL team for their unwavering support throughout this journey. Each of you has played a crucial role in making this project a reality, and I am deeply grateful for your collaboration.

In particular, I would like to express my sincere appreciation to Dr. Quy Ong, whose guidance and expertise were instrumental in helping us develop and refine our project. Your thoughtful advice and insights have been invaluable to us.

A special thank you goes to Ding, whose constant support and willingness to help in times of need have made all the difference. Your encouragement and guidance have been a steady source of motivation for us all.

I would also like to thank Katya and Cécilia for being there when we needed help the most. Your support during critical moments truly made a difference, and I'm deeply grateful.

Thank you all for your hard work, dedication, and for being such a wonderful team to work with.